DOE/SF/17170--T25

DE91 009292

HIGH-TEMPERATURE ALLOYS FOR HIGH-POWER THERMIONIC SYSTEMS

Final Report

Submitted to

Department of Energy

(Contract No. AC03-87SF-17170)

Prepared by

Kwang S. Shin

Dean L. Jacobson

Lester D'cruz

Anhua Luo

Bor-Ling Chen

Dept. of Chemical, Bio and Materials Engineering
Arizona State University
Tempe, AZ 85287

August 1990

DISCLAIMER

SUMMARY

The development of tungsten-base alloys with expected high-temperature strength emphasizes the importance of processing innovations in the area of materials fabrication. These alloys are best produced by the sintering of powders. However the density attainable in the final compact by the conventional sintering route is inadequate for high-temperature strength. Eutectic activated sintering is a process aided by alloying addition that combines the features of liquid phase sintering and solid state activated sintering. Near theoretical densities are attainable by this method of sintering. The sintering experiments were performed at 1492 K and 1703 K, respectively, on pure tungsten and W-Ir-HfC alloys. These experiments consisted of sintering the sample in a thermionic bombardment furnace for short durations of 1-2 hours. The effects of sintering temperature, total sintering duration and alloying additives (Ir-Hf) on the volume shrinkage have been studied. It has been found that higher sintering temperatures result in higher densifications for both the pure W compacts as well as the W-Ir-Hf compacts. And for both sintering temperatures the initial densification rates for the alloyed compacts are lower than those observed in the pure W compacts. This may well be due to the occurrence of chemical reactions which preceed neck growth. Besides, the alloy compact sintered at 1492 K attains a larger level of densification than the pure compact sintered at the same temperature. However the opposite occurs in the compact sintered at 1703 K, the higher temperature of sintering.

The tensile properties of pure W, W-Re, W-ThO_2, W-Ir, W-Re, W-Re-ThO_2, and W-Re-HfC alloys at room temperature and high temperatures (1600 K~3000 K) in a vacuum better than 10^{-7} torr are discussed in chapter 2. The solution softening appears to be a very effective way to improve the low-temperature fabricability of tungsten. The ductility of either arc-melted tungsten or powder metallurgy tungsten increases remarkably with the addition of iridium and rhenium at room temperature. And the minimum hardness and yield strength are observed at 3.6%Re or 0.45%Ir. When testing temperature increases, the yield strengths, ultimate tensile strengths, and work-hardening rates of tungsten-base alloys monotonically decrease. But the strength properties of high-Re alloys are more sensitive to the change of temperature than those of low-Re alloys, and the addition of the second-phase particles will also increase the temperature sensitivity of tungsten. At the same time, the materials having higher temperature sensitivity show a greater strain-rate sensitivity. The solid-solution strengthening of Re in tungsten is effective up to about 2000 K, and W-Re alloys show a significantly greater ductility than pure tungsten at high temperatures. Particle strengthening is effective in tungsten above 2200 K. HfC particle shows a stronger effect in strengthening tungsten than ThO_2 particle at ultra-high temperatures. To our present knowledge, W-Re-HfC system appears to be the strongest metallic material at temperatures above 2000 K. Because of their relatively strong grain boundary cohesion, arc-melted tungsten-base alloys generally show a tendency of fracturing transgranular at temperature above 1600 K. Whereas transgranular fracture is the dominant high temperature fracture mode of arc-melted alloys.

A high-temperature high-vacuum creep testing machine has been built up for the present project. The step-load creep tests were conducted on W-4Re-0.26HfC and W-3.6Re-1ThO_2 alloys at temperatures ranging from 1955 to 2500 K and at stresses from 10 to 70 MPa in a vacuum of 8 x 10^{-7} torr. The results of creep behavior of these two particle-strengthened materials are discussed in Chapter 3. The stress exponent of the steady-state creep is 5.2 for W-4Re-0.26HfC alloy, and is 4.6 for W-3.6Re-1ThO_2. Both materials are not sensitive to the test temperature from 1955 to 2500 K. At temperatures from 1955 to 2190 K, the activation energy for creep deformation is about 105.5 Kcal/mol for W-4Re-0.26HfC. However, the activation energy for creep increased to 161.9 Kcal/mol at temperatures from 2300 to 2500 K. The creep deformation mechanism for W-4Re-0.26HfC appears most likely to be diffusion controlled dislocation climb over the HfC

particles at temperatures from 1955 to 2190 K, while lattice self-diffusion is the rate-controlling creep mechanism at temperatures above 2300 K. The activation energy for creep deformation of W-3.6Re-1ThO_2 is about 105.8 Kcal/mol. at temperatures from 2040 to 2200 K, and is about 152.8 Kcal/mol. at temperatures from 2300 to 2500 K. The rate-controlling deformation mechanism of W-3.6Re-1ThO_2 at temperatures between 2040 and 2200 K is most likely to be diffusion controlled dislocation climb. While at temperatures above 2300 K the rate-controlling deformation mechanism seems to be lattice self-diffusion, as in the case of W-4Re-0.26HfC. Failure mode of these two alloys was intergranular fracture. The intergranular fracture of W-4Re-0.26HfC was caused by wedge-shaped and irregular-shaped cracks, while the intergranular fracture of W-3.6Re-1ThO_2 was caused by r-type cracks. Both HfC and ThO_2 particles are very effective in strengthening W-Re alloys. Both W-4Re-0.26HfC and W-3.6Re-1ThO_2 are more creep resistant than pure tungsten, W-5Re, and W-23.4Re-0.27Hf-C at temperatures above 0.5 T_m. However, at temperatures below 2250 K W-4Re-0.26HfC is more creep resistant than W-3.6Re-1ThO_2 due to the pinning effect of HfC particles on dislocations, subgrain boundaries, and grain boundaries. While, at temperatures above 2250 K, W-3.6Re-1ThO_2 has higher creep strength than W-4Re-0.26HfC due to the rapid coarsening of HfC particles.

TABLE OF CONTENTS

CHAPTER 1 - PROCESSING OF TUNGSTEN ALLOYS

1.1 INTRODUCTION

Tungsten has the highest melting temperature of all known metals with a melting point of 3683 K (3410 °C). In an effort to lower energy costs as well as to tackle problems related to containment, high temperature contamination and ease of fabrication it has become necessary to evolve innovative avenues for the fabrication of Tungsten and its alloys at temperatures much lower than their melting points. Powder processing and sintering, which forms the basis of this study is one such avenue.

Packed metallic powders will bond together when heated to temperatures in excess of half the melting point of the metal. This phenomenon is called sintering. A common characteristic of all forms of sintering is a reduction in particle surface area along with simultaneous strengthening in the packed material. This occurs due to the formation of interparticle bonds brought about by atomic motion at the temperature of sintering. Besides interparticle bonding, significant changes have been observed in pore structure and compact properties like strength, ductility, conductivity and magnetic permeability.

Considerable enhancement in the rate of interparticle bonding can be brought about by, (a) application of external pressure (b) creation of a liquid phase around particles (c) increased atomic motion (diffusion) caused by specific additive elements. The sintering that results due to one or more of these mechanisms is usually referred to as enhanced or activated sintering. Our present investigation concentrates on the effect of Ir and Hf on the sintering characteristics of pure W. With the addition of Ir alone we expect to study sintering which would occur predominantly by the mechanism described in (c) above. The mechanism outlined in (b) however will be studied by small additions (< 2 wt.%) of a blend prepared by grinding a mixture of Hf and Ir powders corresponding to the eutectic composition of Hf-(17at.%) Ir. The eutectic temperature corresponding to this phase is 1703 K (1430 C).

Appendix 1 covers some of the basic theoretical aspects related to this work while Appendix 2 reviews the experimental information on processing of tungsten that exists at present. The experimental set up utilized in this work has been described in section 1.2 and the experimental results obtained thus far are included in section 1.3. Initial attempts to utilize an existing multiple diffusion model to study sintering in our system has been presented in section 1.4 along with relevent discussions.

1.2 EXPERIMENTAL SET-UP

1.2.1 POWDER PROCESSING STEPS

1.2.1.1 Weighing

Cent-o-gram four beam balance (Ohaus model 311) is used for most of the powder weighing needs. This balance has a capacity of 311 grams with a sensitivity of 0.01 g. The sample preparation procedure requires the weighing of powders of 3 grams weight for disc samples and upto 10 grams for cylindrical samples which falls well within the capability of this instrument. Weighing of Ir and Hf involves amounts of the order of 0.1 gram which is also possible with reasonable accuracy using this instrument.

1.2.1.2 Grinding

The grinding step is required for the cominuition and blending of Ir and Hf powders. The factory available sizes are much too large to be used directly furthermore an intimate mixture of these two powders is necessary for the eutectic activated sintering study. Owing to the small amounts of powder involved in each batch, a Diamonite mortar and pestle is used. This particular product is made from pure processed aluminum oxide and has a specific gravity of 3.6 with a hardness of about 9 on the Mhos scale.

1.2.1.3 Mixing

The powder mixing device consists of a simple rotating drum drive by a HP motor with a constant speed of rpm. The powders are loaded into a glass vial which is then fastened at a 20 degree incline within the drum as shown schematically in figure 1.2.1 .

1.2.2 COMPACTION OF BLENDED POWDERS

1.2.2.1 Mould and Plunger

A hardened A2 tool steel mould has been fabricated for room temperature compaction of W powders. Since no lubrication is used in the compaction operation, the contact surfaces in the mould are precision ground to reduce friction. The mould assembly is shown in figure 1.2.2 .

1.2.2.2 Compression Load

The compaction load utilized for the 0.5 micron powder is 10,000 pounds which corresponds to a compaction pressure of 50 ksi in the mould. The coarser powders require higher loads but the maximum pressure will not exceed 100 ksi.

1.2.3 SINTERING OF COMPACTS

1.2.3.1 Thermionic Bombardment Vaccum Bell-Jar Furnace

Supply (Hiptronics): AC fillament heating , 10 V , 30 A

DC output (max) , 10 KV , 500 mA

Heater : tungsten fillament wire (flat spiral).

Vaccum : roughing pump and diffusion pump attains 10^{-6} torr.

The sample holder (tantalum) sits on a molybdenum stage. The power supply leads are connected to a pair of high temperature contacts which in turn hold the fillament right below the sample holder. A gap of about 2 mm is maintained between the fillament and the bottom surface of the sample holder. A thermocouple is introduced through a hole in the sample holder and touches the surface of the sample. The sample holder and stage are grounded. A schematic describing this configuration is shown in figure 1.2.3 .

1.2.3.2 Vaccum/Argon Radio-Frequency Induction Furnace

Supply (Lepel) : Rf supply 450 KHz , 45 KVA

Heater: Helical copper coil, tube O.D 1/8", I.D 1/16"A

This furnace consists of a double-wall stainless steel vaccum chamber fitted with high vaccum Rf feedthrough connected to the water cooled copper coil heater. The sample holder is concentric to the coil and sits on an Inconel stage. When used in the argon atmosphere mode the sample holder used was a graphite crucible filled with loose W powder. In the vaccum mode a tantalum sample holder, similar to that used in the thermionic bombardment furnace, is used. The vaccum system, at present, consists of a sorbtion pump for initial pump down and hi-vac Ion pump. Owing to the tendency of normal plumbing fittings to leak in vaccum, special vaccum fittings have been used on the attatchments to the copper coil heater.

1.2.3.3 Vaccum Hot Pressing Furnace

Supply : same as above

Heater : same as above

This furnace is being presently built to include the capability of studying the effect of applied stress on the sintering process and the resultant density of the compact. The furnace consists of a double-walled vaccum chamber with the Rf feedthrough fitting and thermocouple feedthrough. The sample holder in this case is a molybdenum mould and plunger assembly which rests on a stainless steel base. The load will be applied externally and transmitted through a stainless steel bar attatched to a vaccum bellow. The vaccum system once again will be a sorbtion pump and an Ion pump.

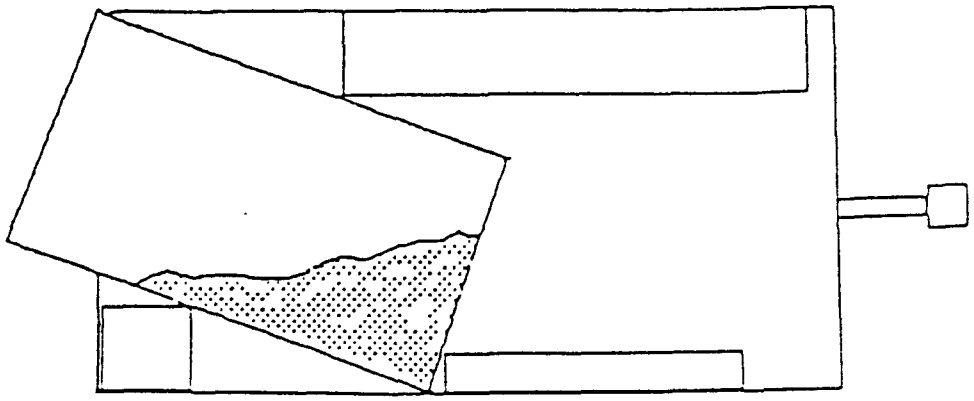

Fig. 1.2.1: Rotary Drum for Mixing of Powders

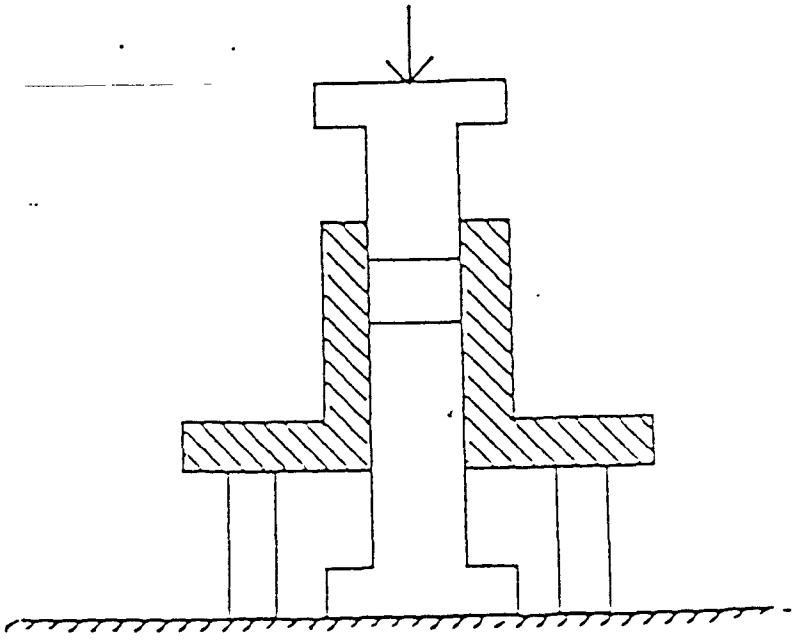

Fig. 1.2.2: Powder Compaction Mould.

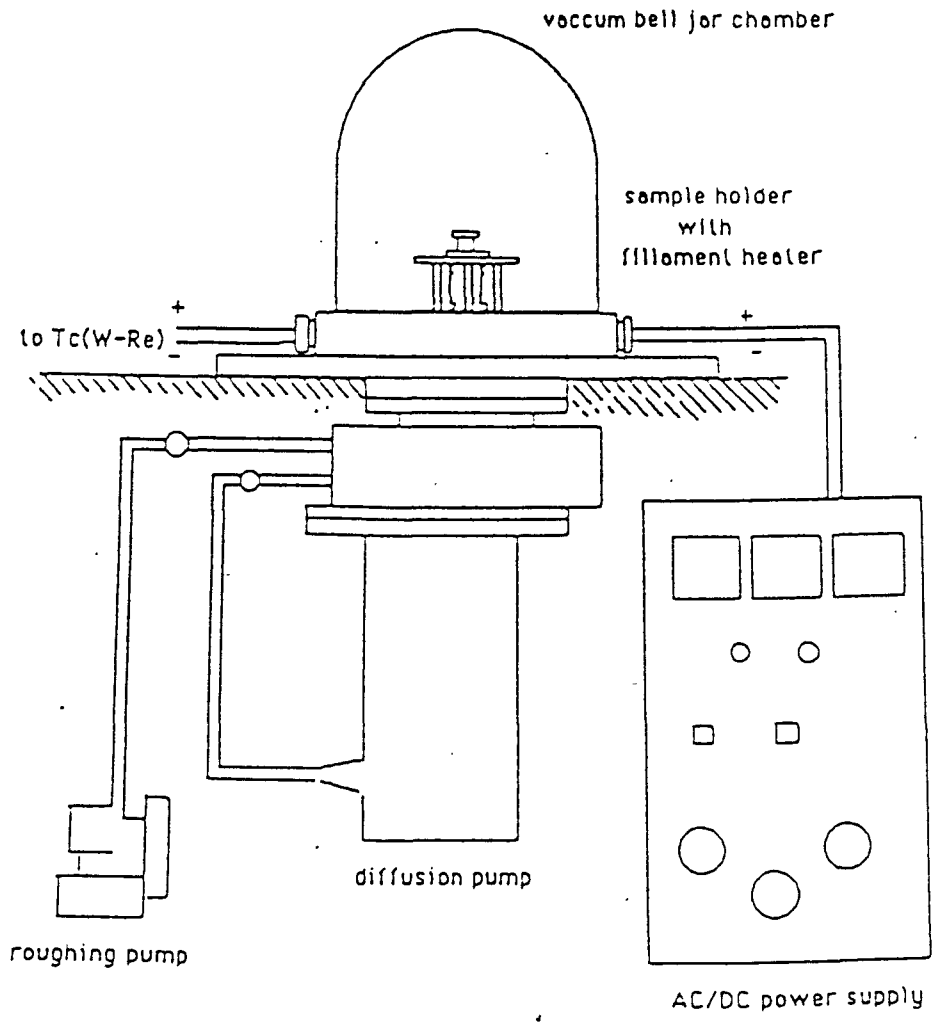

Fig. 1.2.3: Thermionic Bombardment Heating Furnace

1.3 EXPERIMENTAL RESULTS AND DISCUSSIONS

Initial sintering experiments have been performed which attempt, (a) to standardize the experimental procedure so as to generate reproducable data and (b) to perform prelimenary tests on the theoretical hypothesis regarding the role of Ir and Ir-Hf eutectics as sintering activators.

1.3.1 TEMPERATURES OF SINTERING

Initial experiments have concentrated on two temperatures of sintering namely 1492 K (0.405 Tm) and 1703 K (0.450 Tm).

1.3.2 GEOMETRY OF SAMPLES

Disc-shaped samples for these experiments were fabricated from W powder of 0.5 micron size. Powders for the alloyed samples were prepared by adding a pre-ground blend of composition Hf-(17 wt%) Ir, to pure W powder. The size of the green samples were 0.5 inches in diameter and around 0.1 inch (2.5 mm) in height.

1.3.3 SINTERING METHODOLOGY

The experiments consisted of sintering the sample in the thermionic bombardment furnace for short durations of between 1-2 hours at a stretch and extracting the sample for measurement of density. By repeating this procedure on a particular sample several times the variation of density with sintering time was obtained for times upto 10 hrs. The standard experimental procedure evolved maintained a total heat-up time of between 20 to 30 min. for these thin disc samples. The vaccum attained in the chamber was of the order of 10^{-6} Torr.

1.3.4 ISOTHERMAL SINTERING RESULTS

Figures 1.3.1 through 1.3.4 contain the data obtained from these experiments which has been presented in terms of three standard densification indicators used in sintering studies namely, volume shrinkage defined as (Vo-V}/Vo densification parameter defined in terms of the sample density as (Ds-Do}/(Dth-Do}, and dimensionless neck size (x/a) in a packed sphere particle geometry given by,

$$x/a = 0.74 - (f/3^{1/3})$$

where $f = 1 - (Ds/Dth)$

1.3.5 ANALYSIS OF EXPERIMENTAL DATA

The effects of sintering temperature, total sintering duration and alloying additives (Ir-Hf) on the volume shrinkage can be studied from figure 1.3.5. The following conclusions can be drawn from this information:

(a) As expected higher sintering temperatures result in higher densifications for both the pure W compacts as well as the W-Ir-Hf compacts.

(b) For both sintering temperatures the initial densification rates for the alloyed compacts are lower than those observed in the pure W compacts.This may well be due to the occurence of chemical reactions which preceed neck growth.

(c) The alloyed compact sintered at 1492 K attains a larger level of densification than the pure compact sintered at the same temperature. However the opposite occurs in the compact sintered at 1703 K, the higher temperature of sintering.

1.3.6 MICROSTRUCTURE OF SINTERED SAMPLES

1.3.6.1 Characteristics of Metal Powders

Tungsten powder of 99.9% purity and an average particle size of 0.5 mm was utilized for sample fabrication. The powder particles possess roughly equiaxed shapes as can be seen in Figure 1.3.6 which shows partially sintered regions in a compact sintered at 1200 C. A distribution of sizes exists in the powder which is evident in Figure 1.3.7 which shows a region of agglomerated fines in the compacted powders. Figure 1.3.8 shows the secondary electron image and the topographical back scattered electron image of a partially sintered region in a pure tungsten compact. It is clear that the particles are irregularly shaped with sharp corners and edges. Figure 1.3.9 shows the fracture surface of an alloyed tungsten compact which once again exhibits the irregular nature of the tungsten particles. These observations will be significant to exercises involving the comparison of experimental sintering data with theoretical simulations of the densification process since most theoretical treatments assume a spherical particle geometry.

1.3.6.2 Compacts with Ir and Hf Additions

Sintering experiments were performed on samples fabricated from 0.5 micron tungsten powder mixed with a ground blend of iridium and hafnium mixed in proportion to correspond to a composition of Hf-(17 at%)Ir. This is the composition of a eutectic in the Hf-Ir phase diagram which melts at 1430 C (1700 K). The compositions of the mixed powders used to fabricate the samples were W-(1 wt%)Ir-(4.5 wt%)Hf and W-(2 wt%)Ir-(8.2 wt%)Hf. An evaluation of the shrinkage characteristics of these samples sintered in vaccum showed strong indications of oxygen segregation controlled densification behavior. This is likely to result due to both liquification of tungsten oxide layers as well as the high oxygen affinity of the hafnium particles. The only expected effect of oxygen on the iridium phase is the formation of volatile oxides at around 900 C resulting a slight reduction in iridium content.

Due to different extents of shrinkage at the center and the periphery of samples heated by thermionic bombardment it was possible to compare regions of incomplete sintering with those where complete sintering has occurred. As seen in Figure 1.3.10 large pores seem to surround regions of complete sintering . In Figure 1.3.11 the distribution of interparticle porosity indicates that well packed regions sinter to a greater extent while the loosely packed regions remain partially sintered. The loosely packed regions also accomodate any localized dimensional changes associated with the progress of sintering in adjacent fully sintered regions, therefore leading to localized pore growth. This fact is probably responsible for the large pores observed surrounding fully sintered areas of the matrix. Figure 1.3.12 shows magnified secondary electron images of a large pore which clearly shows a significant amount of rounding of edges and corners on the particle surfaces leading to a more spherical shape compared to the angular shapes of the initial powders (Fig.1.3.6). The surface of particles in the pore (Fig.1.3.12 b) also shows evidence of globular debris which seems to be composed of small amounts of a solidified liquid which may have squeezed into the pore during densification.

Compositional analysis was performed on the sintered samples using electron microprobe . Hafnium x-ray scans were used to qualitatively identify the hafnium particles, which appear as a dark grey phase under secondary electron imaging conditions. The iridium-rich phase appears as a light phase and is, in fact, an intermediate ε phase with around 50 wt% W. Either an iridium scan

or a tungsten scan can be used to to identify this phase. Oxygen segregation in the sample was evaluated qualitatively by running oxygen x-ray scans on the second-phase particles as well as the matrix. Figure 1.3.13 shows an hafnium-rich particle with the superimposed hafnium x-ray scan (1.3.13 a) and an oxygen x-ray scan (1.3.13 b). Figure 1.3.14 shows the corresponding micrographs for the Ir-rich particle. Oxygen scans across pores in the microstructure indicate a higher concentration of oxygen at the surface of the pores. Figure 1.3.15 a and b show the superimposed oxygen scans across a small and large pore respectively. These observations indicate that oxygen segregates almost completely to the hafnium particles. The levels of Hf, Ir, W and O were analyzed using electron probe microanalysis on specific points in the microstructure of the sintered W-(1 wt %)Ir-(4.5 wt%)Hf compact and the following was obtained.

Hafnium-rich particles

(84.83 wt%)Hf (13.59 wt%)O +(1.5 wt%)

Note: Stoichiometry of HfO_2 gives (84.80 wt%)Hf+(15.2 wt%)O

Iridium-rich particles

(51.31 wt%)W (45.37 wt%)Ir (0.03 wt%)O +(3.29%)

Matrix

(97.81 wt%)W (0.70 wt%)Ir (0.14 wt%)O +(1.35%)

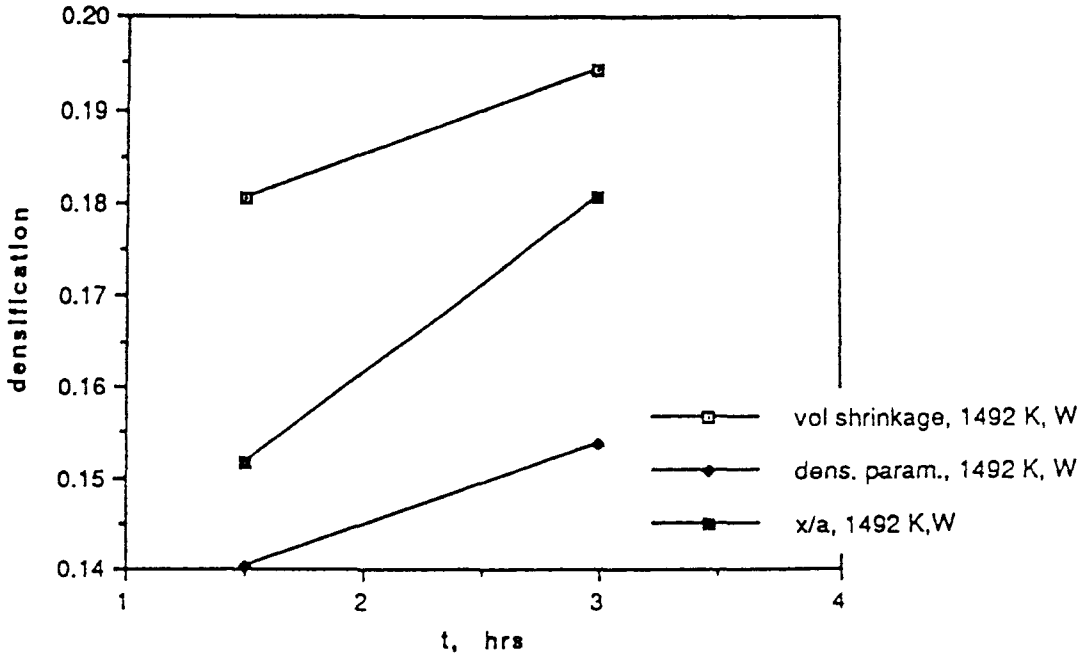

Fig. 1.3.1: Variation of densification parameters as a function of time in pure W sintered at 1492 K.

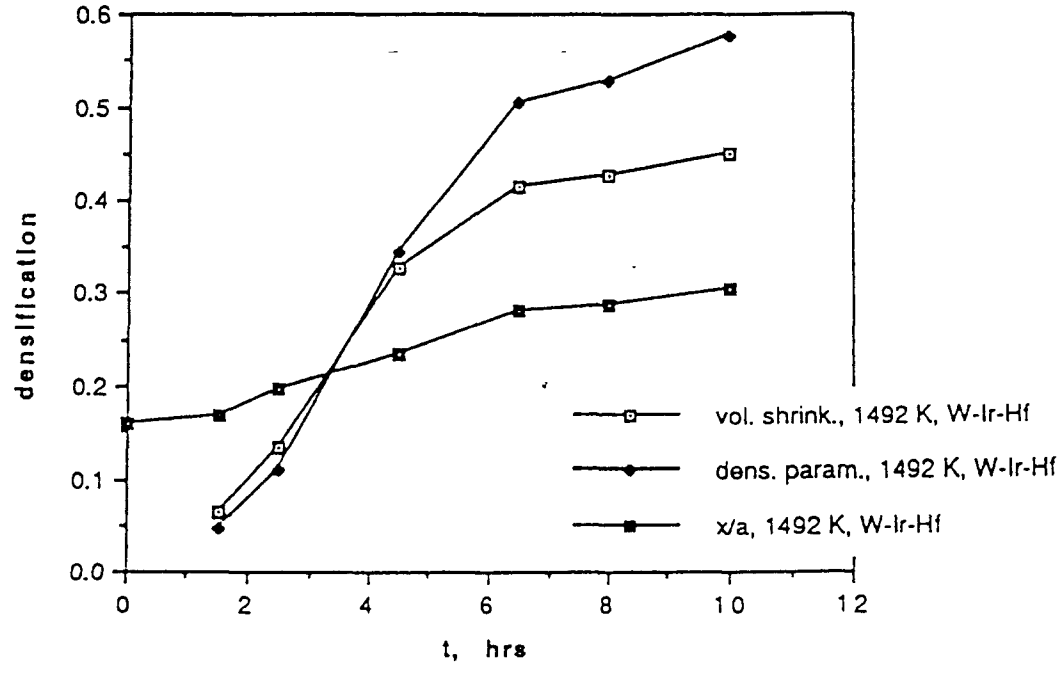

Fig. 1.3.2: Variation of densification parameters as a function of time in alloyed W sintered at 1492 K.

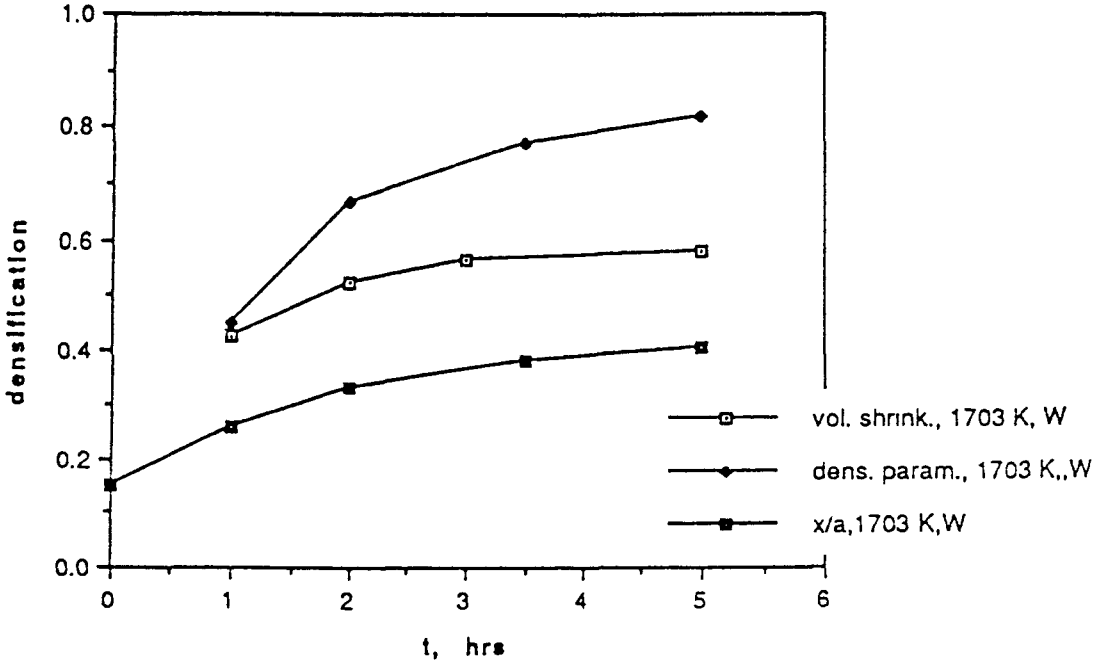

Fig. 1 3.3: Variation of densification parameters as a function of time in pure W sintered at 1703 K.

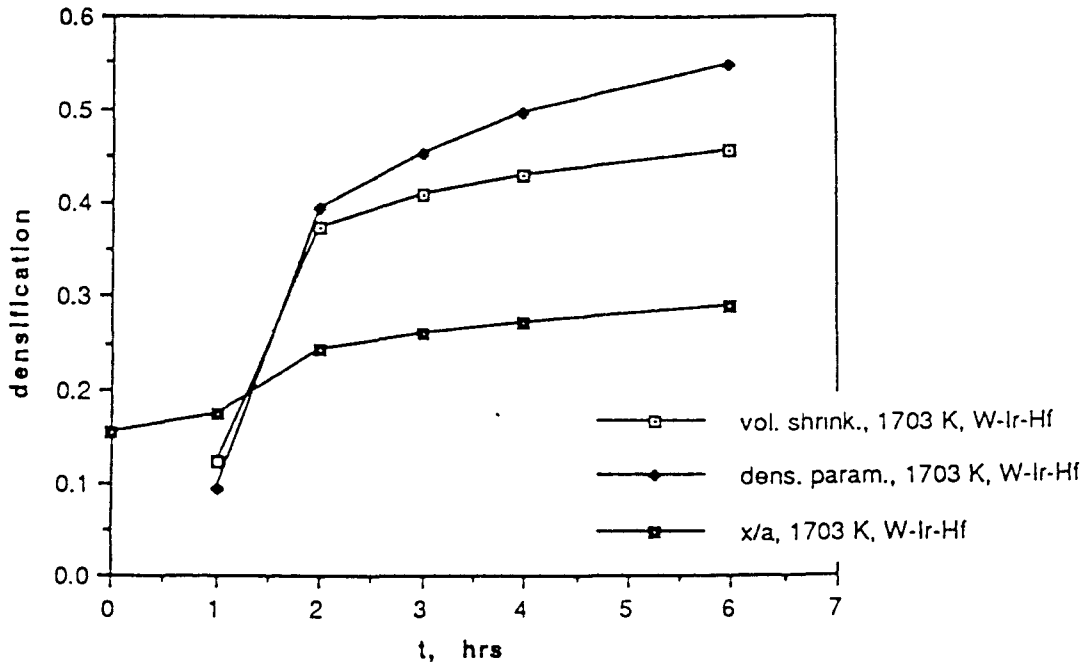

Fig. 1.3.4: Variation of densification parameters as a function of time in alloyed W sintered at 1703 K.

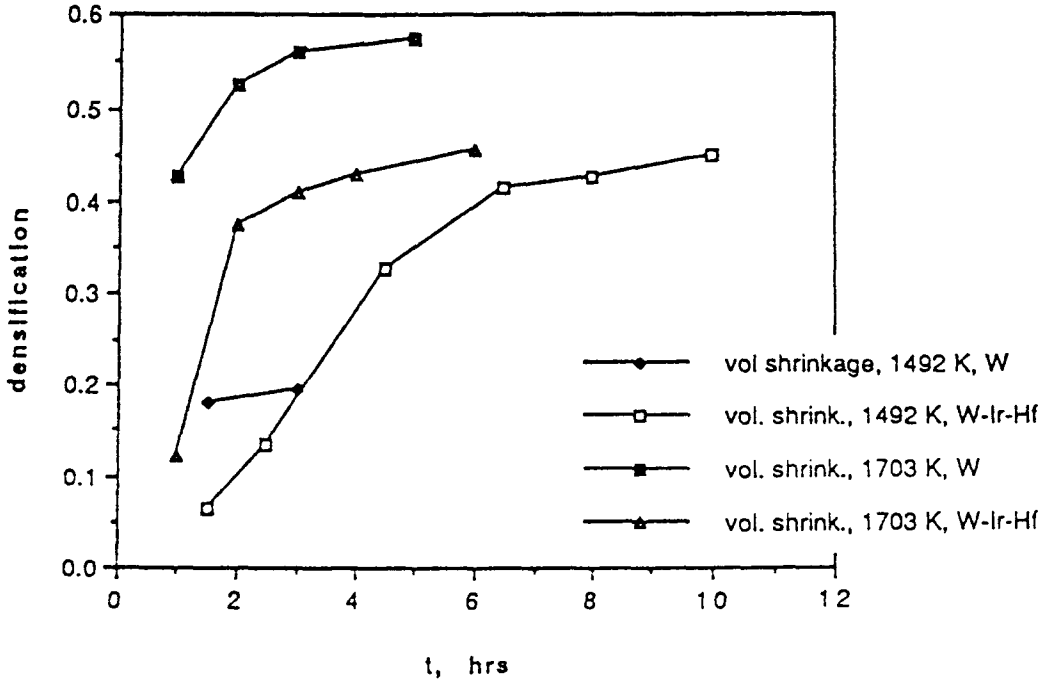

Fig. 1.3.5: Comparison between volume shrinkage values in pure W and alloyed W compacts.

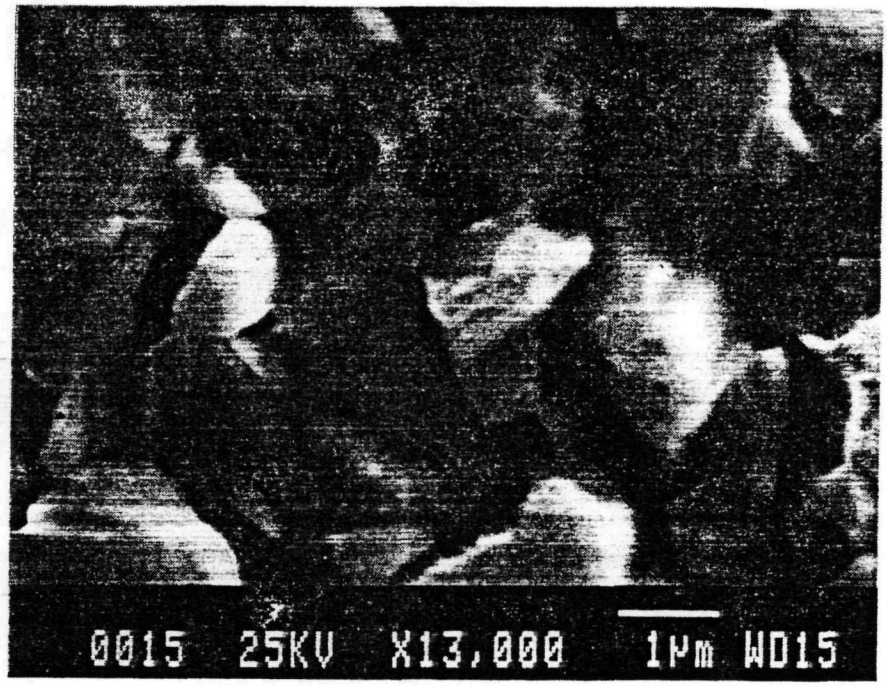

Fig. 1.3.6: Equiaxed tungsten particles in pure 0.5 μ powder

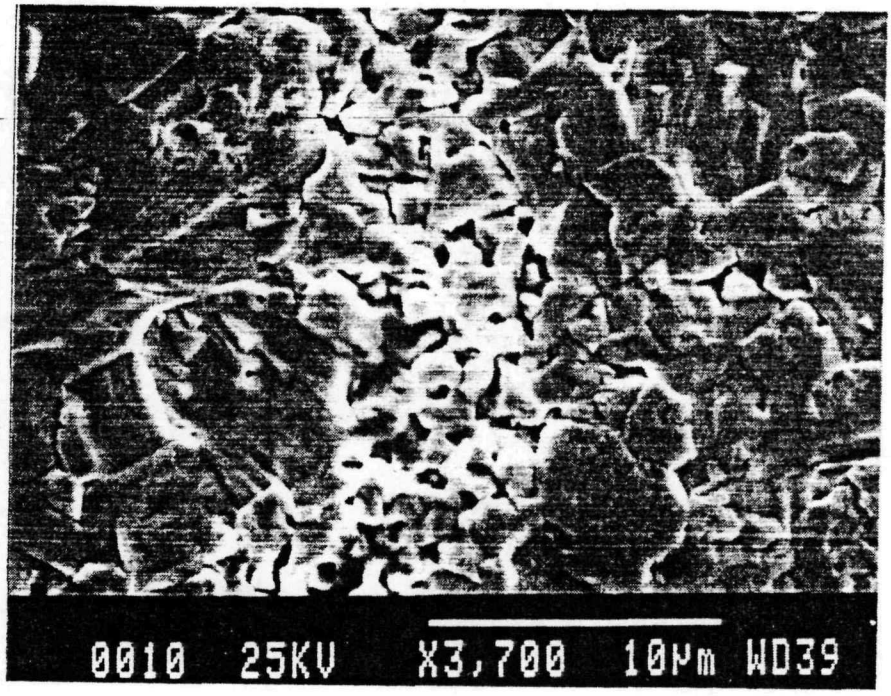

Fig. 1.3.7: Agglomeration of fines in compacted 0.5 μ powder.

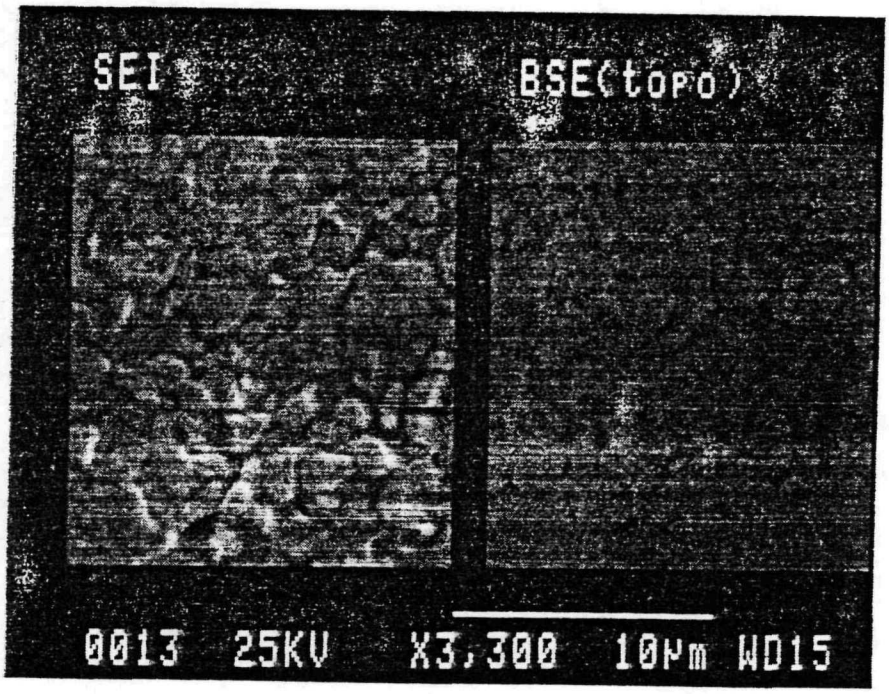

Fig. 1.3.8: Partially sintered region in pure 0.5 µ W compact.

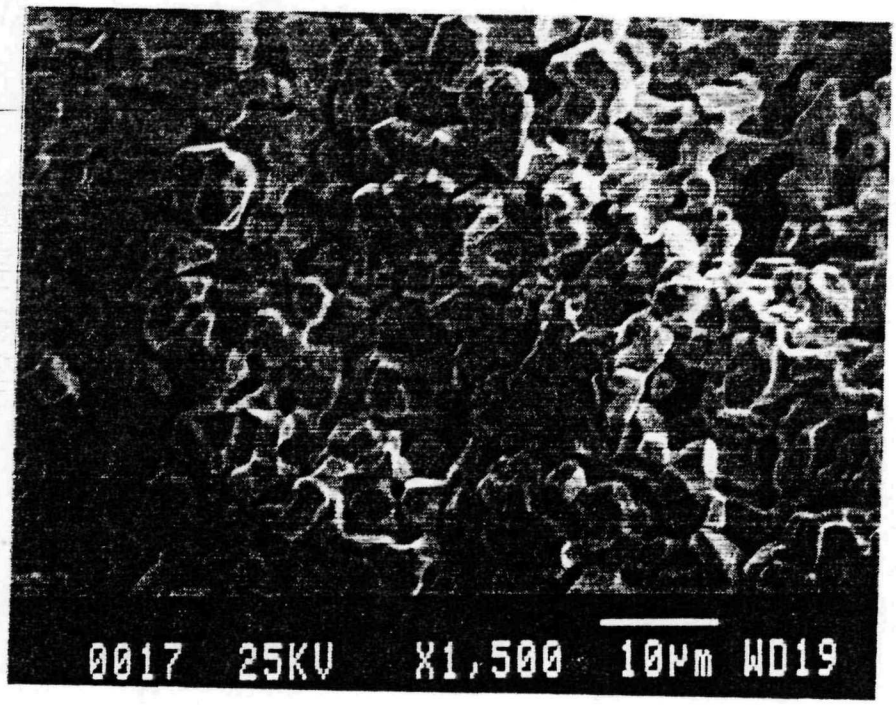

Fig. 1.3.9: Fracture surface of Ir, Hf alloyed W compact.

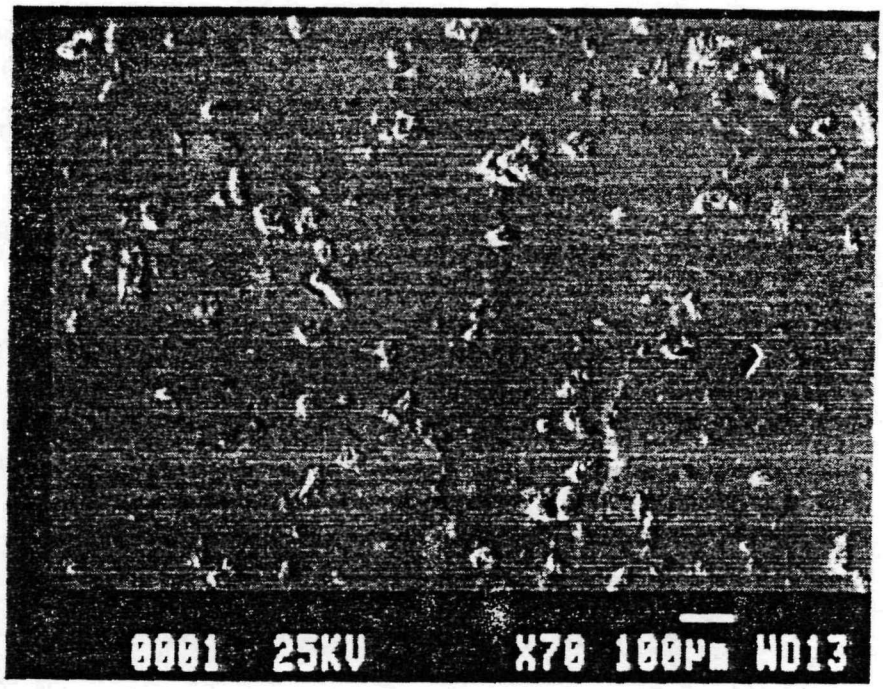

(a)

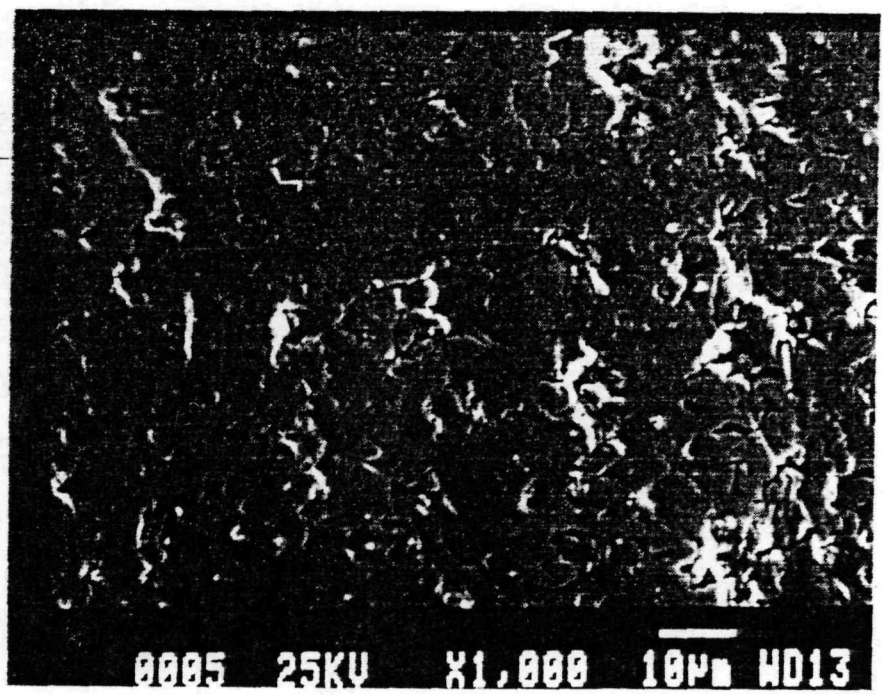

(b)

Fig. 1.3.10: Sintered regions in W-(1.0wt%)Ir-(4.5 wt%)Hf powder-mixed samples (T=1200 C, t=10 hrs).
(a) At the center of the sample (b) Near edge of the sample.

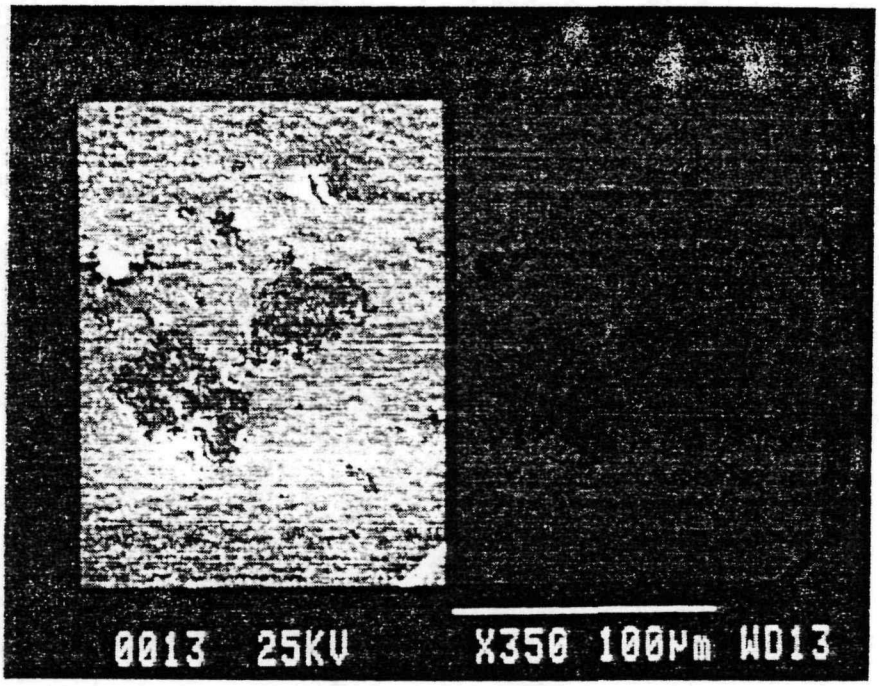

(a)

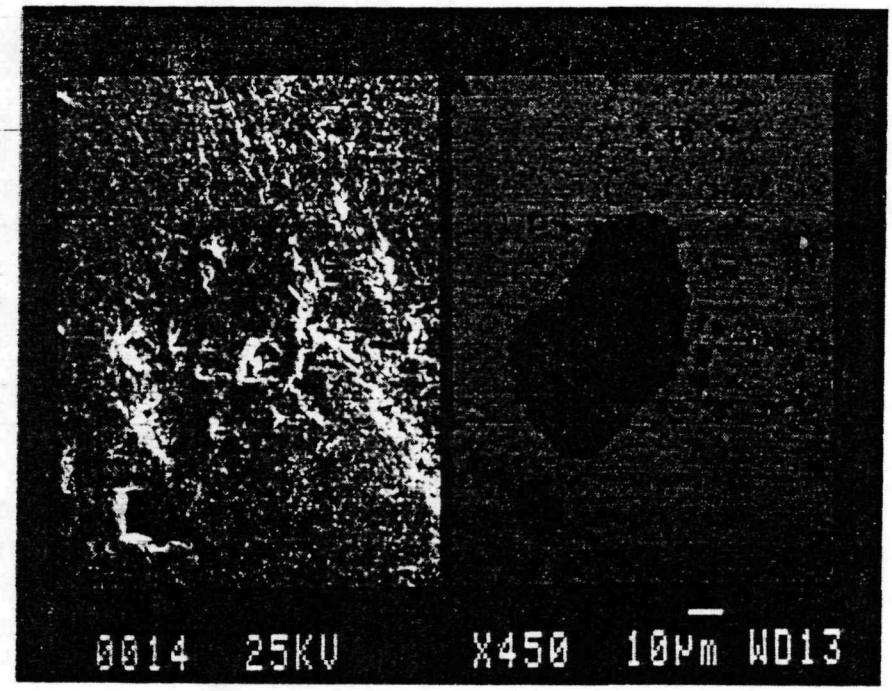

(b)

Fig. 1.3.11: Secondary Electron and Back-Scattered Electron images of hafnium particles in the tungsten matrix.
(a) At the center of the sample (b) Near edge of the sample

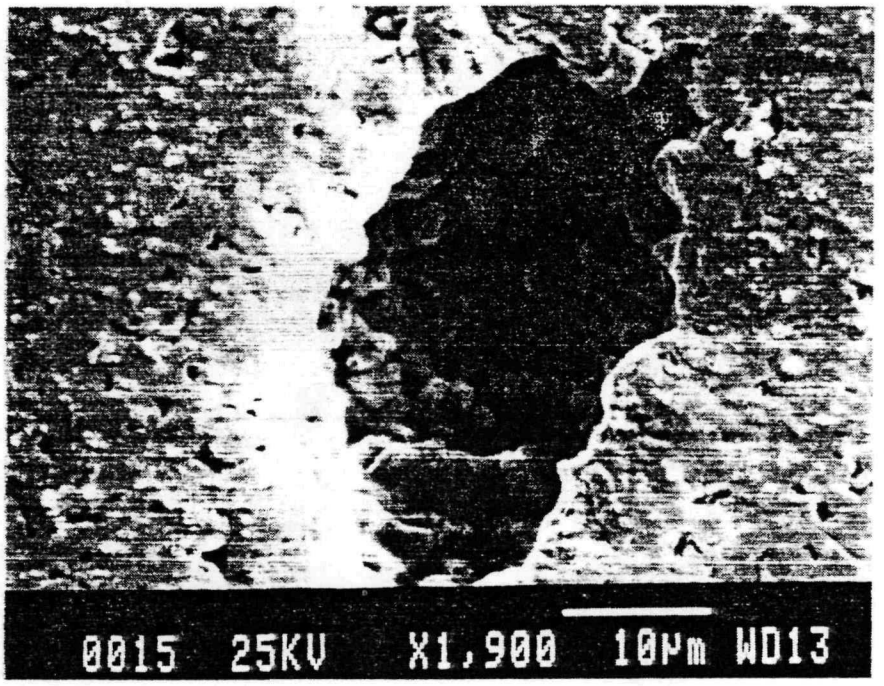

(a)

(b)

Fig. 1.3.12: Large pores in the sintered sample
(a) 1900 X (b) 4300 X

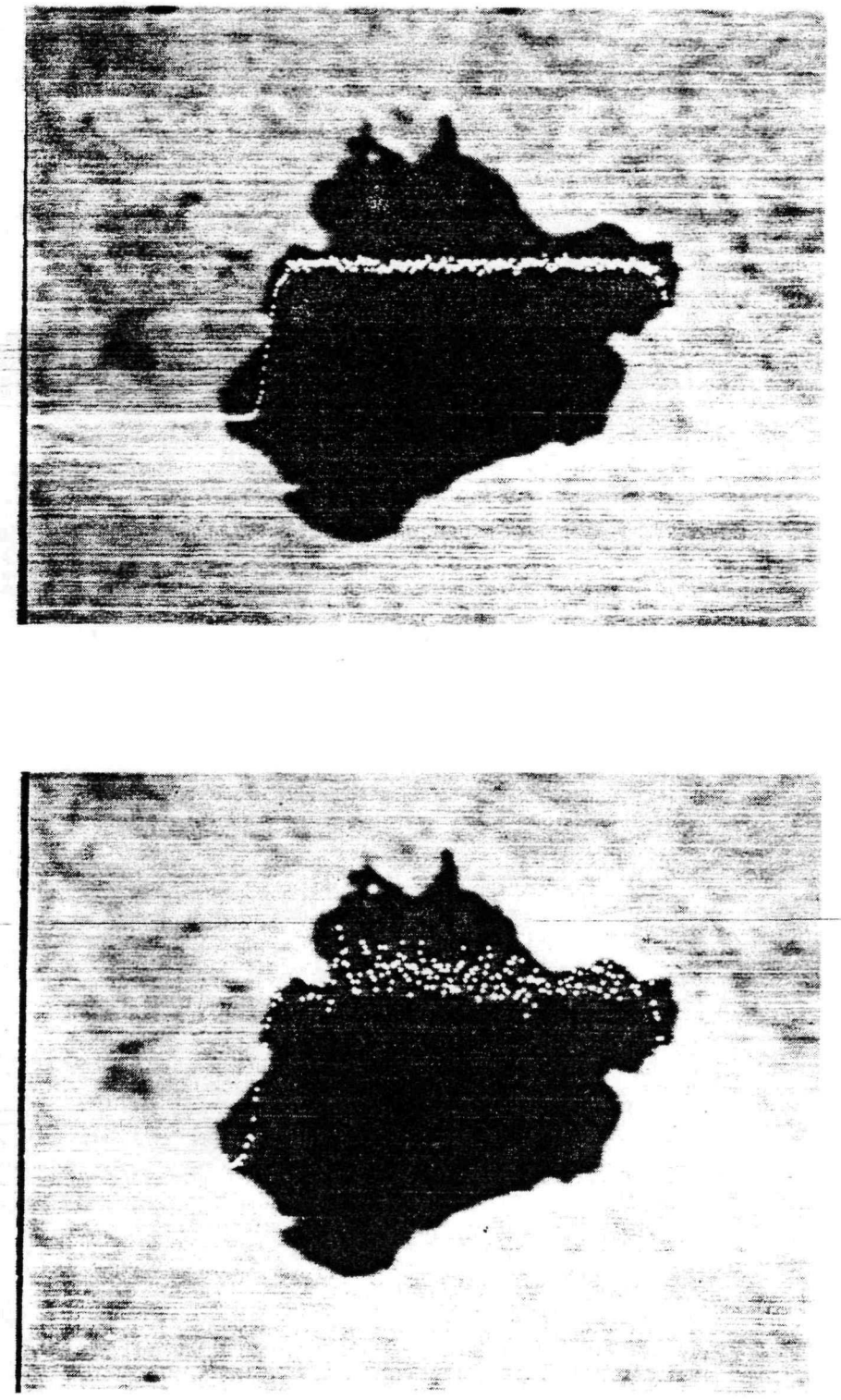

Fig. 1.3.13: Hafnium particles in W-(1.0 wt%)Ir-(4.5 wt%)Hf compact sintered at 1220 C for 10 hrs.
(a) hafnium X-ray scan (b) oxygen X-ray scan

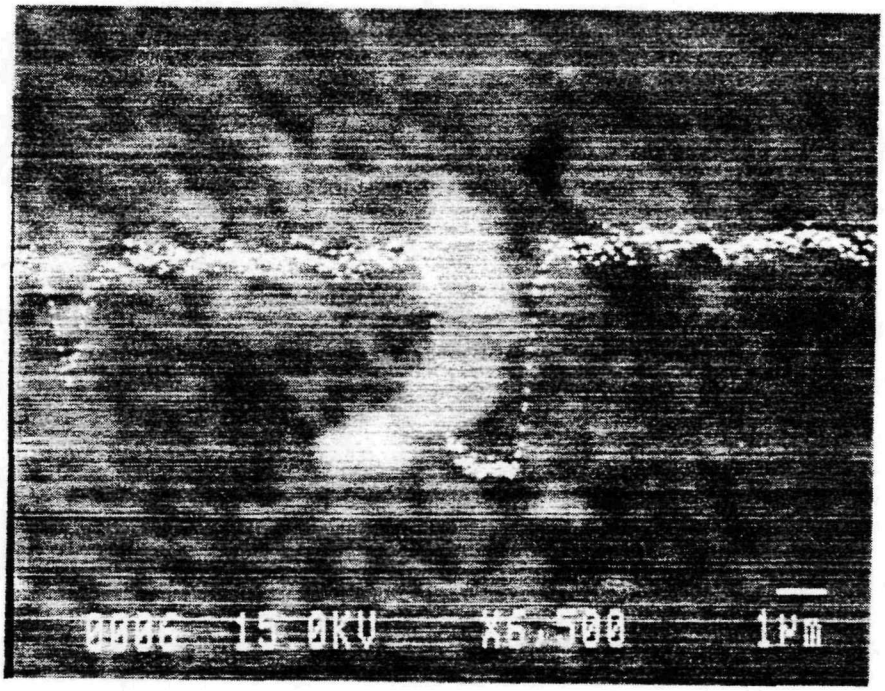

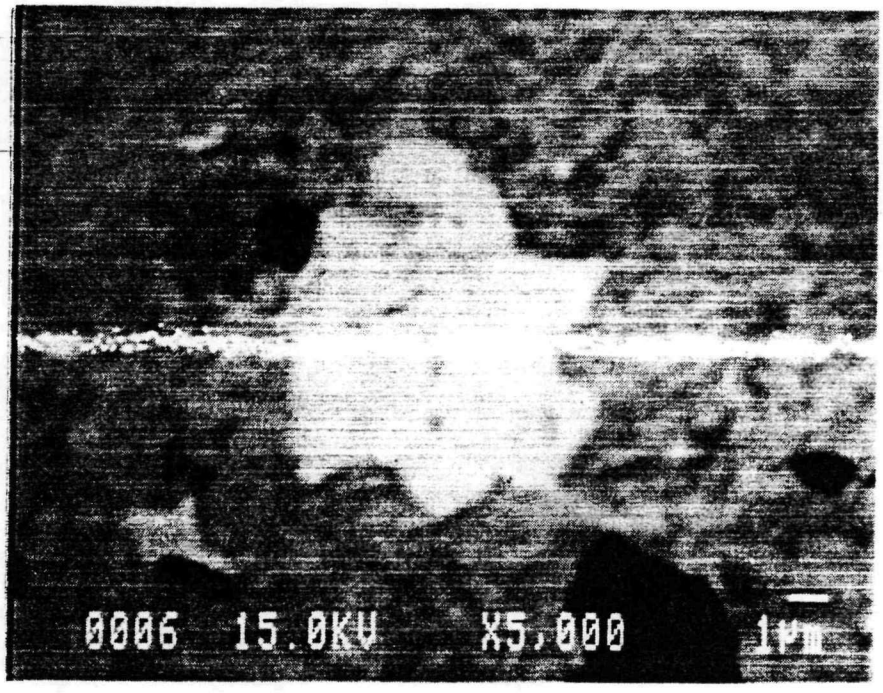

Fig. 1.3.14: Iridium particles in W-(1.0 wt%)Ir-(4.5 wt%)Hf compact sintered at 1200 C for 10 hrs.
(a) tungsten X-ray scan (b) oxygen X-ray scan

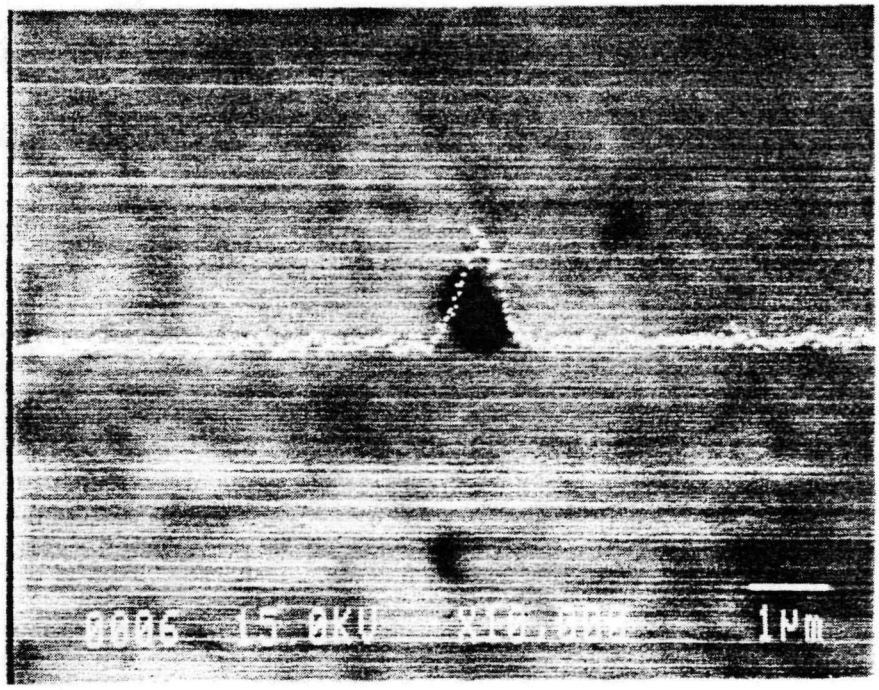

Fig. 1.3.15: Oxygen scans across pores in the sintered matrix
(a) small pore (b) large pore

1.4 MODELLING THE SINTERING PROCESS IN TUNGSTEN

An attempt has been made to study a multi-diffusion model with the ultimate aim of applying it to predict densification in W - based alloy compacts. The mathematical formulation of the model presented by Ashby [11] has been utilized in a computer program which is capable of generating the expected neck size values and hence the corresponding density both as a function of sintering time and temperature. Some interesting features of the model have been studied and their possible effect on our work evaluated.

1.4.1 CONTRIBUTIONS TO DENSIFICATION

In the multi-diffusion model for sintering the various mechanisms that contribute to sintering are categorized in terms of (a) the sources of diffusion i.e. surface sources, grain boundary sources and dislocation sources (b) diffusion route i.e surface diffusion, grain boundary transport (2D) as well as lattice and vapour transport (3D). The total sintering rate is the sum total of the rates corresponding to six mechanisms which are listed below :

(1) Surface diffusion from a surface source.

(2) Lattice diffusion from a surface source.

(3) Vapour transport from a surface source.

(4) Grain boundary transport from grain boundary sources.

(5) Lattice diffusion from grain boundary sources.

(6) Lattice diffusion from dislocation sources.

In figure 1.4.1, the neck size contribution from each type of diffusion source is plotted saperately as a function of homologus temperature. In figure 1.4.2, the total neck size is plotted as a function of homologus temperature for two different powder sizes and two sintering times. In figure 1.4.3, the effect of temperature and powder size is evident in plots of the neck size as a function of time.

In the case of pressureless sintering of annealed powders the contribution due to dislocation sources has been ignored. An immediate effect of this omission is observed in the shape of the neck size-temperature curves. Figures 1.4.4 and 1.4.5 show these modified curves.

1.4.2 INTERPRETATION OF THE CALCULATIONS

The modified curves of densification (i.e. normalized neck size, x/a) obtained from the model indicate the following trends:

(a) For a particular powder size and duration of sintering the densification increases rapidly with temperature upto a particular value of temperature after which the densification remains constant with temperature.

(b) Higher times of sintering result in marginally higher densifications for sintering temperatures below a particular value. For the 0.5 micron W particles this limiting value is 0.45 Tm, as seen in Figure 1.4.4. For temperatures above 0.45 Tm no effect of the duration of sintering is expected.

(c) For a particular duration of sintering, a larger powder size results in lower levels of densification upto a particular sintering temperature. Figure 1.4.5 shows this trend for 0.5 micron and 2.0 micron sizes using a sintering time of 1 hr. In this case we see that above 0.6 Tm the larger powder size shows a marginally higher densification which is contrary to the trend below 0.6 Tm.

1.4.3 COMPARISON OF DATA WITH MODEL PREDICTIONS

The density of pure W compacts obtained from the volume shrinkage data has been plotted in Figures 1.4.6 and 1.4.7 along with the predicted densities obtained from the model. There seems to be a very large discrepency between theory and experiment at the lower temperature of sintering i.e. 1473 K. At the higher temperature of 1703 K, however the experimental values closely approach the theoretical limit at long times of sintering.

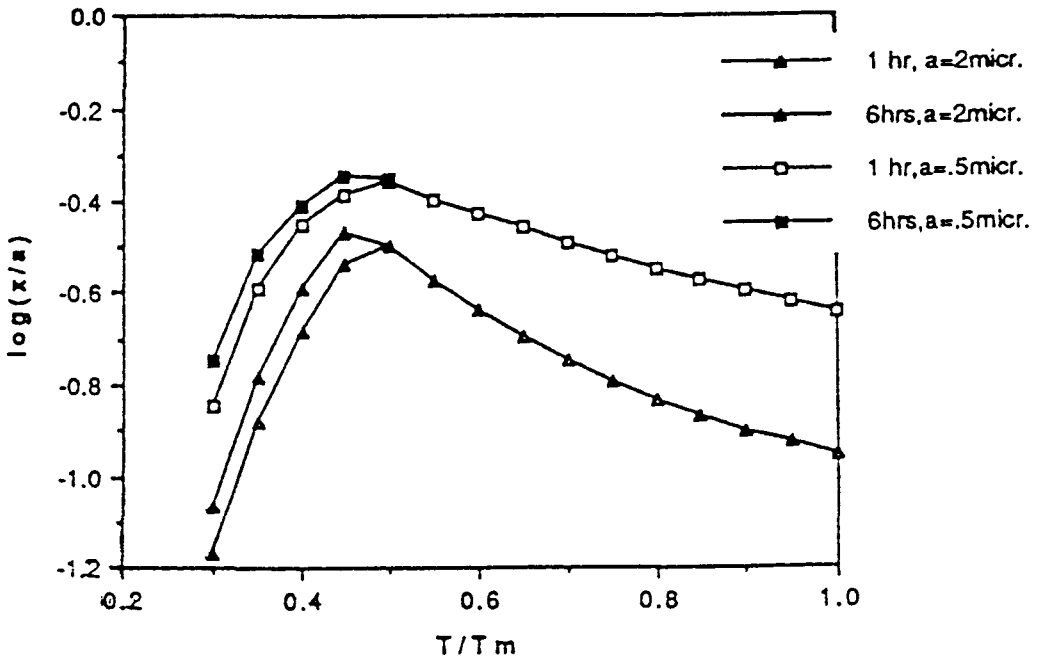

Fig. 1.4.1: Contribution to the neck size by various diffusion sources.

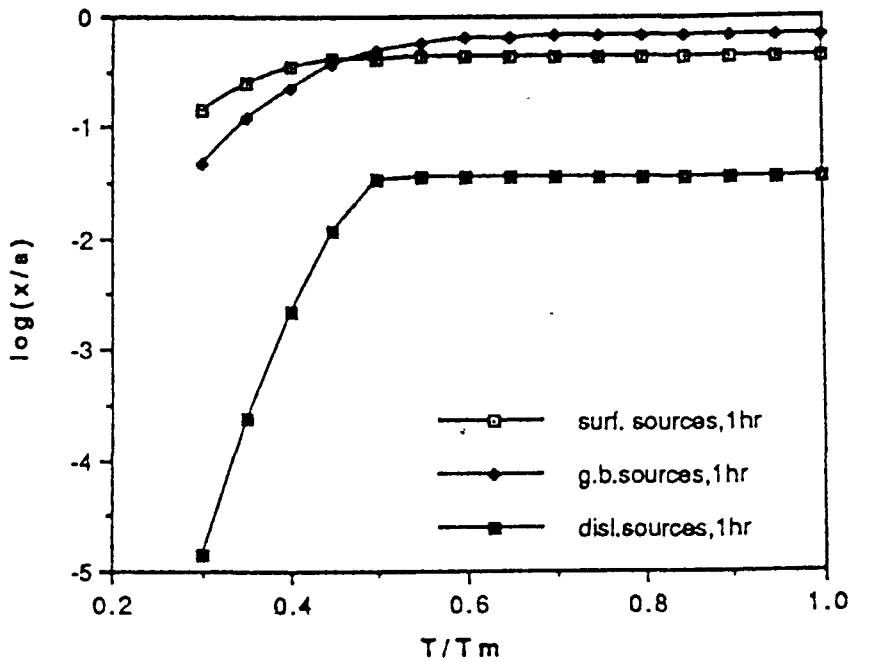

Fig. 1.4.2: Total neck size as a function of homologus temperature for various sintering parameters.

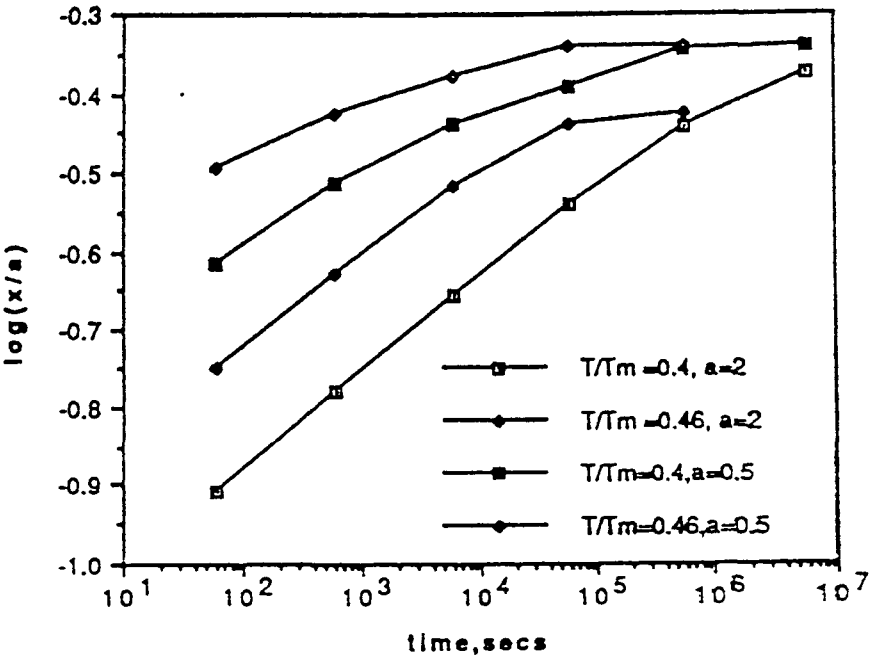

Fig. 1.4.3: Effect of temperature and powder size on the progress of sintering.

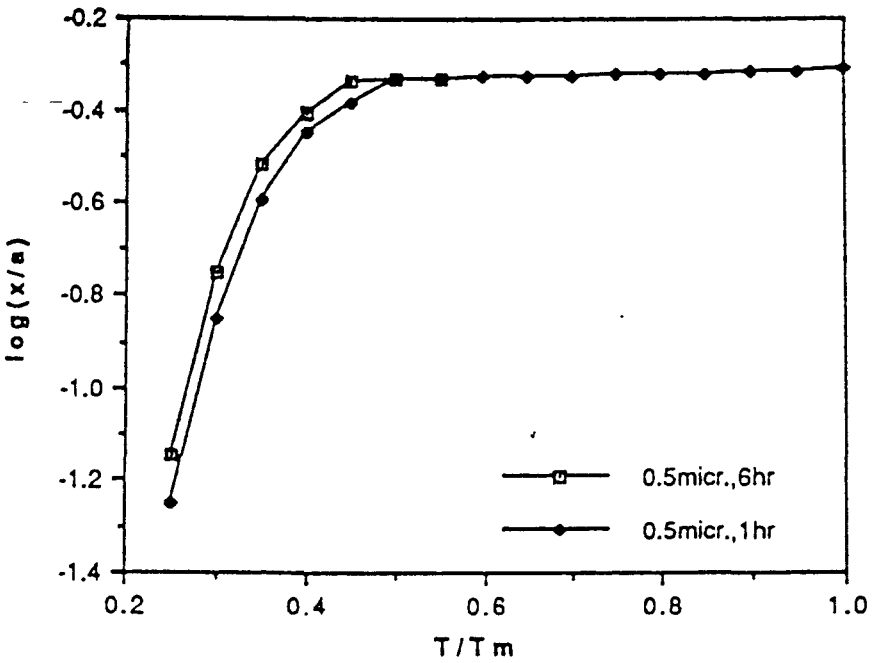

Fig. 1.4.4: Effect of sintering time on the sintering characteristics in absence of dislocation contribution.

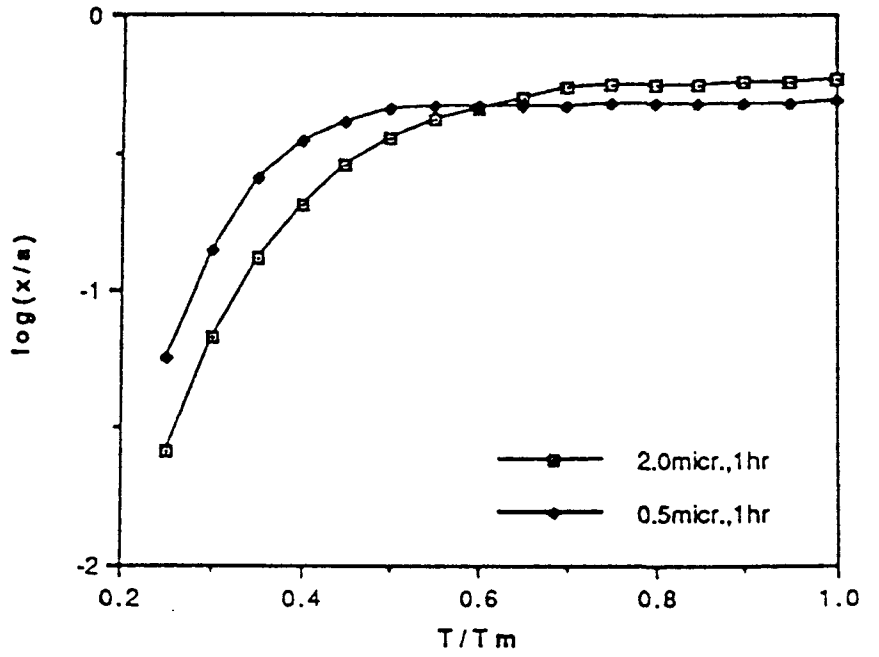

Fig. 1.4.5: Effect of powder size on the sintering characteristics in the absence dislocation contribution.

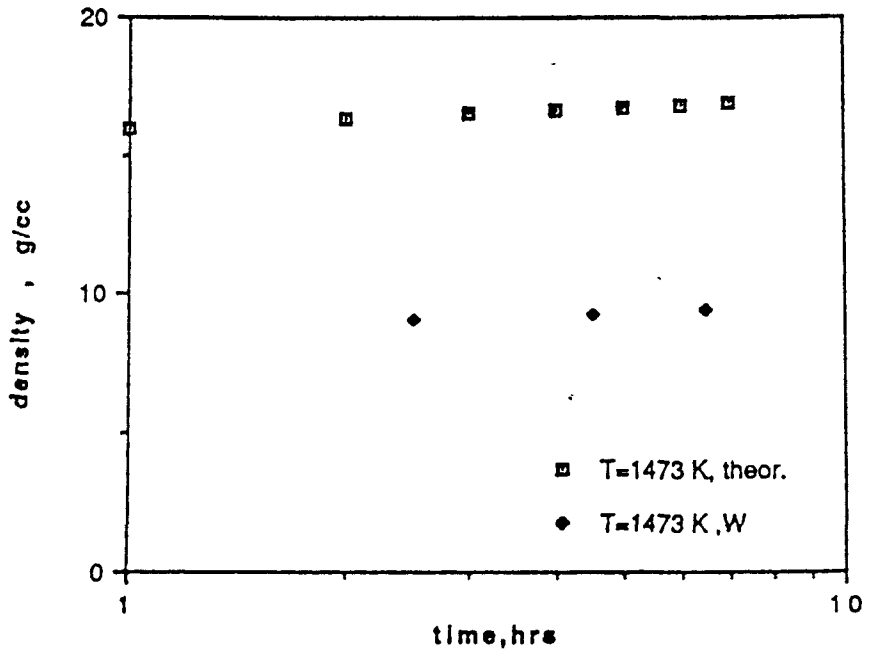

Fig. 1.4.6: Comparison between experimental and predicted densities in pure W (0.5 m) sintered at 1473 K.

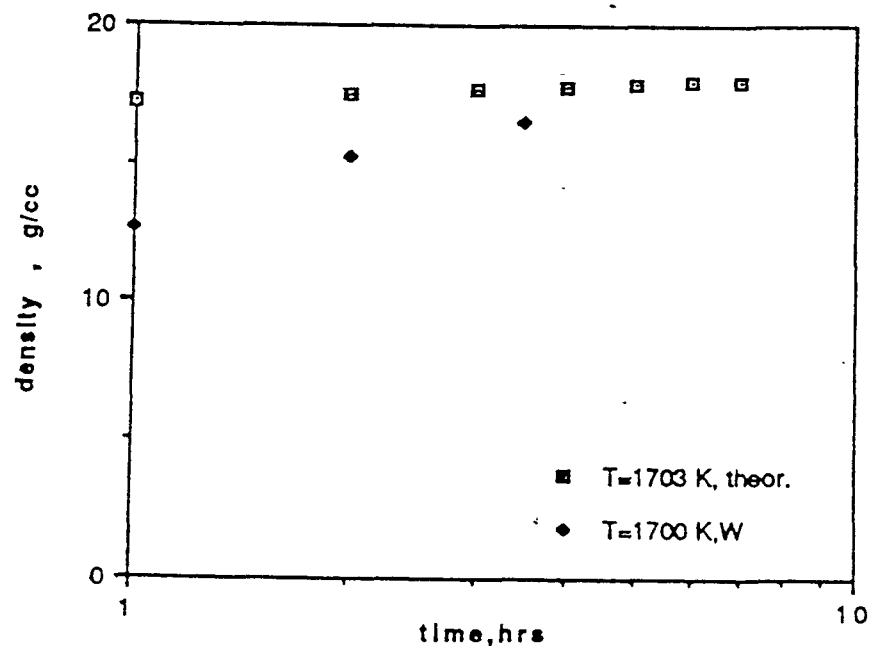

Fig. 1.4.7: Comparison between experimental and predicted densities in pure W (0.5 m) sintered at 1703 K.

APPENDIX 1

A1.0 THEORETICAL ISSUES: ACTIVATED SINTERING OF TUNGSTENALLOYS

A1.1 INTRODUCTION

The following section contains introductory comments pertaining to a comprehensive treatment of Liquid-Phase Sintering by R.M. German [1] wherein sintering has defined as the phenomenon by which packed powders will bond together when heated to temperatures in excess of approximately half of the absolute melting temperature. A common characteristic of all forms of sintering is the reduction in surface area with simultaneous compact strengthening. In a general categorization of sintering techniques, pressure is the primary consideration. Most sintering is performed without an external pressure (pressureless sintering). For several high performance applications, however, high densities are attained using external pressure sources.

The major distinction among pressureless sintering techniques is between solid state and liquid-phase processes. Single-phase, solid state sintering has recieved the greatest consideration from a theoretical stand point. Among the solid state processes there are several options involving second (solid) phases. These include compact homogenization (such as occurs with sintering mixed powders), activated sintering, and mixed phase sintering in the solid state. Activated sintering is the solid state analog to liquid-phase sintering where a second solid phase contributes to rapid interparticle bonding. Mixed phase sintering occurs in an equilibrim two-phase field while homogenization occurs during sintering of mixed powders which form a single phase product.

A1.2 ALLOYING ELEMENTS FOR ENHANCED SINTERING

The effectiveness of an alloying element in increasing the sintering rate depends on the " hetero-diffusion " rate of tungsten in the additive. There is in addition an effect of the electron configurat ion of the added element. Iridium with 5d electrons and good solubility of W , but poor solubility in W is a promising candidate for the activated sintering of tungsten compacts. The increased mass transport rate is further aided by the formation of a low melting second phase layer at the contact regions between particles. The melting point of this second phase layer is a significant factor contributing to the maximal densification of the sintered compact. This has been demonstrated in the work by Li and German [3] who studied the enhanced sintering of tungsten using Ni-Fe-Co additions. In the system of interest here Ir-Th-Hf are expected to act in a similar way to enhance the sintering. The liquid phase expected to form at the particle contacts would be the eutectics corresponding to either of the following systems Ir-Hf , Ir-Th, Th-Hf and W-Ir depending on the compositional homogeniety in the green compact. Table A1.1 shows the approximate eutectic temperatures and compositions obtained from the phase diagrams of the above mentioned systems. These diagrams have been presented in Figures A1.1 to A1.4.

A1.3 SECOND-PHASE FORMATION

Two types of second-phase particles are expected to form during the sintering of the W-Ir-Hf-Th green compacts. The gettering of oxygen and carbon is effected by the highly reactive thorium and hafnium. The resultant refractory compounds HfC and ThO_2, if present in finely dispersed form would increase the strength of the compact considerably.

Eutectic Designation	*Composition (at %)*			*Melting Temp. (C)*
	Ir	*Hf*	*Th*	
A	60.0	26.7	13.0	1500 - 1600
B	57.0	-	43.0	1540
C	62.3	37.7	-	2080

Table Al.l : Eutectic Temperatures and Eutectic Compositions of Tungsten Alloys of Study.

The other type of second phases likely to form are the intermetallic phases predicted by the phase diagrams mentioned in section A1.2 above. A comprehensive list of all the possible intermetallics that appear in these systems have been presented in Table A1.2 along with the corresponding structure data 14]. Unlike the refractory compounds, the formation of intermetallic phases are detrimental to the final strength of the sintered compact. Li and German [3] have shown that high melting temperature intermetallics inhibit the transport of tungsten during sintering by raising the process activation energy. Furthermore, the precipitation of intermetallics during the cooling of the compacts result in severe embrittlement.

A1.4 ROLE OF THE EUTECTIC LIQUID

The formation of a liquid phase around the tungsten particles is capable of enhancing the final sintered density to near theoretical density. The two phenomena of primary importance here are the wetting and spreading of the liquid phase on the tungsten particle surfaces. The completely dispersed liquid results in sufficient internal force through liquid capillary action on the particulate solid that external forces are not required during sintering.

Since complete dispersion of liquid is desired, a natural concern in liquid phase sintering is good wetting. Good wetting depends on a low solid liquid surface energy in comparison with the solid-vapour and liquid-vapour surface energies. Typically, wetting is best when there is a chemical reaction at the solid liquid interface. Such a surface reaction is the reason why reactive metals wet most metal oxides, while noble metals do not.

The tungsten powder particles are covered with oxide films which hinder their solid state sintering properties and result in detrimental strength characteristics in the compact. However, a eutectic liquid composed of Th and Hf, if formed during sintering, would possess superior wetting properties owing to the high affinity of both metals for oxygen. The spreading rate of the liquid is governed by the mechanism of spreading which in turn depends on the surface diffusion (mobility) of the liquid on the solid surface. It has been found that here too the chemical affinity is important for spreading of the liquid on the solid surface. Moreover, solubility between the solid and the liquid phase aids the process too.

A1.5 DEOXIDATION BY ALLOYING

The additives used in the doping of tungsten either restrain recrystallization or help to attain certain properties in recrystallized tungsten. Such measures are necessary because the intra-crystalline strength is lowered by precipitation of minute quantities of oxide at grain boundaries. This problem in tungsten can be overcome either by creating a larger grain boundary area thus diluting the oxide film or by alligning the grain boundaries parallel to the axis of the wire and producing a stable structure. Both these methods of improving the ductility of recrystallized tungsten are applied to metals containing oxide films. It is preferable , however, to eliminate these oxide films altogether

PHASE	*STRUCTURE TYPE*	*PEARSON SYMBOL ; SPACE GROUP*
Hf	W	cI2 ; $Im\bar{3}m$
Hf	Mg	hP2 ; $P6_3/mmc$
$HfIr_3$	$AuCu_3$	cP4 ; $Pm\bar{3}m$
HfIr		orthorhombic
Hf_2Ir	NiTi	cF96 ; $Fd\bar{3}m$
Hf_5Ir_3	Mn_5Si_3	hP16 ; $P6_3/mcm$
Hf_5Ir_3		hexagonal
Hf-O	Mg	hP3 ; $P6_3/mmc$
HfO_2		tetragonal
HfO_2	O_2Zr	mP12 ; $P2_i/c$
HfO_2		oP12 ; $P2_12_12_1$
Hf-W	W	c12 ; $Im\bar{3}m$
HfW_2	Cu_2Mg	cF24 ; $Fd\bar{3}m$
Ir	Cu	cF4 ; $Fm\bar{3}m$
IrTh	BCr	oC8 ; Cmcm
Ir_2Th	Cu_2Mg	cF24 ; $Fd\bar{3}m$
Ir_3Th_7	Fe_3Th_7	hP20 ; $P6_3/mmm$
Ir-W	Mg	hP2 ; $P6_3/mmc$
Ir-W	Cu	cF4 ; $Fm\bar{3}m$
IrtW	AuCd	oP4 ; Pmma
Ir_3W_7	CrFe	tP30 ; $P4_2/mnm$
Th	W	c12 ; $Im\bar{3}m$
Th	Cu	cF4 ; $Fm\bar{3}$

Table A1.2: Structure of Intermetallic Phases

which is best accomplished by alloying with elements having a high affinity for oxygen. Deoxidation as a solid state reaction has not attracted the same interest devoted to deoxidation reactions in the molten state.

Braun and Sedlatschek [5] have systematically investigated the deoxydizing influence of a number of metals and nonmetals. The additives were selected in view of their possible reactions with oxygen entrapped at tungsten grain boundaries leading either to volatilizing or to stabilization in the form of fine dispersions. In this work Hf and Th were among the additives studied. Hafnium and thorium have low solubilities in tungsten and form the most stable oxides during deoxidation of the tungsten particle surfaces. It was found that these additives donot influence the density of the

compacts, the hardness however peaks at 1.0 % of hafnium and thorium due to the dispersion of HfO_2 and ThO_2.

A1.6 THERMODYNAMICS OF SOLID-STATE REACTIONS

The chemical reactions expected to occur during **the eutectic** activated sintering of the W-Ir-Th-Hf compacts could be of the solid-liquid type or the solid-solid type depending on the sintering temperature and the level of compositional homogeniety. The standard free energy calculations for a variety of reactions involving thorium and hafnium with tungsten oxides and carbides can be performed using data from literature [6] .At 1400 C and 1600 C these reactions possess high negative free energies indicating therefore, that these reactions proceed spontaneously at the indicated temperatures. Another implication of this high reactivity of thorium and hafnium is that a eutectic liquid composed of these elements would be expected to efficiently wet and spread on the tungsten particle surfaces. This is because the thermodynamics of wetting and the kinetics of spreading are strongly aided by a chemical reactivity (see section A1.4) between the liquid and the solid particle surface on which the tungsten compounds are present as thin hard layers.

A1.7 KINETICS OF SOLID-STATE REACTIONS

An exact understanding of the mechanism of sintering is possible only with the help of a detailed kinetic analysis performed on a complete array of possible solid-state reactions. Data for such an analysis would come from characterization experiments wherin volume fraction measurements of each reaction product as well as each unreacted additive is obtained. The information obtained from such an analysis is the rate equation that governs each reaction and the relative speeds of these reactions during the sintering process. A systematic methodology for the kinetic analysis of a variety of solid state reactions between powdered reactants was evolved by Beretka [7]. Using linear regression analysis the data from the reactions were fitted into ten equations (models) that usually describe the kinetics of solid-state reactions.

A1.8 CONCLUSIONS

The development of Tungsten-based alloys with high temperature strength emphasizes the importance of processing innovations in the area of materials fabrication. These alloys are best produced by the sintering of powders. However the density attainable in the final compact by the conventional sintering route is inadequate for high temperature strength. Eutectic activated sintering is a process aided by alloying addition that combines the features of liquid phase sintering and solid state activated sintering. Near theoretical densities are attainable by this method of sintering. The present work is directed towards the study of the eutectic activated sintering phenomenon in the W-Ir-Hf-Th alloy system. The investigation will concentrate on the effect of compositional variations on the densification characteristics of the mixed powders and hence the structure and strength of the final compact.

APPENDIX 2

A2.0 FABRICATION ISSUES: COMPACTION AND SINTERING OF TUNGSTEN

A2.1 INTRODUCTION

The fabrication of tungsten alloys in the laboratory involves operations of considerably smaller magnitudes than is encountered in the tungsten industry. However, a good amount of work has gone into the optimization of processing parameters involved in the production of pure tungsten and its alloys much of which is of direct relevence to any processing innovations that might be attempted. This section briefly reviews the information available regarding the compaction and sintering of tungsten compacts and draws from the material presented by Wilkinson [8].

A2.2 PARTICLE SIZE EFFECT

Angular tungsten powders (particles averaging between 1 and 10 microns is usually compacted without a binder, by a hardened steel die or hydrostatically, at 4550 to 45,500 kg/sq.cm (10,000 to 100,000 psi) in plastic containers. Finer powders can be pressed but the particles do not flow uniformily and therefore, they form compacts of non-uniform density. Powders with an average particle size of 2 to 7 microns can be sucessfully compacted into bars of 0.5 in. x 0.5 in. crossection and 16 in. in length provided plunger speeds do not exceed 2.5 mm/ min. during loading and unloading.

Coarse powders (3 to 5 microns) have a particle density of about 19.35 g/cc and a surface area of 0.095 sq.m/gm. Fine powder (1 micron) has a particle density of 19.27 g/cc and a surface area of 0.730 sq.m/gm . The fine powder, in many instances, contains more than twice as much carbon, and about six times as much oxygen. The particle size of tungsten powder produced by hydrogen reduction of tungsten oxide depends on the impurities - including moisture and additives - on reduction temperature and time, and on the type and particle size of the WO_3 .

From an operational stand point, initially the powders are screened in a rotary sifter to remove foreign matter and large agglomerates. The coarse and fine pure tungsten powders are then blended to produce a mixture with maximum compaction characteristics. Handbook data [9] relevent to the parameters for mixing and blending has been presented in Table A2.2

A2.3 EFFECT OF PRESSURE

The use of high pressure lowers the temperature and shortens the time required to convert the fine tungsten powders into compacts of high density. A consequent study of the effects of pressure and temperature on the sintering of small, 5.3 to 5.8 mm (0.21 to 0.23 in.) diameter, compacts of 84% submicron particles of tungsten powder indicates that full densification can be obtained in 20 mins with 30 kbr (435,000 psi) pressure at temperatures of 500 to 1000 C. Since the brittle-ductile transition temperature of tungsten compacts is usually in the range of 300 to 600 C, cracking can be limited by maintaining the temperature well above 600 C while pressure is unloaded.

A pressure survey for 1080 C and 10 minutes revealed a near equivalence of densification pressures in the range of 1 to 30 kbr (14,500 to 435,120 psi), with a sharp break in pressure influence occuring near 1 kbr. When the grain size of the free powder was 0.45 micron, that of the tungsten consolidated at 1000 C had increased only to 0.7 micron; but the rate of grain growth accelerated markedly at 1100 C and the density maximum was near 1050 C. Between peak temperatures of 1000 and 1800 C the density parameter, β , is 0 to 9 for pressureless sintering and 98 to 90 for sintering at 23 kbr (335,600 psi). Here $\beta = 100 . (\rho - \rho_0)/(\rho_T - \rho_0)$, where ρ is the

sintered density, ρ_o is the green density, and ρ_T is the x-ray (theoretical) density. Densification values of sub-micron tungsten powders in excess of 98% can result from parameters as low as 1 kbr peak pressure, 900 C peak temperature, and only a few seconds for coincident time of both peaks.

An evaluation of numerous grades of tungsten powder and of conditions of pressing and sintering led to a procedure for preparing high quality sintered billets with uniform densities in the range of 93% to 95%. In this procedure powder with particles 3 to 4 microns in diameter is hydrostatically pressed at 2465 Kg/sq.cm (35,000 psi) and the resulting compacts are induction sintered for 8 to 10 hrs in hydrogen above 2300 C. The duration of heating can be shortened by raising the sintering temperature - for example, by 300 - 400 C.

A2.4 EFFECT OF IMPURITIES

Maximum metallic impurity specifications for powder metallurgy and for arc-melting do not generally differ widely. Trace metallics below 10 ppm raise the 1-hr recrystallization temperature from 1200 to 1800 C, while 40 to 200 ppm of carbon, 1-40 ppm of oxygen, and < 0.4 to 1 ppm of nitrogen have little effect. Substitutional elements might have a greater effect on high-temperature properties than those that form interstitial dispersions and precipitates.

The ductility of fabricated tungsten is impaired by trace metallics such as 10 to 30 ppm of Ni which increases the tensile transition temperature from 200 to 300 C. Transition temperature behavior is not sensitive to 1 to 15 ppm of oxygen, 2 to 20 ppm of nitrogen, and 1 to 3 ppm of hydrogen, but iron, silicon, aluminium and nickel must be kept at low levels.

A2.5 EFFECT OF SINTERING ATMOSPHERE

The slower the rate of flow of inert gas in an induction furnace the larger the residence time of contaminants (N, Sb, Bi, Si, Mg and Cs) that inhibit the sintering of powders, composed of small crystallites. For a given crystallite size of a powder, a sintering temperature in excess of a certain critical value fixes the grain size so as to inhibit further densification.

A2.6 SIZE EFFECT IN ALLOY PREPARATION

If a constituent of a tungsten alloy has a large particle size, homogeniety by sintering can be dificult. Even at 2000 C a mixture of 80-micron rhenium in 0.5 to 0.6-micron tungsten does not homogenize in 15 hrs. Beside a suitable size distribution of particles to be blended, homogenity requires adequate mixing of powders. Homogeneous mixing with 3 vol % of additives can be achieved by cone blending batches of 350 gms for 2 hrs.

The method of adding inert material can determine whether fine dispersion or segregation will occur. For example, 2 volume % of ZrO_2 or ThO_2 added as a water soluble salt to a slurry of tungsten powder gives a uniform dispersion, but the addition of 1 to 8 micron thoria or zirconia powder causes permanantly segregated patches. The segregated alloys have properties similar to those of unalloyed tungsten, but the uniform alloys have higher recrystallization temperatures and lower ductile-brittle transition temperatures.

Table A2.1 contains the specifications of the powders being utilized in our work.

Element	*Size Range(μm)*	*Purity (%)*
W	8-12	99.995
Ir	≤ 250	99.950
Hf	≤ 44	99.6 (Zr-2.2)
Th	≤ 74	99.8

Table A2.1: Specification of Powders

Degree of mixing = 0.4		
Mixing speed rpm	**Mixing Time min.**	**Total number of revlolutions**
80	3	240
60	4	240
40	8	320
25	17	425
16	30	480
Degree of mixing = 0.06		
80	5	400
60	7	420
40	12	480
Material: red and white sand Mixer: horizontally rotating cylinder		

Table A2.2: Degrees of mixing as a function of revolutions.

References

1. German R.M., Liquid Phase Sintering, Plenum Press, New York, 1985 .
2. Morris J.F., Dilute Solution Ultralloys, AFOSR report 1985.
3. Li C. and German R.M., Metall. Trans. A, 1983, vol. 14A, pp 2031-41.
4. Villars P. and Calvert L.D., Pearsons Handbook of Crystallographic r,ta for Intermetallic Phases, Vols 2,3 ASM, 1985.
5. Braun H. and Sedlatschek K. , J. Less-Common Metals, 2 (1960), 277-291.
6. Schick H.L., Thermodynamics of Certain Refractory Compounds, Vol II, Academic Press Inc., (1966).
7. Beretka J., J. Am. Ceram. Soc., 66 [5] 383-88.
8. Wilkinson W.D., Fabrication of Refractory Metals, Gordon and Breach, New York, (1970).
9. Hausner H.H., Handbook of Powder Metallurgy, Chemical Publishing Co., New York, (1982).
10. Hayden H.W. and Brophy J.H., J. Electrochem. Soc., 110 [7], pp 805-10, (1963).
11. Ashby M.F., Acta Met. , 22, p275, 1974

CHAPTER 2 - TENSILE PROPERTIES OF TUNGSTEN ALLOYS

2.1 INTRODUCTION

The need for structural materials with useful strength above 1600 K has stimulated interest in refractory-metal alloys. Tungsten possesses an extreme high modulus of elasticity (337,400 MPa at 1842 K) as well as the highest melting temperature (3683 K) among metals, and hence has being considered as one of the most promising candidate materials for the high temperature structural applications. Tungsten is particularly well-suited for space Iluclear power systems because of its superior strength at very high temperatures, good resistance to corrosion by liquid alkali metal coolants, and good compatibility with candidate fuel materials. Poor low temperature ductility, especially under the impact loading, is a potential limitation to the usefulness of tungsten. In order to improve the low temperature fabricability and high temperature strength retention, there existed an extensive study on tungsten-base alloys during the two decades prior to the mid-1970s [1-7]. Various approaches, including the purification and alloying, have been employed to alleviate the low-temperature ductility problem and high-temperature strength problem.

More recently, there has been a renewal of interest in the development of tungsten-base alloys for the applications of future aerospace propulsion and space nuclear power systems. Current studies on tungsten-base alloys are basically focused on the investigations of recrystallization temperatures [8], mechanical properties [9], fracture behavior [10], the substructure effect on low-temperature ductility [11], and the criterion for optimum choice of alloying elements [12].

With an atomic radius close to that of tungsten and a relative high solubility in tungsten, rhenium is likely to be an interesting solute for tungsten in alloying. The fact that rhenium additions increase the ductility of tungsten was first reported by Geach and Hughes [13] in 1956, and following study confirmed that rhenium in tungsten could not only reduce the brittle-ductile transition temperature but also improve the high-temperature strength [1, 14]. The ductility improvement of rhenium additions is thought to be associated with the solution softening effect, a low temperature phenomenon resulted from a decrease in the Peierls stress in bcc metals on dilute alloying.

Since the strengthening effects of solid-solution elements on tungsten reduces significantly at temperatures above 0.5 Tm (melting temperature in Kelvin), the dispersion strengthening method is also introduced to the development of tungsten-base alloys. Among various potential second-phase particles, hafnium carbide (HfC) seems to possess both the highest melting point, 4103 K, and the best thermodynamic stability, a free energy of formation of 43 Kcal/g at 1773 K. The studies on W-HfC and W-Re-HfC systems indicated that HfC is the most effective precipitate strengthener in improving the high temperature strength of tungsten without adversely affecting the low temperature ductility [5-7]. Klopp et al. examined the relationship between mechanical properties and HfC content extensively, and found that the maximum strengthening effect occurred at a HfC concentration around 0.35 percent [5].

On the other hand, thoria(ThO_2), a compound having the highest melting temperature (3473 K) among metal oxides, was found to be effective in strengthening tungsten above 1600 K, and the strengthening effect is optimum at the thoria concentration around 1.0 wt.% [9,15,16]. The strengthening effect of thoria additions has been attributed largely to the interaction between thoria particles and dislocations, as well as the retention of cold work to higher temperature than possible with unalloyed tungsten [16]. On the other hand, W-ThO_2 alloys show a poor ductility at room temperature and a weak strength retention at high temperatures. Therefore, it is necessary to utilize the rhenium low-temperature ductilizing effect and high-temperature strengthening effect to develop the W-Re-ThO_2 ternary alloys with a better low-temperature ductility and a superior high-temperature strength.

But so far the study on the mechanical properties of tungstenbase alloys at room-temperature is still rare. And even for W-Re systems, which were the most widely studied tungsten-base alloys, most

investigations on room-temperature mechanical properties in the past were only limited in bending test which is not enough to explain the rhenium ductilizing effect in tungsten. Also, the high-temperature strengthening mechanism of second-phase particles in tungsten-base alloys is not well understood, and the effect of strain rate on the high-temperature tensile properties of tungsten-base alloys is not well documented. Besides, the study on the microstructure and fracture behavior of dispersion strengthened W-Re alloys deformed at either low temperature or high temperature is rare in literature. Except for rhenium, it was suggested that there should exist some other solute elements which could also produce the room-temperature ductilizing effect in tungsten. The search for such beneficial solute elements is, of course, a very important approach to the development of tungsten-base alloys.

Therefore, the present investigations are focused in the following three objectives:

(1) To perform a comprehensive investigation on the microhardness, tensile properties, microstructure, and fracture behaviors of W-Re-ThOz alloys at room temperature to examine whether the solid-solution softening of rhenium is also existed in thoria strengthened tungsten, and find the optimum composition for rhenium ductilizing effect, as well as the fracture characterization of W-Re-ThO_2 alloys.

(2) To investigate the effect of rhenium concentration, temperature, and strain rate on the tensile properties of W-Re-ThO_2 alloys at the temperature range from 1600 K to 2600 K, i.e., 0.45 to 0.70 T_m (melting temperature of tungsten in Kelvin), and examining their fracture behaviors at these temperatures.

(3) To determine the relationship between HfC strength increment and test temperature for a wide temperature range above 0.5 T_m, the coarsening mechanism of dispersed HfC particles and the characteristic temperature at which the rapid coarsening of HfC particles occurs, the applicable dispersion strengthening model, and the contribution of HfC particles to the activation energy for plastic flow in tungsten.

2.2 MATERIALS AND EXPERIMENTAL PROCEDURES

2.2.1 Materials

The swaged P/M tungsten-rhenium alloy, P/M tungsten-thoria alloy, and P/M tungsten-rhenium-thoria alloys, all in the form of a 7.5 mm diameter rod, were provided by Rhenium Alloys Inc., Cleveland, Ohio. These materials were tungsten-26 wt.% rhenium(W-26Re), tungsten-1.0 wt.% thoria (W-1ThO_2), tungsten-3.6 wt.% rhenium-1.0 wt.%thoria(W-3.6Re-1ThO_2), tungsten-ll wt.%rhenium-1.0 wt.%thoria(W-llRe-1ThO_2), and tungsten-26 wt.% rhenium-1.0 wt.%thoria(W-26Re-1ThO_2), These alloys, which the suppliers claimed had a porosity of less than 0.1 %, were sintered from the powders of W, Re, and ThO_2 at a pressure of 2.07 X 10^8 N/m^2 and a temperature of 2500 K in a reducing atmosphere of ultrapure hydrogen. The average grain size of these alloys determined by a linear intercept method was around 60 μm, and the initial thoria particle size determined by the characteristic X-ray mapping was less than 1 μm.

The arc-melted unalloyed tungsten (pure W) and tungsten-3.6 wt.% rhenium-0.26 wt.% hafnium carbide (W-3.6Re-0.26HfC) rods 1.0 inch in diameter used in present investigation were supplied by NASA Lewis Research Center. The chemical compositions of these materials were measured with a microprobe analysis. The average grain size determined by a linear intercept method was 110 μm for W-3.6Re-0.26HfC, and 190 μm for pure W.

The W-Ir and W-Os alloys, used in microhardness tests, were arcmelted in the Materials preparation Laboratory at Arizona State university. The solute concentration in these alloys was varied from 0.1 wt.% to 15 wt.%, and the average grain size was determined as around 60 ~m.

Besides, in order to provide a uniform recrystallized structure, all materials were annealed at high temperature for 30 min. in a vacuum of better than 1.3 X 10^{-5} Pa (10^{-7} torr) prior to testing. The Annealing temperature for all W-Re, W-ThO_2 and W-Re-ThO_2 alloys was 2600 K. Since W-3.6Re-0.4HfC and pure W had a relative large initial grain size, the annealing temperatures for these two alloys were lower than that for W-Re and W-Re-ThO_2, i.e. 2450 K for W-3.6Re-0.26HfC, and 2300 K for pure W.

2.2.2 Experimental Procedures

Room-temperature tests included hardness test and tensile test. Hardness test was performed on a Tukon Microhardness tester, and the hardness value obtained on each alloy was the average of at least ten readings. Room-temperature tensile test were performed on an Instron tensile testing machine. Plate-type specimen, with a gage lengths of 8.0 mm, was first mechanically polished with 400 and 600 grit emery papers, and then chemically polished with a 10% NaOH solution. Since the tensile elongation of tungsten-base alloys was relative small at room temperature, a projection method in which the size of pose-test specimen was magnified at X50 was used to measure the final specimen gage length. In order to determine the reduction in area (RA) accurately, the final fracture area of tensile specimen was measured with a scanning electron micros,cope at a magnification of X100.

High-temperature tensile tests were performed in an ultra-high vacuum test chamber mounted on an Instron tensile testing machine. The tensile specimens, which had the same gage length and the same polishing treatment as those used in room-temperature tensile test, were heated with self-resistant heating by passing a direct current through the specimen, and the test temperatures were measured with an optical pyrometer calibrated to have an uncertainty less than 5 K in the whole temperature range employed ill the present study. All tensile tests were performed at a strain rate of 10^{-3}/sec to 10^{-2}/sec in a vacuum better than 1.3 X 10^{-5} Pa (10^{-7} torr).

The testing temperature range for high-temperature tensile tests was 1700 K to 2700 K for pure W, 1600 K to 2600 K for W-Re, W-ThO_2, and W-Re-ThO_2 alloys, and 1950 K to 2980 K for W-3.6Re-0.26HfC. The purpose of employing extreme high testing temperature to W-3.6Re-0.26HfC was to examine the HfC particle thermal stability at high temperatures. Besides, in order to understand the HfC particle growth mechanism, each W-3.6Re-0.26HfC specimen was held at the particular test temperature for 15 min. prior to performing the tensile test.

Both side and fracture surfaces of all tested specimens were examined with a JEOL 840 scanning electron microscope. The TEM specimens, which were cut from the near-fracture-tips of post-tested tensile specimens, were examined with a 2000 FX high-resolution transmission electron microscope at a magnification of 50,000. For the convenience of theoretical analysis, a cubic SPLINE interpolating method [17] was used in the calculations of HfC strength increment, and a linear regression treatment was used in the calculations of strainrate exponent, activation volume, and activation energy for plastic flow.

2.3 ROOM-TEMPERATURE MECHANICAL PROPERTIES OF TUNGSTEN ALLOYS

2.3.1 Hardness

In Fig. 2.1, the vickers hardness of W-Re-ThO_2 alloys is plotted as a function of rhenium content. For the purpose of comparison, the hardness of swaged P/M W-Re alloys [8], which were provided by the same company as those used in present study and prior annealed at 2500 K, is also shown in this figure. It is easy to see that a small amount addition of rhenium in thoriated tungsten could significantly reduce the hardness. And a maximum hardness reduction about 16 percent was observed at rhenium concentration of 3.6 pct, almost the same concentration where maximum softening occurs in W-Re. This confirms that rhenium solid-solution softening also exists in thoriated tungsten. And the softening mechanism for W-Re and W-Re-ThO_2 would be similar because the softening occurs at almost the same rhenium concentration. Besides, by comparing the hardness of W-Re-lThO_2 and W-Re, it was found that the 1 pct thoria in tungsten resulted a near-uniform increase in hardness which was basically not related to rhenium concentration. This means that thoria acts as an independent strengthening element in tungsten and does not interfere with the rhenium solid-solution softening effect.

The solid-solution softening effect occurred at temperature below about 0.2 T_m (melting temperature in Kelvin) in bcc metals was well reviewed by Pink et. al [18] who suggested that the free-electron concentration, i.e. the outer-orbit electron configuration, would significantly affect the Peierls stress encountered by moving dislocations. Transition metals with unfilled and non-spherical d orbits bring about covalent binding, which can result in large Peierls stress; however, filling the d orbit with electron, such as rhenium in tungsten, is supposed to decrease the Peierls stress because the condition of forming covalent binding is no longer existed. If this is true, other elements on the left of tungsten in the periodical table, such as osmium and iridium, are expected to show the similar solidsolution softening effect in tungsten as rhenium does. A comprehensive study on the hardness of W-Ir alloys is currently underway here at Arizona State university, and the primary result confirms that there indeed exists a hardness minimum at particular solute concentration for W-Ir alloys. The solute concentration where maximum solution softening occurs is around 0.45 wt.% Ir for W-Ir alloys, as shown in Fig. 2.2. Since the solubilities of Ir and Re in W at room temperature are 1 wt.% and 10 wt.%, respectively, the solute concentration resulting maximum solution softening seems in proportional to its solubility in tungsten, i.e. the maximum softening always occurs at a solute concentration around 40-60 percent of the solubility of given solute in tungsten.

2.3.2 Tensile Properties

The ultimate tensile strength (UTS) and yield strength (YS) of W-Re-ThO_2 alloys at room-temperature as a function of rhenium content are shown in Fig. 2.3. Because of the solution softening, a decrease in both tensile strength and yield strength was observed at few percent rhenium, while yield strength was decreasing in a rather faster rate than tensile strength. The softening was limited to a strength minimum at rhenium concentration around 3.6 pct and was followed by solution strengthening at higher rhenium contents. According to the result shown in Fig. 2.3, it is expected that up to 7 wt.% addition of rhenium in thoriated tungsten would reduce the yield strength at room temperature. Similar phenomenon was observed by Raffo [19] in W-Re alloys at 77 K, where the rhenium addition up to 9 at.% in tungsten resulted a decrease in yield strength.

As mentioned earlier, the room-temperature ductility is one of the most concerned mechanical properties of W-Re-ThO_2 alloys. Fig. 2.4 shows the tensile elongation and reduction in area (RA) as a function of rhenium content. As expected, a maximum ductility about 8% was found at

rhenium concentration around 3.6 pct. present result, therefore, confirms that the rhenium ductilizing mechanism found in pure tungsten is also effective in thoriated tungsten. But there still exist some differences. For example, in W-Re systems the maximum rhenium ductilizing effect occurs both at low-rhenium concentration about 4 pct and at a high concentration greater than 20 pct [14]; while in W-ReThO_2 systems the ductilizing effect occurs at low-rhenium concentration only. According to Klopp et al.'s explanation [14], the ductilizing effect at low-rhenium concentration was associated with the dilute solution softening, and ductilizing effect at high-rhenium concentration was associated with the presence of an intermediate sigma phase which's nuclei were postulated to provide stress concentration sites that could act as sources for dislocations and twins. If this is the case, the dispersed thoria particles in W-Re-ThO_2 alloys could also be considered as the source of dislocations. At low rhenium concentration, these dispersed particle may act in the same way as sigma phase nuclei so that the ductilizing effect becomes more remarkable. At high rhenium concentration, too many dislocations are introduced by both dispersed thoria particles and sigma phase nuclei. Because the dislocation density is so high that the dislocations created by these sources are hard to move. Hence, no obvious ductilizing effect could be observed at high rhenium concentration. This strong solution strengthening at high rhenium concentration was also confirmed by the microstructure of W-26Re-1ThO_2 discussed elsewhere.

Except for the general theory of solid-solution softening in bcc metals, several other mechanisms were suggested to explain the particular rhenium ductilizing effect in tungsten. Typical mechanisms are following:

1. Rhenium additions produce a complex oxide with appreciable surface tension. Instead of wetting grain boundaries, the oxide agglomerates into round globules so that the intergranular strength and ductility are improved [20,21].

2. Interstitial solubility, essentially that of oxygen, is lowered by rhenium so that the number of barriers to dislocation motion inside of the grains is significantly reduced [22,23].

3. The stacking fault energy of tungsten is reduced by rhenium additions, resulting in easier twinning [24,25].

However, the third mechanism was controversy because twinning only accounts for a minor fraction of the plastic deformation, usually at the onset of macroscopic strain, witll slip contributing to the remainder. Considering the thoria strengthening effect observed at temperature above 1600 K [9,15,16], it is expected that a combination of particle strengthened tungsten with proper rhenium additions would be the most promising approach to develop tungsten-base alloys with superior low-temperature ductility and excellent high-temperature strength.

2.3.3 Fracture Behaviors

The room-temperature fractographs of W-Re-ThO_2 alloys are shown in Fig. 2.5. It seems that all four fractographs are similar. The intergranular fracture is the dominant fracture mode for W-Re-ThO_2 alloys, indicating that the microcrack is most likely initialized at grain boundaries and propagated along the weak interface. But some difference can still be found by a careful view of these fractographs.

First, not all fracture surfaces are along grain boundaries. There existed more or less some area where transgranular fracture occurred. Second, the area of transgranular fracture was changing depend upon the rhenium concentration. The W-1ThO_2 without rhenium had the least transgranular fracture area. When rhenium was added to W-1ThO_2, the transgranular fracture area was first increased, and then decreased once the rhenium reached a very high concentration. In order to discuss this phenomenon quantitatively, we may use the fraction of transgranular fracture (FTF),

i.e. the ratio of transgranular fracture area to total fracture area. Fig. 2.6 shows the fraction of transgranular fracture as a function of rhenium content. Now it is easy to see that all W-Re-ThO_2 alloys have a higher FTF value than W-ThO_2 alloy, and the FTF reaches its maximum, about 0.23, at the rhenium concentration of 3.6 pct. Since the transgranular fracture implies that the strength of grain boundaries is stronger than that of interior-grain, the increase of FTF resulted from rhenium additions indicates that rhenium does improve the intergranular strength at room temperature by the possible mechanism that rhenium changes the oxide morphology along grain boundaries as suggested by Jaffee et. al [20,21]. Certainly, rhenium will increase the interior-grain strength by solution strengthening at the same time. But this strengthening is not as strong as that of some given grain-boundaries at low rhenium concentration so that we could still observe some transgranular fracture area on fracture surface. At very high rehnium concentration, on the other hand, the solution strengthening of interior-grain is so strong that interior-grain strength is again larger than that of grain boundaries. The FTF, of course, is supposed to be reduced in such case.

2.3.4 Conclusions

(1) Rhenium solid-solution softening exists in thoriated tungsten. The minimum hardness and yield strength are observed at the rhenium concentration of 3.6 pct.

(2) Iridium and osmium softening exist in tungsten. The minimum hardness is observed at the iridium concentration of around 0.4 pct for W-Ir alloys.

(3) Rhenium addition can significantly improve the roomtemperature ductility of thoriated tungsten. The optimum rhenium concentration for this purpose is between 3 to 11 pct.

(4) Intergranular fracture is the dominant fracture mechanism of W-ThO_2 and W-Re-ThO_2 alloys at room temperature. But the W-Re-ThO_2 alloys shows a higher fraction of transgranular fracture than W-ThO_2.

2.4 HIGH-TEMPERATURE TENSILE PROPERTIES OF W-Re-ThO_2 ALLOYS

2.4.1 Strength Properties

Fig. 2.7 shows the 0.2% offset yield strength of W-Re-lThO_2 alloys as a function of rhenium content above 1600 K. similar to most alloy systems, the yield strength of these alloys decreased with the increasing temperature over the entire temperature region, but the high-rhenium alloys showed a higher decrease rate than the lowrhenium alloys. When temperature increased from 1600 K to 2600 K, for example, the yield strength of W-3.6Re-lThO_2 reduced 67 pct, while the yield strength of W-26Re-lThO_2 reduced 85 pct. It can be seen from Fig. 2.7 that the addition of rhenium in thoriated tungsten had a varying strengthening effect depend upon the temperature. At temperatures up to 2000 K, the rhenium strengthening effect was rather significant, and the strength increment was in proportional to the rhenium content. At 2000 K, for example, W-3.6Re-lThO_2 had a yield strength of 160 MPa, comparing with 109 MPa of W-lThO_2, while W-llRe-lThO_2 had a value of 185 MPa, much higher than that of W-lThO_2. From 2200 K to 2400 K, on the other hand, the strengthening effect of rhenium decreased rapidly. In this temperature range, the yield strength was first increased with increasing rhenium conteIlt, and then almost kept as a constant once the rhenium content reached 11 pct. At 2600 K, the strengthening effect of rhenium was so small that it could be negligible.

It is well known that the solid-solution strengthening comes from the interaction between soluted atoms and dislocations. G.E. Dieter [26] indicated six mechanisms by with the soluted atoms could interact with dislocations. Of these various mechanisms, there are only two mechanisms are relatively insensitive to temperature and continue to act up to about 0.5 Tm (the melting point of base metal in Kelvin). One is the elastic interaction arisen from the mutual interaction of elastic stress fields which surround misfitting soluted atoms and the edge dislocation core. Another one is the modulus interaction which occurs when the presence of soluted atoms locally alters the modulus of the matrix. In present case, it appeared that both mechanisms played the important roles in the rather strong solid-solution strengthening effect of rhenium in W-ThO_2 up to 2000 K.

Similar trend was observed in the effect of rhenium on the ultimate tensile strength, as shown in Fig. 2.8. Here it was also found that the rhenium strengthening was effective up to 2000 K, and the strengthening effect became relative small above this temperature. At 2400 K, the tensile strength of W-3.6Re-lThOl and W-llRe-lThO_2 was almost the same as that of W-lThO_2, and the tensile strength of W-26RelThO_2 was even lower than that of W-lThO_2. The rapid decrease in tensile strength of high rhenium alloy above 2400 K may be explained in the effects of rhenium on the interior-grain strength and intergranular strength. According to the W-Re phase diagram [27], the rhenium addition in tungsten will largely lower the melting temperature. With a rhenium concentration of 26 pct, for example, the magnitude of melting point decrease could be as high as 350 K. This implies that at given temperature W-Re has lower atomic bonding energy than pure W. If the solution strengthening effect is not strong enough to compensate the decrease in bonding strength, such as the case at very high temperatures, the interior-grain strength would be decreased. On the other hand, the intergranular segregation of rhenium which was observed in other systems may further lower the melting temperature locally at grain boundaries and also promote the formation of microvoids, resulting the serious grain-boundary sliding and intergranular rupture.

From Fig. 2.7 and Fig. 2.8, it can be seen that the difference between yield strength and ultimate tensile strength varied depend upon both the rhenium content and temperature. Taking the W-llRe-lThO_2 as an example, the magnitude of strength difference decreased from 66 MPa at 1600 K to less than 10 MPa at 2600 K. This is most likely caused by a decreasing work hardening rate. The work hardening behavior of a material is generally expressed by the strain-hardening exponent n given by following equation

$$\sigma = K \varepsilon^n \tag{2.1}$$

where σ and ε indicate the true stress and true strain in an axial tensile deformation process, respectively. The constant K is known as the strength coefficient of a material. The strain-hardening exponent n, which is a function of material, microstructure, temperature, and strain rate, has an important meaning in the evaluation of plastic deformation behavior of a material. The n value provides an empirical parameter for appraising the relative stretch formability, and particularly, a measurement of the effectiveness of alloying strengthening in alloys. A large value of n indicates high work hardening capability and therefore, a high resistanCe to further plastic deformation.

Fig. 2.9 shows the effect of temperature and rhenium concentration on the strain-hardening exponent of W-Re-ThO_2 alloys. In agreement with most alloy systems, with increasing temperature, all these four alloys showed a continuous decrease in strain-hardening exponent, which reduces from a value around 0.45 at 1600 K to a value smaller than 0.2 at 2600 K. On the other hand, two phenomenon were found in the contribution of rhenium concentration on the n value. First, both W-llRe-lThO_2 and W-26Re-lThO_2 showed a similar workhardening rate in whole temperature range. The n values of these two alloys were higher than that of W-lThO_2 up to 2200 K, and kept almost the same as that of W-lThO_2 above this temperature, which is consistent with the observed strength properties discussed previousiy. Second, a small amount addition of rhenium around 3.6% in tungstenthoria alloy had an effect in decreasing the strain-hardening rate, indicating that the maximum rhenium ductilizing effect found in pure tungsten at rhenium concentration around 4 pct is also valid in thoriated tungsten.

One of the parameters in evaluating the material performance at high temperatures is the activation energy of deformation. Similar to the activation energy of deformation, this quality represents the energy needed for dislocation overcoming the barriers in its slip plane. A higher activation energy of deformation implies that t}lere exists a stronger interaction between dislocations and dispersed barriers, and therefore, the material possesses a better strength retention at high temperatures. The activation energy of deformation can be experimentally determined at a constant strain rate by following expression [26]

$$\sigma_y = A \exp(Q/RT) \tag{2.2}$$

where Q is the activation energy of deformation, σ_y is the yield stress, A is a strength coefficient, and R and T have their usual meanings. Using this expression, a plot of $\ln(\sigma_y)$ versus l/T will give a straight line with a slope of Q/R. From the results shown in Fig. 2.7, it was found that the increment of activation energy was in proportion to the rhenium concentration. And the linear relationship between the Q value, in an unit of Kcal/mole, and rhenium content can be approximately expressed as

$$Q = 12.61 + 0.0475\ Re(wt.\%) \tag{2.3}$$

2.4.2 Ductility

In Fig. 2.10, the tensile elongations of W-ThO_2 and W-Re-ThO_2 alloys are plotted as a function of rhenium content at various temperatures. The increasing temperature always result in a higher ductility. And it is found that the addition of rhenium could significantly improve the high-temperature ductility of thoria strengthened tungsten, especially at the rhenium concentration around 11 pct.

In order to find the high-temperature deformation mechanisms of these alloys, side surfaces of deformation zones were examined using SEM second electron imaging. It was found that the interior-grain deformation was the dominant deformation mechanism for these alloys at temperature below 2000 K. Fig. 2.11 shows the side surfaces of all four alloys tested at 1800 K. Obvious slip bands, appearing in almost 45 degree to the tensile loading axis, were observed on the side surfaces of the specimens tested at this temperature, and the number of slip bands increased with increasing rhenium content, reached a maximum value at the rhenium concentration of 11 pct, and then decreased with further addition of rhenium. From this observation, it appears that rhenium addition up to 11 pct in W-1ThO_2 is beneficial in promoting the dislocation slip and improving the ductility from 1600 K to 2000 K, but further increase in rhenium concentration beyond 11 pct would be harmful to the ductility because of the strong solid-solution strengthening effect at very high rhenium concentration in this temperature range. Considering the previous reports that a rhenium concentration about 4 pct in tungsten would result the maximum ductilizing effect at room temperature[2, 6, 31], it is interesting to note the ratios of optimum rhenium concentration where maximum ductilizing effect occurs to the rhenium solubility are almost the same both at room temperature and at high temperatures, i.e. 4 pct to 12 pct at 298 K, and 11 pct to 28 pct at 1800 K.

At temperature above 2000 K, on the other hand, the intergranular deformation was found to be the dominant deformation mechanism, and serious grain-boundary sliding was observed from 2200 K to 2600 K. Fig. 2.12 shows the typical side-surface morphological pictures of specimens tested at 2400 K. The W-Re-ThO_2 alloys showed more widely grain-boundary sliding than W-ThO_2 alloy. It appears that rhenium addition in thoria strengthened tungsten can promote the grainboundary sliding with a possible mechanism that segregated rhenium atoms forms the rhenium-rich regions with low melting temperature locally at grain boundaries so that the intergranular strength is reduced. The grain-boundary segregation of rhenium was observed by Booth in Co-Re alloys [28], these segregated rhenium atoms could promote the microcrack propagation along grain boundaries, and hence lower the intergranular strength. With increasing temperature, both intergranular strength and interior-grain strength are continually decreased. But former reduces in a faster rate because of the grain- boundary segregation of rhenium, once the intergranular strength is lower than interior-grain strength, deformation mostly concentrates at grain boundaries and intergranular sliding becomes the main mechanism for the high-temperature deformation.

According to above discussion of strength properties and ductility, it seems that W-11Re-1ThO_2 possesses the optimum combination of strengthening effect and ductilizing effect among all alloys investigated here at high temperatures. And further increase in rhenium content beyond 11 pct could result an unexpected deterioration in tensile properties because of the rapidly weakened grain boundaries confirmed in the fractographic study described at the end of this paper.

2.4.3 Effect of Strain Rate

As mentioned earlier, one of the deterrents to the applications of tungsten lies in its high strain-rate sensitivity, which in turn results in a poor material performance under the impact load. Therefore, it is necessary to examille the effect of strain rate on the tensile properties of W-Re-ThO_2 alloys at high temperatures. Figs. 2.13 and 2.14 shows the strength and elongation of W-3.6Re-1ThO_2 and W26Re-1ThO_2 as a function of strain rate at 2000 K. It is easy to see that the tensile properties of high-rhenium alloy are more sensitive to the change in strain rate than those of low-rhenium alloy at high temperature. When strain rate increased from 10^{-3}/sec. to 10^{-2}/sec. at 2000 K, for example, the elongation of W-3.6Re-1ThO_2 only decreased 16 pct, while a reduction of 42 pct in elongation was observed in W-26Re 1ThO_2. At the same time, the tensile strength of W-3.6Re-1ThO_2 had an increase of 72 MPa, but that of W-26Re-1ThO_2 increased as much as 156 MPa, more than double the strength increment of W-3.6Re-1ThO_2.

A general relationship between flow stress σy and strain rate $\dot{\varepsilon}$ at constant temperature can be expressed by the power law [29]

$$\sigma_y = C\,(\dot{\varepsilon})^m \tag{2.4}$$

where C is a material constant, and m is the strain rate sensitivity. The m value is important in the evaluation of material performance under dynamic impact loading, and it also provides a key link between the dislocation concepts of plastic deformation and the more macroscopic measurement made in the tensile test. If the power law is obeyed, a plot of $\log(\sigma_y)$ versus $\log(\varepsilon)$ will give a straight line with the slope of m. Fig. 2.15 shows such a plot for W-3.6Re-lThO_2 and W-26Re-lThO_2 at 2000 K. The strain-rate sensitivities of these two alloys were calculated by a linear regression treatment as 0.157 and 0.247, respectively. The m values obtained in present study are the indications that the W-26Re-lThO_2 is indeed much more sensitive to the varying strain rate than W-3.6Re-lThO_2 at high temperatures. A strain-rate sensitivity of 0.15 at high temperature was determined by King et al.. in a P/M W-lThO_2 alloy [15], the comparison between their data and present results suggests that the addition of rhenium could increase the strain-rate sensitivity significantly at high temperatures, and therefore should be avoided if the material is to be used under the dynamic loading conditions.

Another effective parameter used to evaluate the effect of strain rate on the deformation behavior of a material at high temperatures is the activation volume V* given by the expression [30]

$$V^* = kT\,(d\ln(\dot{\varepsilon})\,/d\ln(\tau)) \tag{2.5}$$

where k is the Boltzman constant, T is the absolute temperature, and τ is the shear stress. The activation volume is a measurement of the maximum space in where a dislocation may overcome various barriers during its motion process under thermal activation. The V* values of W-3.6Re-lThO_2 and W-26Re-lThO_2 at 2000 K were determined as 8.83×10^{-22} cm^3 and 1.79×10^{-21} cm^3, or 87 b^3 and 43 b^3, respectively. Where b is the Burgers vector of tungsten. According to Krausz et al.. classification [30], for such magnitudes of activation volume, both Peiers-Nabarro mechanism and cross-slip mechanism could be the rate controlling mechanisms in the deformation process of these two alloys. The transmission electron micrographs of post-test specimens confirmed that cross-slip did exist in W-Re-ThO_2 alloys deformed at high temperatures.

2.4.4 Fracture Behaviors

In order to find the fracture mechanisms of W-Re-ThO_2 alloys, the fracture surface of every post-test specimen was examined with a scanning electron microscope. There existed three different fracture modes depend upon the particular test temperature and rheniumconcentration.

They were intergranular fracture, transgranular fracture, and mixed fracture mode. Voids were observed on the fracture surfaces at temperature above 2000 K, and it was also found that the varying strain rate did not change the fracture mode.

Fig. 2.16 shows the high-temperature fracture mode of W-Re-ThO_2 alloys as a function of temperature and rhenium content. Two interesting facts can be found in this figure. First, at given rhenium concentration the fracture morphology transfers from intergranular mode to transgranular mode with increasing temperature. Second, at given temperature the fracture mode transfers from transgranular one to intergranular one with increasing rhenium concentration. The second fact observed leads to an important conclusion that rhenium addition in thoriated tungsten would significantly lower the grain boundary strength, as observed in the tensile properties and deformation behaviors, and result the intergranular fracture at high temperatures. According to the

tungsten-rhenium phase diagram, the melting point of W-Re alloys decreases continuously with increasing temperature. This implies that tungsten with high rhenium concentration possesses lower bonding energy than those with low rhenium concentration for given temperature. Deformation at 2200 K, for example, means a deformation at about 0.61 T_m for W-3.6Re-lThO_2, 0.64 T_m for W-llRe-lThO_2, or 0.67 T_m for W-26Re-lThO_2. Since the rhenium solution strengthening is very small at 2200 K the tungsten-base alloys with higher solute concentration, of course, should have a relatively rapid decrease in strength. Furthermore, a higher strength reduction is supposed to occur at grain boundaries if there exists the solute grain-boundary segregation. This reduction in grain-boundary strength in turn leads to the easy rupture along grain boundaries, and the rapid deterioration in tensile properties at temperature above 2000 K. W-26Re-lThO_2 is a typical one for such case as discussed earlier.

2.4.5 Conclusions

(l) Rhenium strengthening in thoriated tungsten is effective up to 2000 K, and the strengthening effect is in proportion to the rhenium concentration below this temperature.

(2) 11 pct addition of rhenium in thoriated tungsten can lead to the best combination of tensile properties at high temperatures.

(3) Activation energy of deformation, Q value, is in proportion to the rhenium concentration, and lhe Q value in the unit of Kcal/mole can be expressed as Q = 12.61 + 0.0475 Re (wt.%)

(4) The dominant deformation mechanism of W-Re-ThO_2 alloys is interior-grain dislocation slip below 2000 K, and is the grain-boundary sliding above 2000 K.

(5) The strength and ductility of W-26Re-lTh02 are much more sensitive to strain rate than those of W-3.6Re-lThO_2. At 2000 K, W-26Re-lThO_2 has a strain-rate sensitivity of 0.247 and an activation volume of 43 b^3, while W-3.6Re-lThO_2 has the values of 0.157 and 87 b^3 respectively.

(6) Rhenium in thoriated tungsten will lower the grain-boundary strength. The trend of Intergranular fracture increases with increasing rhenium concentration and temperature.

2.5 EFFECTS OF THORIA ON THE TENSILE PROPERTIES OF W-26Re ABOVE 1600 K

2.5.1 Strength and Ductility

The 0.2 % offset yield strength of W-26Re-1ThO_2 and W-26Re deformed at a strain rate of 10^{-3} /sec from 1600 K to 2600 K is shown in Figs. 2.17. The yield strength of both materials decreased with increasing temperature over the entire temperature region. And the results indicated that the 1 w/o thoria addition had a modest strengthening effect on W-26Re at temperature above 1600 K, and this thoria strength increment decreased with increasing temperature. At 1600 K, for example, the yield strength of W-26Re-1ThO_2 was 67 MPa higher than that of W-26Re, indicating that 1 w/o thoria addition in W26Re resulted a 25 percent increase in strength at this temperature. At 2000 K the strength increment reduced to 25 MPa, i.e. 10 percent increase in yield strength. At temperatures above 22000 K, on the other hand, the thoria strengthening effect decreased rapidly, and both W-26Re and W-26Re-1ThO_2 had almost the same yield strength. Because the size of thoria particles was relative large in present case, some particular strengthening mechanism, instead of the formation of the Orowan dislocation loops around second-phase particles, must exist in W-26Re-1ThO_2. From the back-scattering electron images of either side surface or fracture surfaces of W-26Re-1ThO_2, it was found that thoria particles had a strong tendency of segregating along grain boundaries. These segregated particles might act as the hard pegs on the interfaces so that the grain-boundary sliding was slow down and the intergranular strength was improved. Besides, it was also found that the grain size of thoriated W-26Re was smaller than that of W26Re, especially at temperature above 2200 K. it seems that the thoria particles distributed at grain boundaries could prevent the grain boundary migration and hence, stabilize the microstructure. Since the grain growth occurred in W-26Re reduce the grain-boundary area, the stabilization of grain size occurred in thoriated W-26Re would partially compensate the pegging strengthening effect at high temperatures. This may be one of the reasons why thoria strength increment decreases rapidly at temperature above 2200 K.

Similar trend was also found in the effect of thoria on the ultimate tensile strength, as shown in Fig. 2.18. Compared the tensile strength of W-3.6Re-1ThO_2 shown in Fig. 2.8, the data obtained in present study indicated that the thoria strengthening effect in W-26Re alloy from 1600 K to 2000 K was not as significant as that in W3.6Re. This may be due to that the high rhenium solid-solution strengthening effect was so strong in this temperature range that the thoria strengthening effect had been partially covered.

It can also be seen from Figs. 2.17 and 2.18 that the difference between yield strength and ultimate tensile strength of each alloy decreased with increasing temperature. This was, certainly, caused by the decrease in strain-hardening rate as mentioned in section 2.4.1. Fig. 2.19 shows the effect of 1.0 percent thoria on the strain-hardening exponent of W-26Re. The thoria addition in W-26Re resulted in a higher strain-hardening exponent. Even though the absolute increment of n value varied with temperature, the percentage increase in n value was the same, 15 to 20 percent in the entire temperature range. Since the strain-hardening exponent is directly related to the deformation behavior inside the grains, the increase in n value shows that the thoria particles within the grain could effectively increase the interior-grain strength by hindering the dislocation motion over the entire temperature range. But because the grain boundaries are relatively weak at high temperatures, and also because the amount of thoria particles inside the grain is less than that at grain boundaries, these thoria particles dispersed within the grains have less contribution to the strength properties than those distributed at grain boundaries.

The ductility of W-26Re-1ThO_2 and W-26Re at 10^{-3}/sec strain rate, as represented by the total elongation, is shown in Fig. 2.20. As what expected, the ductility kept increasing with increasing

temperature for both alloys. And the high-temperature elongation of W-26Re-1ThO_2 was obviously lower than that of W-26Re, especially at temperature above 2200 K. This decrease in elongation can be explained by the thoria-strengthened grain boundaries. The second-phase hard particles distributed at grain boundaries made the grain-boundary sliding more difficult, and the deformation would be mainly limited within grains. Since the total strain is the sum of the strain caused by slip within the grains and the average sliding distance of grain boundaries, a reduction of average sliding distance by thoria addition would certainly lead to a lower elongation. A study of second electron imaging on the side surface of post-test specimens confirmed that W- 26Re had a much severe grain-boundary sliding than W-26Re-1ThO_2, especially at temperature above 2200 K. Still, the high-temperature elongation of thoriated W-26Re which varied from 26 pct to 39 pct in the entire temperature range was fairly good compared with those of other dispersion-strengthened W-Re alloys, such as W-Re-HfC[5, 32].

2.5.2 Effect of Strain Rate

In Fig. 2.21, the yield stresses of W-26Re-1ThO_2 and W-26Re at 2000 K are plotted as a function of strain rate in a log-log scale. With increasing strain rate, both alloys yielded at greater higher applied stress. But the yield stress of thoriated W-26Re increased with a faster rate than that of W-26Re. When the strain rate increased from 10^{-3}/sec to 10^{-2}/sec, for example, the stress increment of W-26Re-1ThO_2 was 141 MPa. While that of W-26Re was only 61 MPa, less than a half of the stress increment of thoriated W-26Re. Not only the strength property, the ductility of W-26Re-1ThO_2 was also more sensitive to the change of strain rate than W-26Re, as illustrated in Fig. 2.22. With one order increase in strain rate, the elongation of thoriated W-26Re reduced from 31 pct to 18 pct, and that of W-26Re only reduced from 36 pct to 29 pct. Obviously, the strength and ductility of thoriated W-26 is much more sensitive to the change in strain rate.

From Fig. 2.21, it can be seen that all data points of each alloy fall on a straight line. The slope of the straight line is the strainrate sensitivity which was calculated as 0.257 for W-26Re-1ThO_2, and 0.163 for W-26Re. Besides, King et al. [15] reported that at temperature above 0.5 Tm P/M W-1ThO_2 possessed a higher strain-rate sensitivity than pure tungsten. The comparison of data indicated that the tensile properties of both thoriated W or thoriated W-Re were more sensitive to the strain rate than those of either pure W or W-Re. It appeared that the addition of thoria had an obvious effect in increasing the strain-rate sensitivity in tungsten. Therefore, thoriated materials are expected to have a poor performance under impact loading, and hence should be avoided to be used in dynamic loading conditions.

Another parameter used to evaluate the effect of strain rate on the deformation behavior of a material at high temperatures is the activation volume V* as mentioned in section 2.4.3. By a linear regression treatment, the activation volumes of W-26Re-1ThO_2 and W-26Re at 2000 K were found to be 0.833 X 10^{-21} cm^3 and 1.312 X 10^{-21} cm^3 or 43 b^3 and 64 b^3 respectively. Where b is the Burgers vector of tungsten. According to Krausz et al. classification of V* magnitudes[30], both Peierls-Nabarro mechanism and cross-slip mechanism could be the rate controlling mechanisms in the plastic deformation process of these two alloys at 2000 K.

2.5.3 Fracture Behaviors

The fracture surfaces of all tested specimens were examined with a scanning electron microscope. Figs. 2.23 and 2.24 are the fractographs of specimens tested at 1800 K and 2400 K, respectively. The fracture mode was intergranular for both W-26Re-1ThO_2 and W-26 in the entire temperature range. As mentioned in section 2.4.4, rhenium addition in tungsten would reduce the grain-boundary strength so that the intergranular fracture is the dominant fracture mode for high rhenium W-Re alloys. Since the intergranular fracture implies that the grain boundaries are the weakest region of the material, the most effective way to strengthen the material would be the strengthening

of grain boundaries. It is the pegging effect of segregated thoria particles that give the thoriated W-Re greater high-temperature strength. Besides, the effect of strain rate on the fracture behavior of both alloys at 2000 K was also examined, and it appeared that the increase in strain rate did not affect the fracture mode. Both alloys deformed at various strain rate showed a transgranular fracture mode at 2000 K. This may be due to the fact that the range of strain rate applied in present study is not wide enough to produce the transition of fracture mode.

Also, It was reported [15] that voids were formed at grainboundaries in pure tungsten and W-1ThO_2 during deformation at temperature above 0.5 Tm, and these voids leaded to the intergranular fracture. Voids were observed for both alloys tested above 2000 K in present study. And these voids were formed in the whole uniform gage section but to a less extent than those observed in the near-fracturetip region. The majority of voids were presented at the parallel boundaries in W-26Re-1ThO_2, but were mostly presented in the grain boundary triple points for W-26Re. This is because that W-Re had a more severe grain-boundary sliding due to the less friction between interfaces of grains. The requirement of deformation compatibility makes the voids easier to create at triple points of grain boundaries in W-26Re. Furthermore, it can be seen that the addition of thoria in W-26Re not only reduced the size of voids but also stabilized the microstructure. It was observed that the grain size of W-26Re was almost the same as that of W-26Re-1ThO_2 up to 2000 K, and was 15-20 percent larger than that of W-26Re-1ThO_2 above 2200 K, indicating that the addition of thoria in W-Re could resist the grain growth at high temperatures. It is well known that the segregated second-phase particles at grain boundaries will lower the grain-boundary energy and hence, prevent the migration of grain boundaries. This stabilization of microstructure is beneficial at low temperatures, but is unwanted at high temperatures because grain boundaries become the relative weak region under thermal activation. Therefore, the stabilization of grain size occurred in thoriated alloy was thought to be partially responsible for the rapid decrease in thoria strengthening effect on W-26Re at temperature above 2200 K.

2.5.4 Conclusions

(1) Thoria has a modest strengthening effect in W-26Re up to 2000 K. And the increase in strength mainly attributes to the pegging effect of segregated thoria particle at grain boundaries.

(2) 1 w/o thoria addition in W-26Re results in about 15 to 20 increase in the strain hardening exponent over the entire temperature range from 1600 K to 2600 K.

(3) The high-temperature ductility of W-26Re is reduced by thoria addition because the grain-boundary sliding is slow down by the intergranularly distributed second-phase particles.

(4) Thoria addition makes the strength and ductility of W-26Re more sensitive to strain rate. At 2000 K, W-26Re-1ThO_2 has a strainrate sensitivity of 0.247 and an activation volume of 8.83×10^{-22} cm^3 (43 b^3). For W-26Re, the correspond values are 0.163 and 1.312×10^{-21} cm^3 (64 b^3), respectively.

(5) The mode of fracture is intergranular for both W-26Re-1ThO_2 and W-26Re. And the increase in strain rate does not change the fracture mode.

(6) Thoria addition in W-Re has an effect in stabilizing the microstructure at high temperatures.

2.6 HfC STRENGTHENING IN W-3.6Re ABOVE 0.5 T_m

2.6.1 HfC Strength Increment

Figure 2.25 shows the 0.2% offset yield strengths of arc-melted W-3.6Re-0.26HfC and pure W, as well as those of W-3.6Re tested under the similar conditions [2], as a function of test temperature. Each data point of W-3.6Re-0.26HfC showed in this figure indicated the average of the results obtained from at least two specimens tested under the identical condition. It is clearly seen that W-3.6Re-0.26HfC exhibited much greater high-temperature strength than that of pure W up to 2450 K. At temperatures higher than 2450 K, the tensile strength of W-3.6Re-0.26HfC decreased rapidly and gradually became similar to that of pure W. Previous studies on the effect of grain size on the high-temperature mechanical properties of tungsten had shown that a difference about 40 percent in grain size, such as the present case, had a very small influence on the strength of tungsten above 2000 K. The excellent high-temperature tensile strength of W-3.6Re-0.26HfC, therefore, must come from the solid-solution strengthening of rhenium and the dispersed-particle strengthening of hafnium carbide.

In order to approximately evaluate the strengthening effect of HfC particles in tungsten matrix, we might use the cubic SPLINE interpolating method to obtain the strength-temperature curves of W-3.6Re and W-3.6Re-0.26HfC, and then subtract the tensile strength of W-3.6Re from that of W-3.6Re-0.26HfC. Based on this approach, the strength increment introduced by HfC, i.e., the individual contribution of dispersed HfC particles to the high-temperature yield strength of a W-3.6Re-0.26HfC alloy, as a function of testing temperature is given in Figure 2.26. The dispersed HfC particles exhibited an exceptional strengthening effect at 1950 K, and a HfC strength increment as high as 248 MPa was obtained. With increasing temperature, the strengthening effect of HfC particles decreased monotonically as expected, but was fairly good up to 2450 K at which there still existed a HfC strength increment of 125 MPa, more than double the yield strength of 45 MPa observed by Klopp in an arc-melted W-3.6Re at this temperature [2]. This implied that the HfC particles were thermally stable up to 2450 K so that these dispersed particles could still hinder the dislocation motion effectively at this temperature. A HfC strength increment of 94 MPa was observed at 2700 K. At higher temperatures, the HfC strength increment rapidly reduced to zero and no HfC strengthening effect was found at 2900 K.

A similar trend was also observed in the tensile strengths of a W-3.6Re-0.26HfC and pure W, as shown in Figure 2.27. At 1950 K, the tensile strength of a W-3.6Re-0.26HfC was about 400 MPa higher than that of a W-3.6Re. The increasing temperature resulted in a monotonic decrease in tensile strength, but the tensile strength of W-3.6Re-0.26HfC was still 132 MPa higher than that of W-3.6Re at 2450 K.

The strain-hardening exponents of W-3.6Re-0.26HfC and pure W from 1700 K to 2980 K, together with the **n** values reported by Taylor [1] in a W-3Re alloy tested at the same strain rate, are shown in Figure 2.28. It was of interest to note that the strain-hardening exponents of pure W observed in the present study were just slightly smaller than those of W-3Re, confirming that the addition of rhenium had a rather small contribution to the strength properties of tungsten at high temperatures. It could be seen from Figure 2.28 that the strain-hardening exponents of W-3.6Re-0.26HfC were obviously greater than those of either W-3Re or pure W at the temperatures up to 2450 K, but did not show significant difference from those of W-3Re and pure W above 2450 K.

The activation energies of plastic deformation for pure W and W-3.6Re-0.26HfC, together with those of other important tungsten base alloys, are given in Table 2.1. As expected, W-3.6Re-0.26HfC possessed the highest activation energy of plastic deformation and the largest strength coefficient among various tungsten base alloys. Comparing the Q value of W-3.6Re-0.26HfC with those of pure W and W-3.6Re, it was found that a 0.26 percent addition of HfC in tungsten resulted in about 28 percent increase in activation energy of plastic deformation, while a 3.6

percent addition of rhenium in tungsten only increased the Q value by about 9 percent.

Figure 2.29 shows the tensile elongation of W-3.6Re-0.26HfC at high temperatures. Similar to all of the arc-melted metals and alloys discussed in the previous sections, the ductility of W-3.6Re-0.26HfC increased with increasing temperature. But this high-strength alloys showed a relatively low ductility at high temperatures.

2.6.2 Discussion

Because the thermal activation significantly reduces the interaction between solute atoms and dislocations at temperatures above 0.5 T_m, the strengthening effect obtained from the addition of a 3.6% rhenium was very small. This could be easily shown by comparing the tensile strength of W-3.6Re with that of pure W. The addition of a 0.26% HfC, therefore, had the dominant contribution to the superior strength of W-3.6Re-0.26HfC at high temperatures. Figure 2.30 shows the microstructure of W-3.6Re-0.26HfC deformed at 1950 K and 2450 K. There existed a strong interaction between the second-phase particles and dislocations. The dislocations were firmly pinned by HfC particles, resulting in a significant decrease in dislocation mobility. From Figure 2.30, it is easy to see that most dislocation lines attached to the HfC particles. This phenomenon, so called "dislocation smearing", was first noted by Nardone and Tien [33] and then confirmed by other researchers [34-36] in various dispersion-strengthened materials deformed at high temperatures. Srolovitz and coworkers [37] proposed that the interface between an incoherent particle and the matrix could be modeled as a slipping interface which does not support tangential forces. The dislocation glides up to the particle and spreads out its core over the interface in order to reduce its energy. Since this mechanism depends on diffusive processes, it is expected to be operated only at high temperatures. Recently, Arzt et al [38,39] have developed a local climb theory which depends on the dislocation being attracted to the particle/matrix interface. They have shown that if the line tension of a dislocation at the interface is 6 percent lower than that in the matrix, the stress required for its detachment from the particle exceeds the barrier to climb so that dislocation detachment becomes the strength-controlling mechanism.

Besides, the inhomogeneity of deformation in the particle adjacent region could also have some contribution to the the **n** value of W-3.6Re-0.26HfC. We define, following Ashby [40], a crystalline material containing the second-phase particles that do not deform together with the matrix as the plastically inhomogeneity. Although the plastic deformation in W-Re alloy might be quite large, HfC particles did not deform or deformed only elastically, leading to an inhomogeneous deformation in W-Re alloy. There did not occur any slip (i.e., the plastic deformation) in the HfC particles or in the adjacent matrix region. Far away from the particles, however, the slip could be quite large. Thus, the second-phase particles introduced microscopically the gradients of deformation in the W-Re matrix, although macroscopically the deformation appeared uniform. The smaller the HfC particles, the smaller the spacing between the particles, and the larger the strain gradients would be. The strain gradients, in turn, had partial contribution to the extraordinarily fast work hardening rate in W-3.6Re-0.26HfC.

It is well known that with increasing temperature, more energy is supplied to the diffusion process occurred around the dispersed particles, resulting in a rapidly coarsening of second-phase particles above a critical temperature. Particle coarsening implies a reduction of total particle number available in the matrix, and hence, an increase in the mean slip distance of dislocation and a decrease in the strain-hardening rate. Since both W-3.6Re-0.26HfC and pure W had a similar strain-hardening exponent at temperatures above 2450 K, this similarity suggested that the temperature of 2450 K could be concerned as the characteristic temperature at which rapid coarsening of HfC particles occurred. This was confirmed by the growth behavior of HfC particles determined by the transmission electron micrographs of W-3.6Re-0.26HfC tested at various temperatures. Figure 2.31 shows the HfC particle radius as a function of testing

temperature. The size of HfC particles did not change much with increasing temperature up to 2450 K, and then increased rapidly at higher temperatures. This was concerned as the most important reason why the dispersion strengthening effect of HfC decreased significantly above 2450 K, as shown previously in Figures 2.25-2.28.

For the ideal case of spherical particles coarsening by the diffusion-controlled transfer of solute in the matrix, the most acceptable equation for the rate of particle coarsening was derived by Lifshitz and Slyozov [41] with the following form

$$r^3 - r_o^3 = K_c t \tag{2.6}$$

where r is the average particle radius at time t, r_o is the average particle radius at the onset of coarsening, and K_c is a rate constant. It should be pointed out that the magnitude of r_o has only a minor effect on the final particle size because r^3 is generally much larger than r_o^3. Theoretically, the rate constant K_c can be calculated by

$$K_c = \frac{8D\gamma C_e V_m^2}{9\,RT} \tag{2.7}$$

where g is the interfacial free energy of the particle-matrix interface, C_e is the concentration of solute in the matrix in equilibrium with a particle of infinite size, D is the diffusion coefficient of solute in the matrix, V_m is the molar volume of dispersed particles, R is the gas constant, and T is the absolute temperature. K_c value is usually considered as a measure of the thermodynamic stability of second-phase particles. The smaller the rate constant K_c, the more stable the particles.

Since so far the g value of HfC particle in W-Re matrix is unknown, it was rather difficult to directly use equation (2.7) calculating the rate constant K_c of HfC particles in W-Re. Instead, we might obtain the value of K_c experimetally by examining the particle growth behavior shown in Figure 2.31. Based on the eqn.(2.7), K_c could be written in the following form

$$K_c = \frac{\alpha}{T} \exp(-\frac{E}{RT}) \tag{2.8}$$

where a is a material constant, E is a measure of the temperature dependency of rate-limiting diffusion reaction, and R and T have their usual meanings. The E value can be experimentally determined by a plot of K_cT against inverse absolute temperature. This plot, shown in Figure 2.32, can be represented by the relation:

$$K_cT = 1.08 \text{ X } 10^{-10} \exp(-\frac{61{,}800}{RT}) \tag{2.9}$$

The activation energy of hafnium in tungsten is 47,200 cal/mole [42], and that of carbon in tungsten is 53,500 cal/mole [43]. The diffusivities of both carbon and hafnium in tungsten matrix from 1900 K to 3000 K were calculated, and the results are shown in Figure 2.33. Even though the diffusivity of carbon in tungsten is lower than that of hafnium in tungsten, we could not conclude that carbon is the controlling element determining the HfC particle coarsening rate in tungsten matrix. This is because both carbon and hafnium atoms have a very fast diffusion rate in tungsten at high temperatures. For example, at 2450 K, the one-minute diffusion distance of either carbon or hafnium in tungsten is about two orders higher than the average interparticle spacing. The diffusion process could not be considered as the controlling stage in the particle growth.

Instead, the small growth rate of HfC particles observed in the present study was most likely due to the relatively low decomposition rate of this highest-melting-point carbide.

Since the finely distributed particle represents an effective barrier to dislocation motion, various theories have been developed to explain the enhanced yield strength of a metal containing a dispersed second phase of small hard particles. These theories can be separated into two types: the indirect effect of the dispersed second phase, i.e., the long range interactions between the dispersed particles and dislocations; and the short range interaction, i.e., dislocation circumnavigation around the particle in its slip plane.

The first mechanism is related to the difference in average atomic volume of the dispersoids and matrix. This difference results in many randomly distributed internal stress fields which would distort the matrix and hence, hinder the movement of dislocation motion. This strengthening effect is essentially depends upon the particle volume fraction and the difference in atomic volume. One of the most acceptable theories in this field was suggested by Mott and Nabarro [44] based on the analysis of the internal stresses resulting from the difference in average atomic volume of the matrix and of the dispersoids.

The short range interaction mechanism assumes the direct interactions between moving dislocations and unshearable dispersoids. This interaction is directly related to the particle size and distribution, and hence, is temperature dependent. As seen in Figure 2.30, dislocation lines were firmly pinned up by HfC particles which could be considered as the pinning up points of Frank-Reed sources [45]. The stress needed for dislocation motion is therefore the stress required to operate the Frank-Reed source which is proportional to the Burgers vector and shear modulus of the matrix, and invedrsely proportional to the interparticle spacing. If we consider both long-range interaction and short-range interaction of particles with dislocations, the shear stress of a dispersion alloy can be expressed as the following

$$\tau_s = \tau_{ms} + \tau_{ls} + \frac{bG_m}{L} \qquad (2.10)$$

where τ_s is the shear strength of particle-strengthened material, τ_{ms} is matrix shear strength, τ_{ls} is the strength increment caused by the long range interaction, G_m is the matrix shear modulus, **b** is the Burgers vector of dislocation in the matrix, and L is the average interparticle spacing. Using the Tresca yielding criterion and the Mott-Nabarro theory on particle dilatation misfit, and noticing that τ_s, τ_{ms}, G_m, and L are all temperature dependent, we might re-write relation (2.10) in the following form

$$\sigma_y(T) = \sigma_{my}(T) + \gamma_s G_m(T) + \frac{2bG_m(T)}{L(T)} \qquad (2.11)$$

where $\sigma_y(T)$ and $\sigma_{my}(T)$ are the yield stresses of particle-strengthened material and matrix, respectively, and g_s is the misfit strain caused by the second-phase particles. In the present case, the molar volumes for HfC and W-Re matrix are 15.618 cm^3/mole and 9.521 cm^3/mole, respectively. By using the Mott and Nabarro theory, the misfit strain introduced by 0.26wt.% (or 0.43 vol.%) HfC was found to be about $4.53X10^{-3}$. And the strength increment due to the long range interaction of HfC with dislocations in the temperature region of 1950 K to 2980 K was calculated as less than 20 MPa, and could be negligible. Therefore, the third term on the right hand of relation (2.11), i.e., the short range interaction, has the dominant contribution to the exceptionally high strength of W-Re-HfC alloy at high temperatures. Since this term is very

sensitive to the interparticle spacing L(T), the description of the particle distribution in a matrix becomes very critical to the evaluation of dispersion strengthening model. One of the reasonable approaches, suggested by Westmacott [46], assumed that the particle distribution was a uniform random distribution in the volume so that there was an average number of N_p particles per unit volume. According to the statistics principles, for the three dimensional case, the mean nearest neighbor distance is given by the relation

$$L = 0.5540\ (N_p)^{-1/3} \tag{2.12}$$

And for the two dimensional case, the mean nearest neighbor distance is

$$L = \frac{0.5}{\sqrt{N_p}} \tag{2.13}$$

Now if the particles has an average radius **r**, a plane which could be concerned as the slip plane of dislocation through the material would intersect particle up to $\pm$ **r** from the plane. In such case the planer density of effective particles is $2rN_p$ points per unit area. Therefore, the interparticle spacing could be calculated by

$$L = \frac{0.5}{\sqrt{2rN_p}} \tag{2.14}$$

Since in a unit volume the second-phase particle volume fraction is given by

$$F_v = \frac{(4/3)\pi r^3 N_p}{1} \tag{2.15}$$

Relation (2.15) might be re-written as

$$L = 0.5r\sqrt{\frac{2\pi}{3F_v}} \tag{2.16}$$

Substitute relation (2.16) into relation (2.11) and note that **r** is a function of temperature, we finally obtain

$$\sigma_y(T) = \sigma_{my}(T) + \gamma_s G_m(T) + \frac{4b\sqrt{3F_v}\ G_m(T)}{\sqrt{2\pi}\ r(T)} \tag{2.17}$$

It is of interest to note that relation (2.17) predicted that the yield strength a dispersion-strengthened alloy is proportional to the square root of particle volume fraction. This is consistent with Klopp's observation on the strength properties of W-4Re-HfC as a function of HfC content at 2200 K [31]. According to the TEM observation of post-test specimens, the volume fraction of HfC particles was approximately a constant at different temperatures. Therefore, the effect of testing temperature on the strength of W-Re-HfC was mainly attributed to the effect of temperature on the particle size. The calculated yield strength of a W-3.6Re-0.26HfC as a function of temperature, obtained by using relation (2.17), together with the values experimentally determined in the present study, are shown in Figure 2.34. The theoretical values obtained by using the

statistical distribution theory of particle were in good agreement with the true yield strength of a W-3.6Re-0.26HfC above 1950 K. The root-mean-square derivation of the statistical model was determined as 19.8%. The present work, hence, suggested that the statistics model could be the most acceptable model for the strengthening of HfC particles in W-Re matrix. And we also supported the contention that the yield strength of a dispersed particle-strengthened material varied as $F_V^{1/2}$ at high temperatures.

According to its strength properties, W-Re-HfC appeared as the strongest metallic material to our present knowledge at temperatures above 1950 K. According to its activation energy of plastic deformation, on the other hand, W-Re-HfC also showed the highest temperature sensitivity among all materials examined in the present study. This is because the strength of dispersed alloy depends primarily upon the pinning force of second-phase particles on dislocations. This kind of force is certainly a strong function of temperature. The thermal activation and diffusion process results in a rapid growth of dispersed particle and also severely reduces the interaction between the particles and dislocations. With increasing temperature the hindering of these particles on the dislocation movement is significantly decreased and the dislocation mobility is expected to be increased rapidly, resulting in a relatively great temperature sensitivity.

2.6.3 Conclusions

(1) W-3.6Re-0.26HfC appear as as the strongest metallic material to our present knowledge at temperatures above 1950 K. HfC particle strengthening is effective in a W-Re matrix up to 2450 K, and the HfC strengthening is mainly due to the pinning up of HfC particles to the dislocations.

(2) A HfC-introduced yield strength increment of 248 MPa is observed at 1950 K, and 125 MPa at 2450 K.

(3) The characteristic temperature at which rapid HfC particle coarsening occurs is around 2450 K in the short-term tensile tests.

(4) The yield strength of HfC-strengthened alloy at temperatures above $0.5T_m$ is proportional to the square root of particle volume fraction. The yield strength of a W-3.6Re-0.26HfC calculated based on the particle statistical distribution is in good agreement with the experimental values.

(5) It is also found that the addition of 0.26 percent HfC in tungsten results in about 28 percent increase in activation energy of plastic deformation. Besides, the high-temperature ductility of W-Re is reduced by the HfC dispersions.

References

1. J. L. Taylor, J. Less-Common Metals, 7(1964)278.

2. W.D. Klopp, W.R. Witzke, and P.L. Raffo. NASA Tech. Note D-3483, Cleveland, Ohio, 1966.

3. P.L. Raffo, J. Less-Common Metals, 17(1969)133.

4. J.R. Stephens and W.R. Witzke, J. Less-Common Metals, 23(1971)325.

5. W.D. Klopp and W.R. Witzke, NASA Tech. Note D-5348, Cleveland, Ohio, 1969.

6. W.D. Klopp and W.R. Witzke, J. Less-Common Metals, 24(1971)427.

7. W.R. Witzke, Metall. Trans., 5(1974)499.

8. M.L.Ramalingam and D.L. Jacobson, J. Less-Common Metals, 123(1986)153.

9. J. Fembock, R. Stickler, and A. Vinckier, Proc. 11th International Plansee Seminar, Austria, 1(1985)361.

10. A.S. Drachinskiy, Y.N. Podrezov, and V.I. Trefilov, Phys. Met. Metall., 55(1983)140.

11. V.I. Eremin, V.A. Moskalenko, and V.I. Startsev, Scripta Metall., 17(1983)751.

12. A.S. Drachinskiy, A.V. Kraynikov, and V.I. Trefilov, Phys. Met. Metall., 58(1984)102.

13. G.A. Geach and J.R. Hughes, Plansee Proceedings, Pergamon Press, London, 1955, p. 245.

14. W.D. Klopp, NASA Tech. Note D-4955, Cleveland, Ohio, 1968.

15. G.W. King and H.G. Sell, Trans. AIME, 233(1965)1104.

16. G. W. King, Trans. AIME, 245(1969)83.

17. G.E. Forsythe, M.A. Malcolm, and C.B. Moler, Computer Methods for Mathematical Computations, Prentice-Hall, Inc., New Jersey, 1977, p. 70.

18. E. Pink and R. J. Arsenault, Progress in Materials Science, 24(1979)1.

19. P.L. Raffo, NASA Tech. Note D-4567, Cleveland, Ohio, 1968.

20. R.I Jaffee, C.T. Sims, and J.J. Harwood, Plansee Proceedings, Pergamon Press, 1958, p. 380.

21. C.T. Sims and R.I. Jaffee, Trans. ASM, 52(1960) 927.

22. D.A. Robins, J. Less-Common Metals, 1(1959)396.

23. D.A. Robins, Trans. ASM, 52(1960)943.

24. E.N. Aua and C.N.J. Wagner, Trans. ASM, 59(1966)367.

25. D.L. Davidson and F.R. Brotzen, Acta Metall., 18(1970)463.

26. G. E. Dieter, Mechanical Metallurgy, 3rd ed. McGraw-Hill Book Co., New York, 1986, pp.205 & 303.

27. R.P. Elliot, Constitution of Binary Alloys, lst Suppl., McGrawHill, New York, 1965, p. 528.

28. I.G. Booth, Annual Topical Report on Contract No. Nonr-3589(00), Battelle Memorial Inst., Columbus, Ohio, 1963.

29. M. A. Meyers and K. K. Chawla, Mechanical Metallurgy, PrenticeHall, Inc., New Jersey, 1984, p.570

30. A. S. Krausz and H. Eyring, Deformation Kinetics, John Wiley & Sons, New York, 1975, p. 120.

31. W.D. Klopp, P.L. Raffo and W.R. Witzke, J. Metals, 6(1971)27.

32. A. Luo, D.L. Jacobson, and K.S. Shin, Scripta Metall., 23(1989)397.

33. V. C. Nardone and J. K. Tien, Scripta Metall., 17(1983)467.

34. D. J. Srolovitz, R. Petkovic-Luton, and M. J. Luton, Scripta Metall., 18(1984)1063.

35. J. H. Schroder and E. Arzt, Scripta Metall., 19(1985)1129.

36. R. S. Herrick, J. R. Weertman, R. Petkovic-Luton, and M. J. Luton, Scripta Metall., 22(1988)1879.

37. D. J. Srolovitz, R. Petkovic-Luton, and M. J. Luton, Phil. Mag. A, 48(1983)795.

38. E. Arzt and D. S. Wilkinson, Acta Metall., 34(1986)1893.

39. E. Arzt and J. Rosler, Acta Metall., 36(1988)1053.

40. M. F. Ashby, Phil. Mag., 21(1970)399.

41. I. M. Lifshitz, and V. V. Slyozov, J. Phys. Chem. Solids, 19(1961)35.

42. B. A. Dainyak and V. I. Kostikov, Diffusion and Defect Data, 16(1978)66.

43. R. C. Weast ed. Handbook of Chemistry and Physics, 64th ed, CRC Press, Inc., Florida, 1983, F51.

44. N. F. Mott and F. R. Nabarro, Proc. Phys. Soc., London, 52(1940)86.

45. F. C. Frank and W. T. Reed, Phys. Rev., 79(1950)722.

46. K. H. Westmacott, C. W. Fountan, and R. J. Stirton, Acta Metall., 14(1966)1628.

TABLE 2.1 Activation Energies of Plastic Deformation for Pure Tungsten and Tungsten Base Alloys

Composition	Q(cal/mole)	C_1(MPa)
A/M W	11,020	2.600
W-3.6Re [2]	12,040	5.120
W-26Re	13,040	5.120
W-1ThO_2	12,550	4.773
W-3.6Re-1ThO_2	12,860	5.654
W-11Re-1ThO_2	13,270	5.610
W-26Re-1ThO_2	13,790	5.330
W-3.6Re-0.26HfC	15,180	6.895

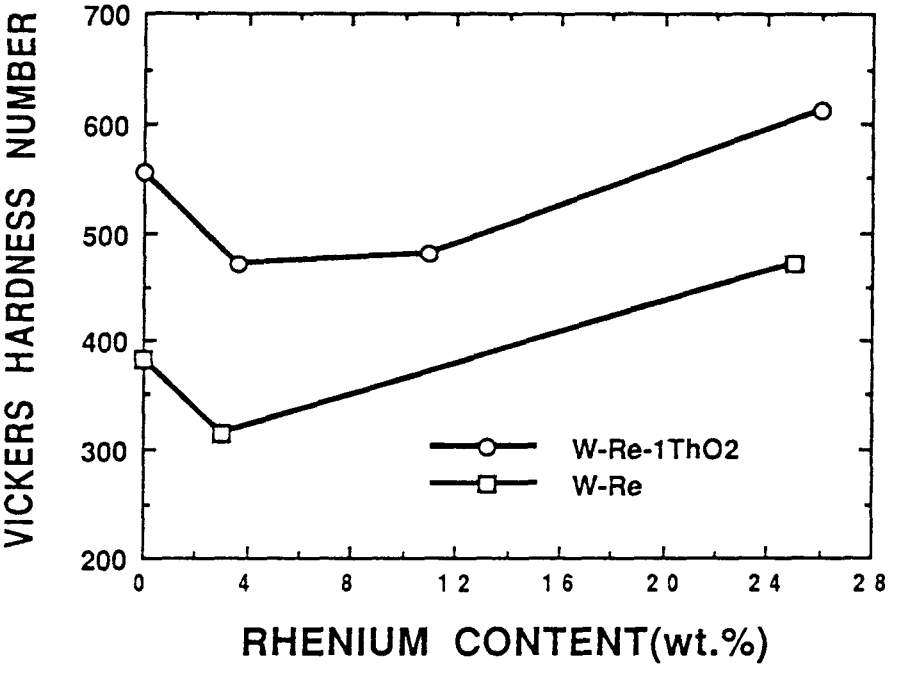

Fig. 2.1 Room-temperature hardness of W-Re-1ThO_2 alloys

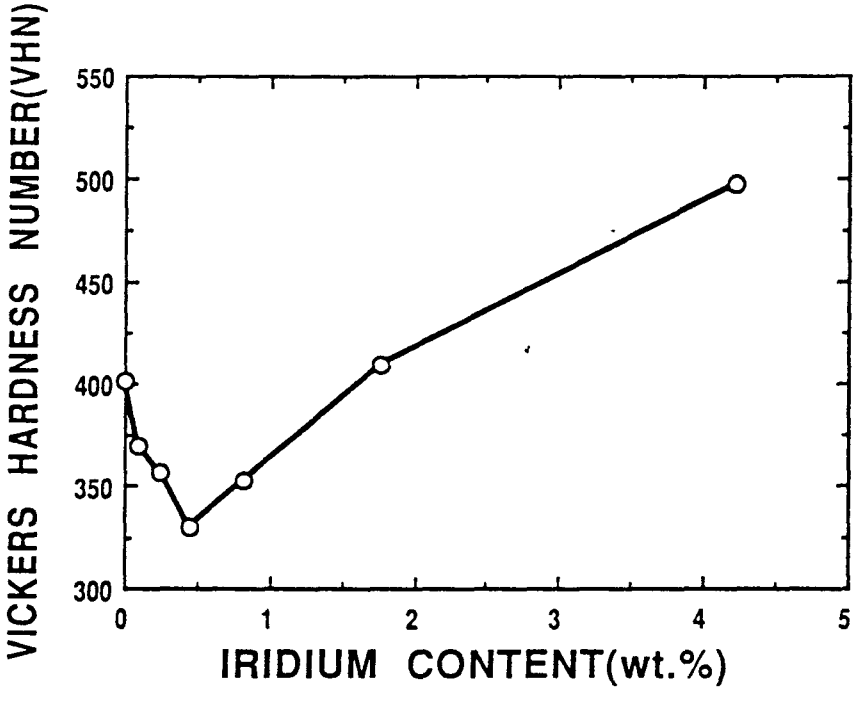

Fig. 2.2 Room-temperature hardness of W-Ir alloys

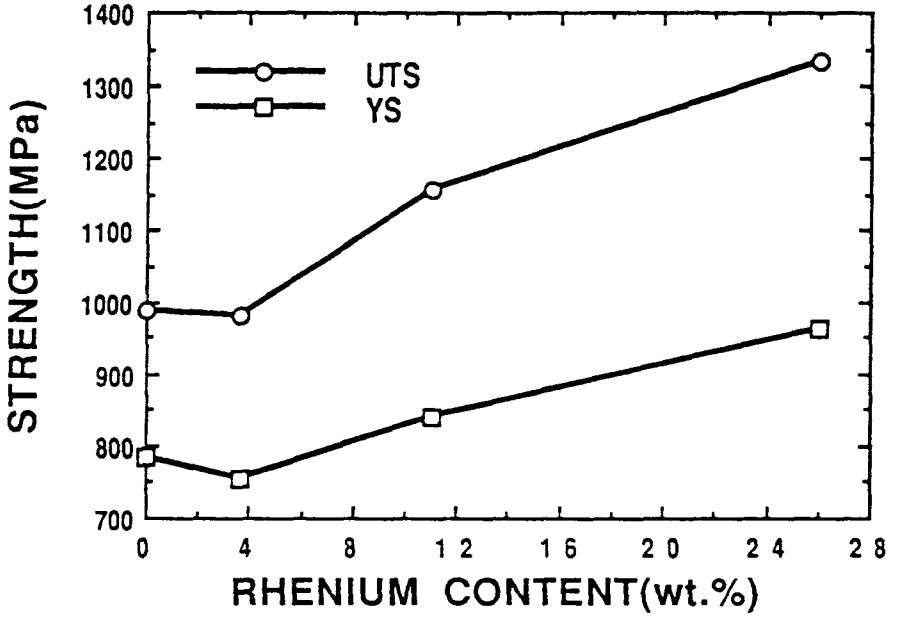

Fig. 2.3 Strength of W-Re-1ThO_2 alloys at room temperature.

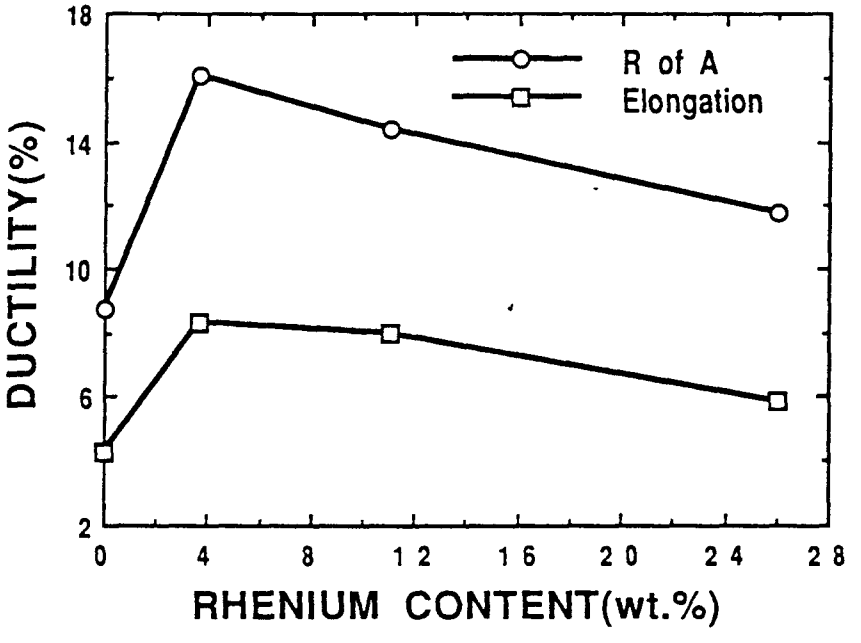

Fig. 2.4 Ductility of W-Re-1ThO_2 alloys at room temperature

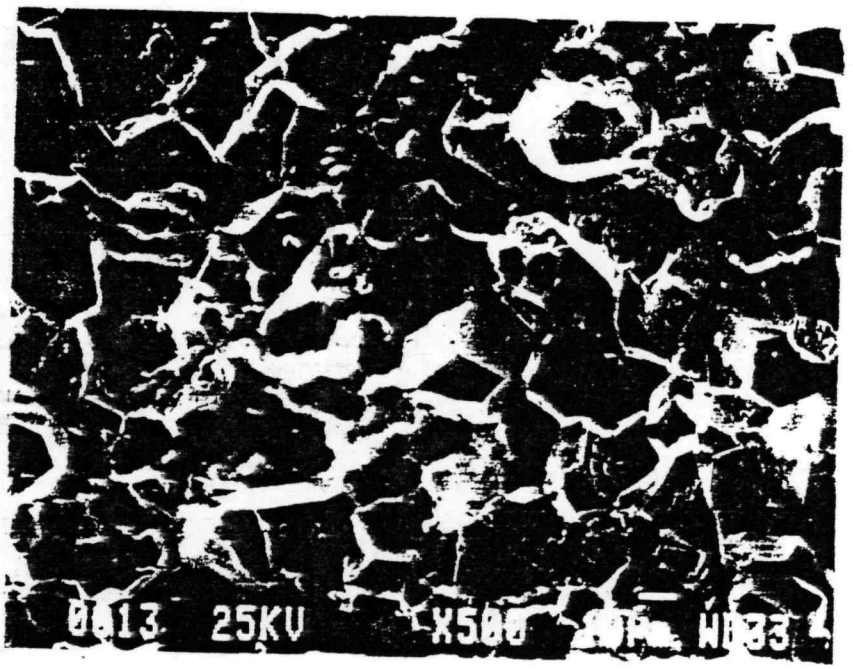

(a) W-1ThO_2

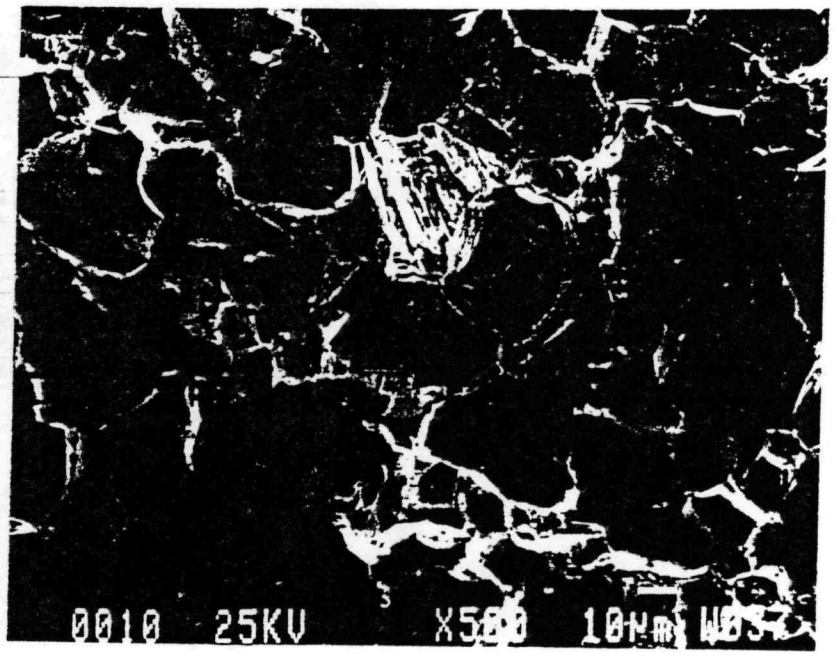

(b) W-3.6Re-1ThO_2

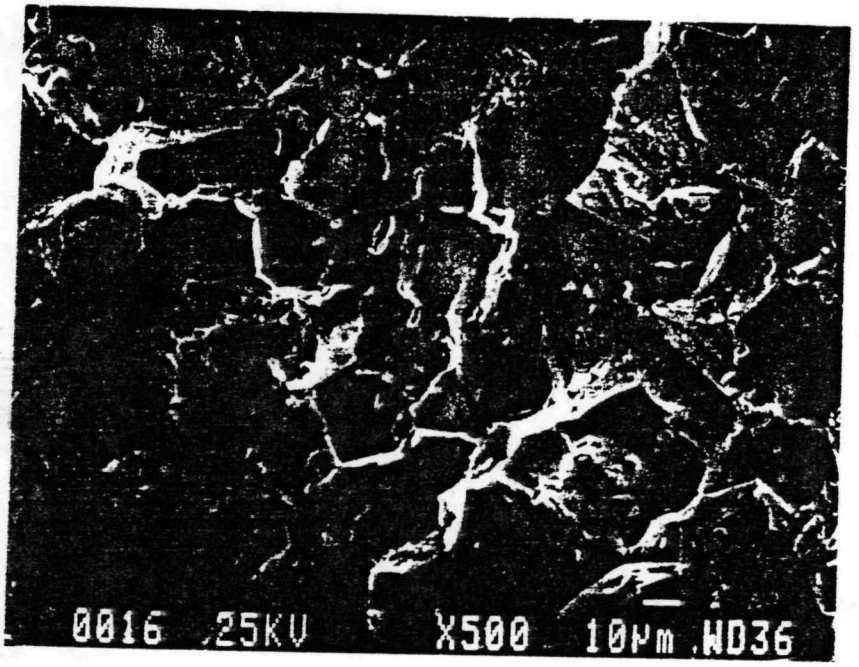

(c) W-11Re-1ThO_2

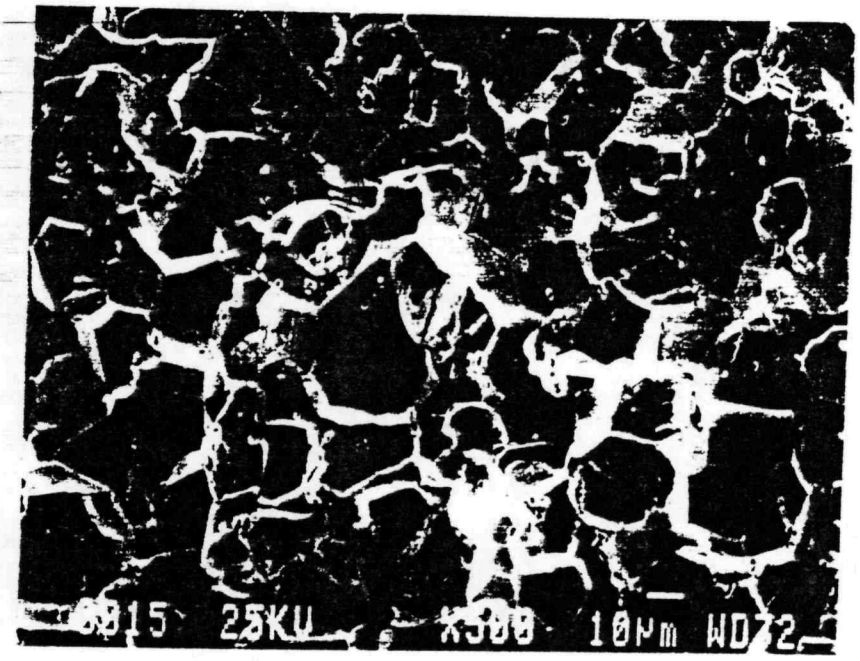

(d) W-26Re-1ThO_2

Fig. 2.5 Fractographs of W-Re-ThO_2 alloys at room temperature.

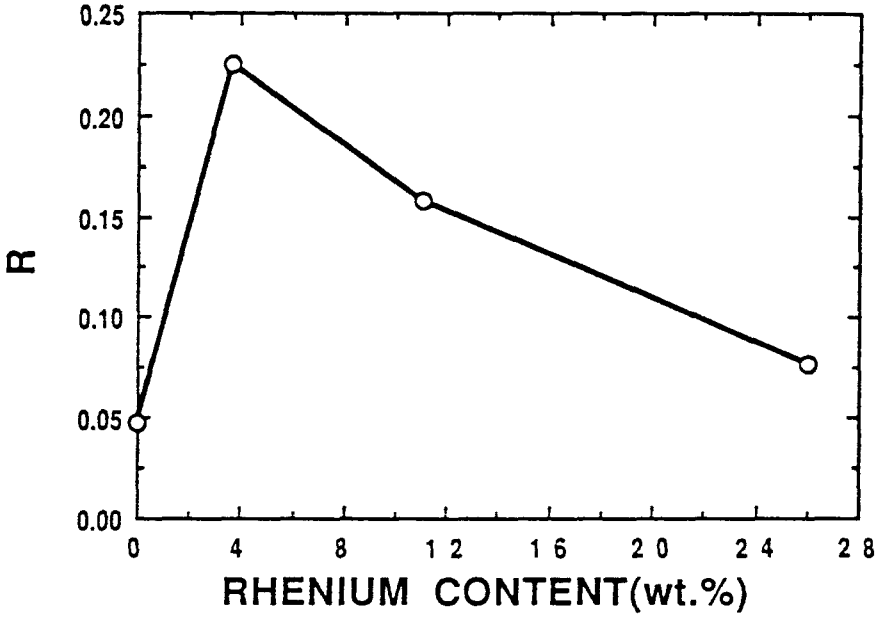

Fig. 2.6 Fraction of transgranular fracture of W-Re-ThO_2 as a function of rhenium content.

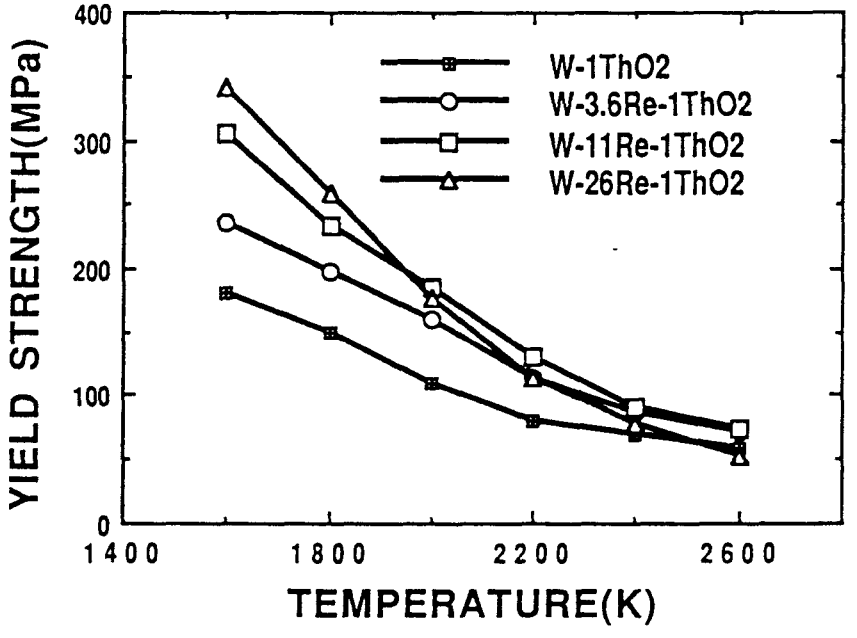

Fig. 2.7 Effect of rhenium on the 0.2% yield strength of W-Re-1ThO_2 alloy from 1600 K to 2600 K.

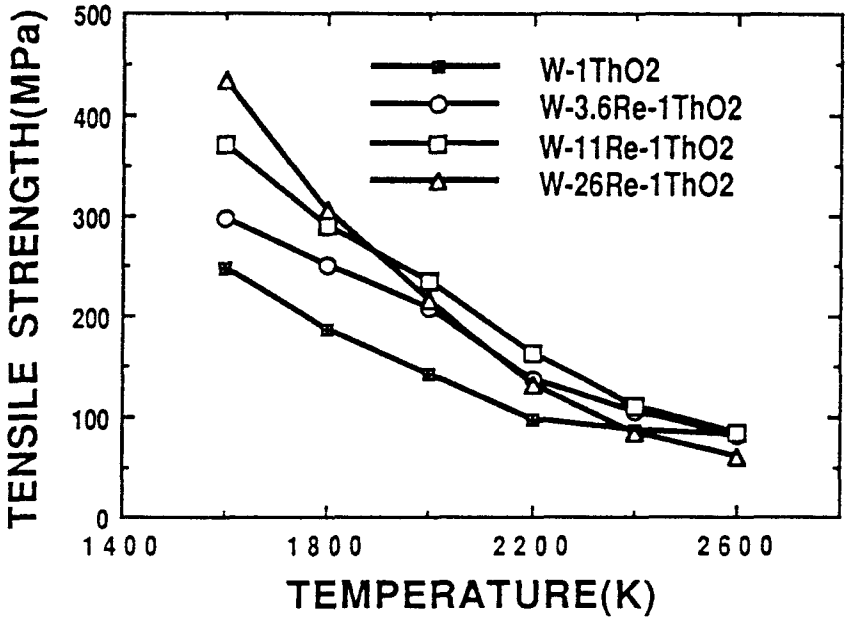

Fig. 2.8 Effect of rhenium on the ultimate tensile strength of W-RelThO$_2$ from 1600 K to 2600 K.

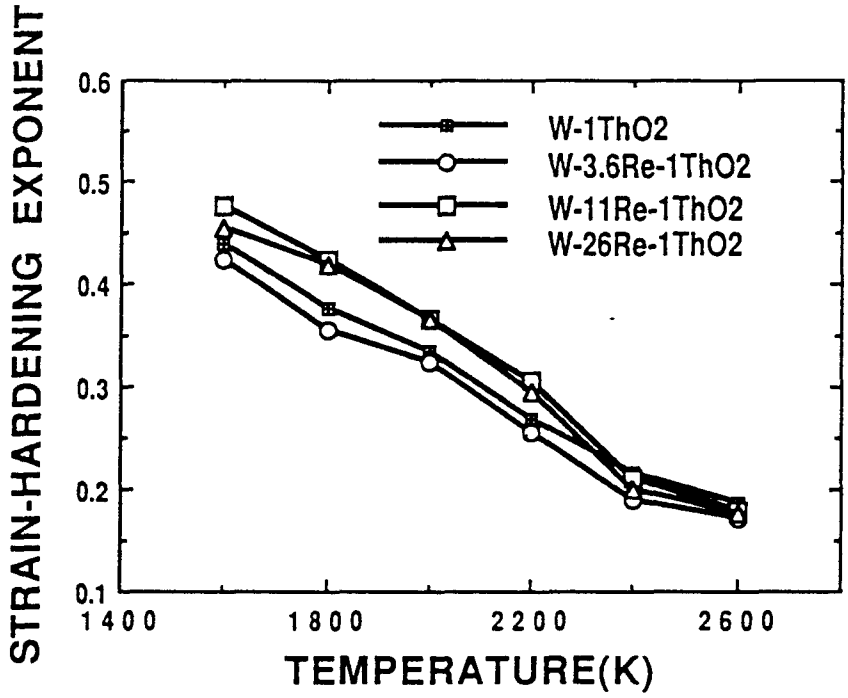

Fig. 2.9 Effect of rhenium on the strain-hardening exponent of W-RelThO$_2$ from 1600 K to 2600 K.

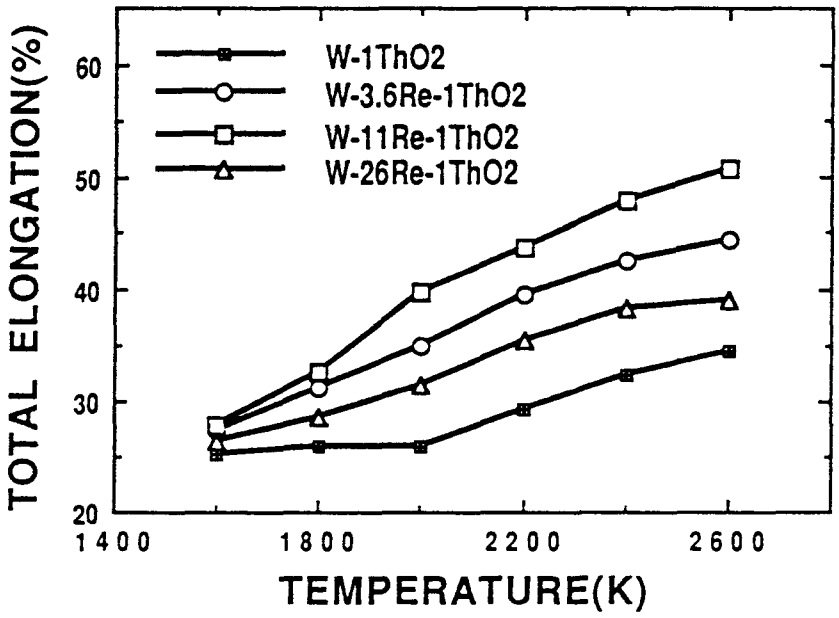

Fig. 2.10 Effect of rhenium on the total tensile elongation of W-Re-1ThO_2 from 1600 K to 2600 K.

(a) W-1ThO_2

(b) W-3.6Re-1ThO_2

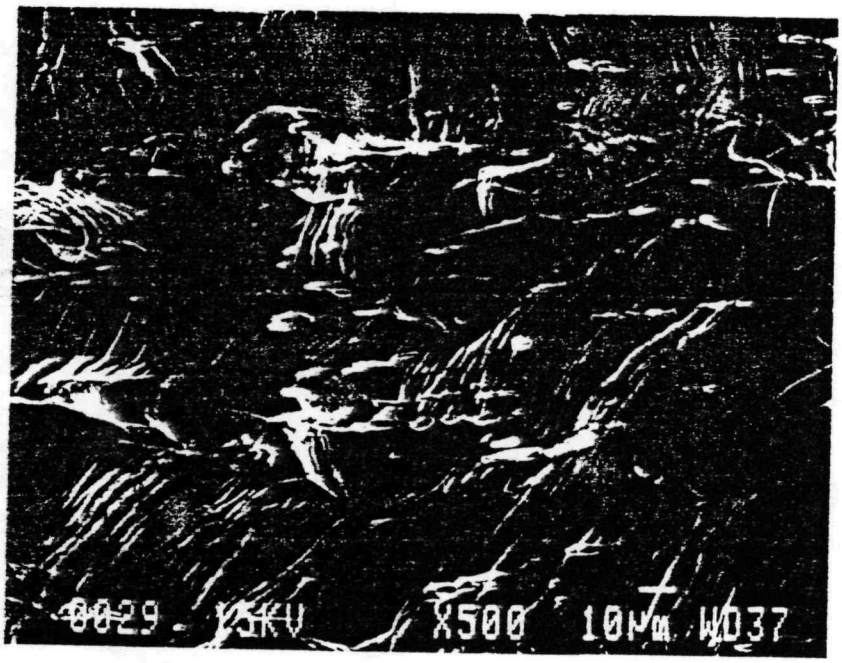

(c) W-1lRe-1ThO_2

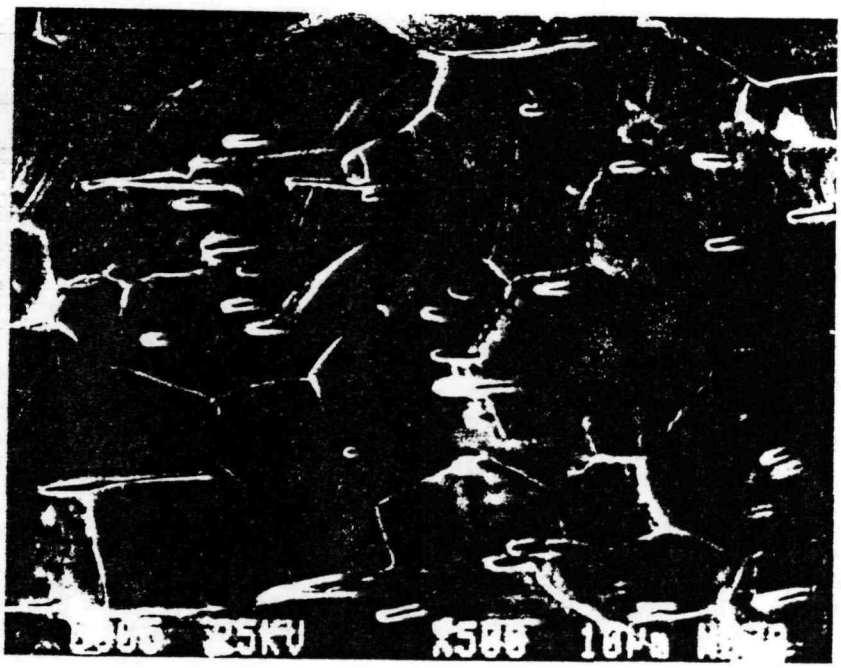

(d) W-26Re-1ThO_2

Fig. 2.11 SEM second electron imaging of side surfaces for the specimens tested at 1800 K.

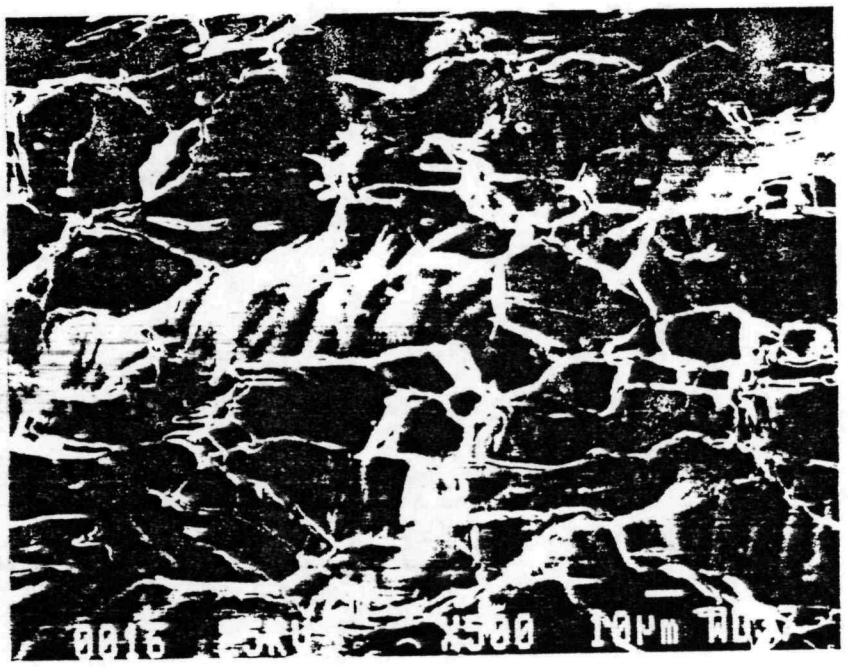

(a) W- $1ThO_2$

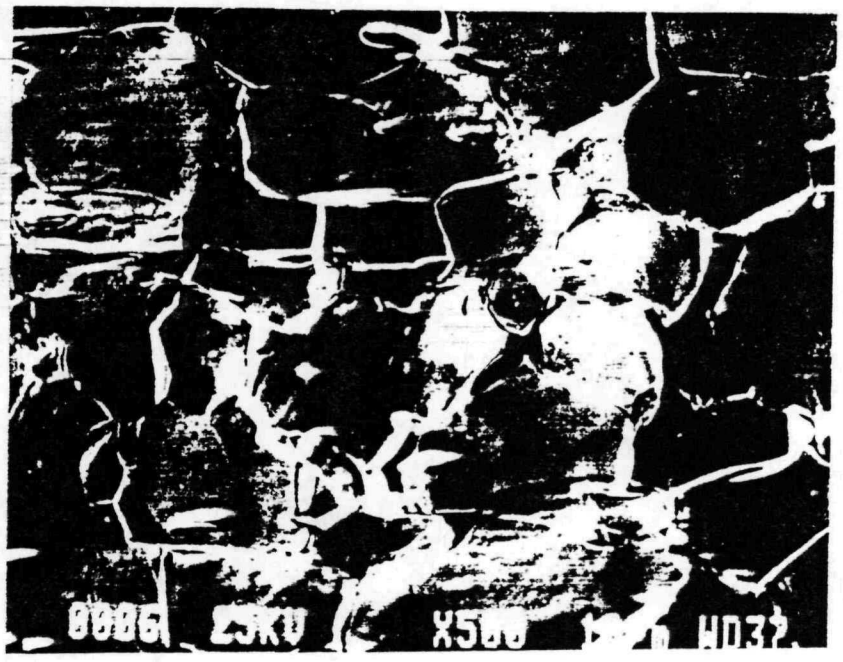

(b) W-26Re-$1ThO_2$

Fig. 2.12 SEM second electron imaging of side surfaces for the specimens tested at 2400 K.

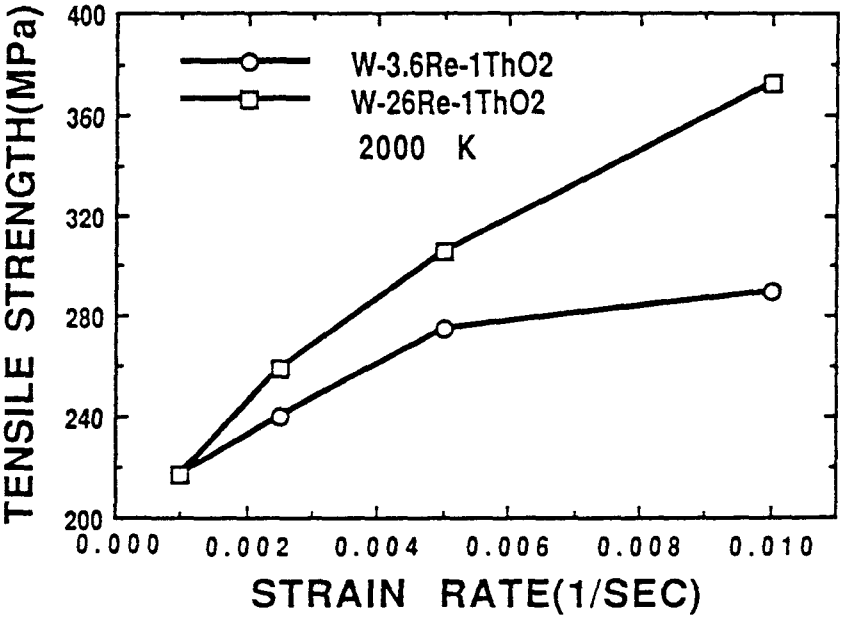

Fig. 2.13 Effect of strain rate on the tensile strength of W-3.6Re-1ThO_2 and W-26Re-1ThO_2 at 2000 K.

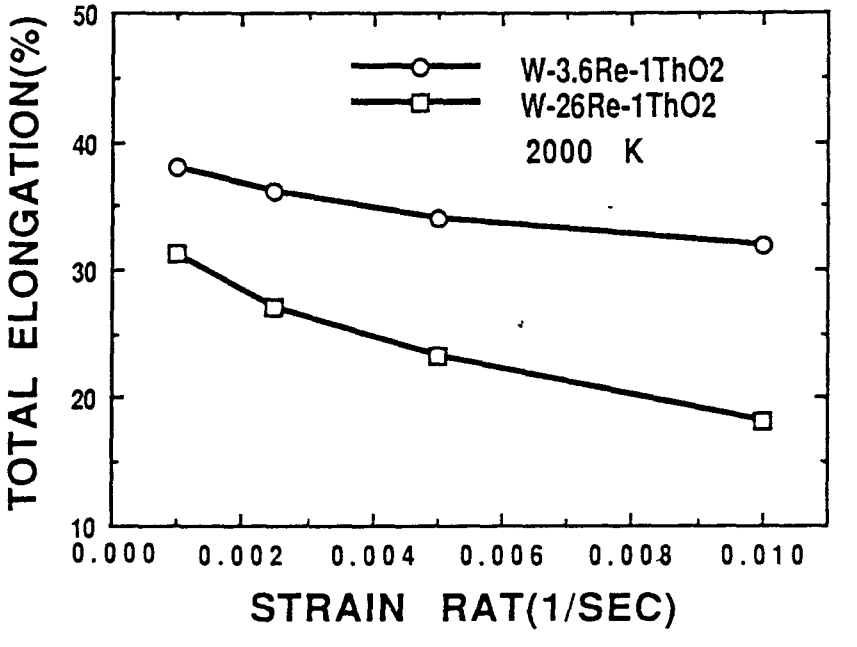

Fig. 2.14 Effect of strain rate on the ductility of W-3.6Re-1ThO_2 and W-26Re-1ThO_2 at 2000 K.

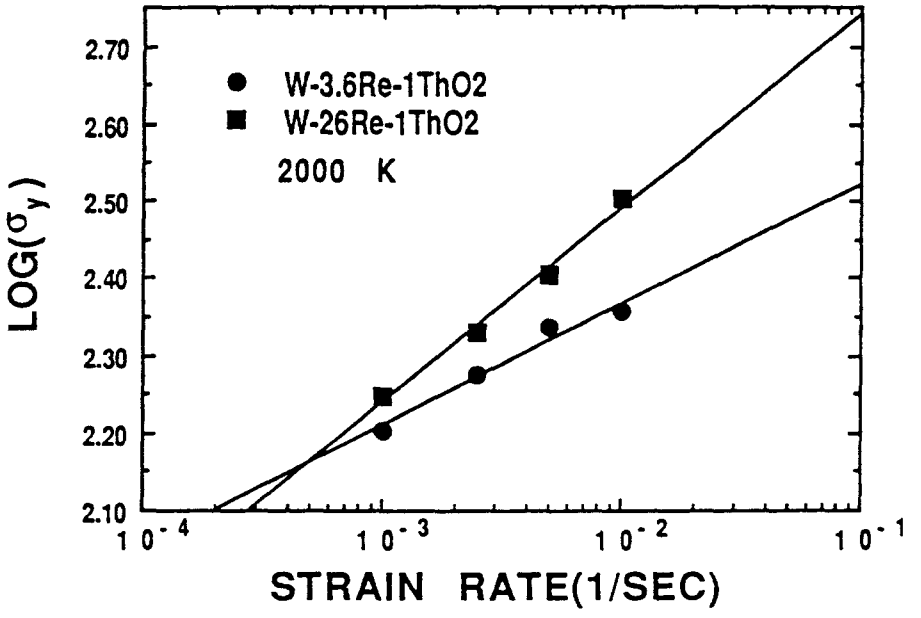

Fig. 2.15 Strain-rate sensitivities of W-3.6Re-1ThO_2 and W-26Re-1ThO_2 at 2000 K.

Re (wt.%)	Testing Temperature(K)					
	1600	1800	2000	2200	2400	2600
0.0						
3.6						
11.0						
26.0						

Transgranular Mixed Intergranular

Fig. 2.16 High-temperature fracture mode of W-Re-ThO_2 alloys as a function of temperature and rhenium content.

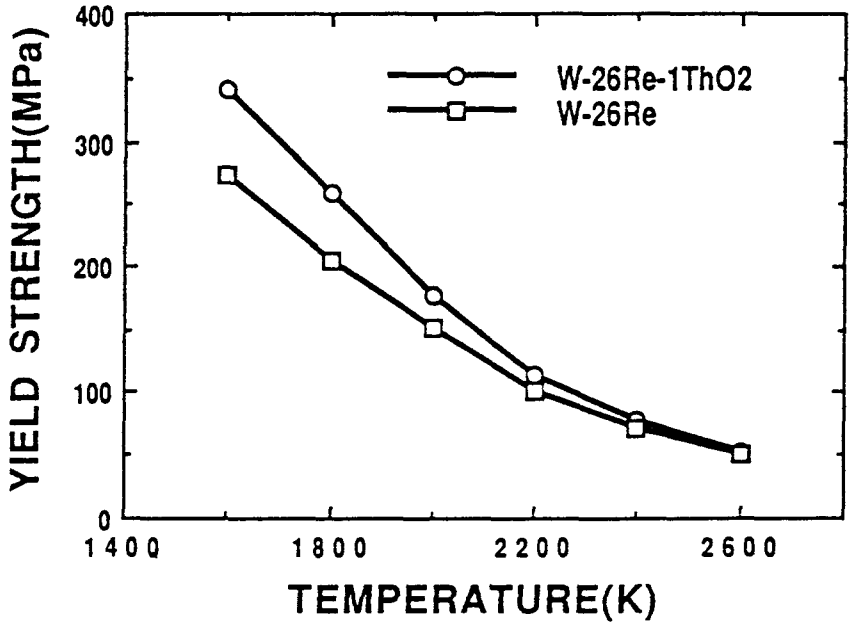

Fig. 2.17 Yield strength of W-26Re-1ThO_2 and W-26Re.

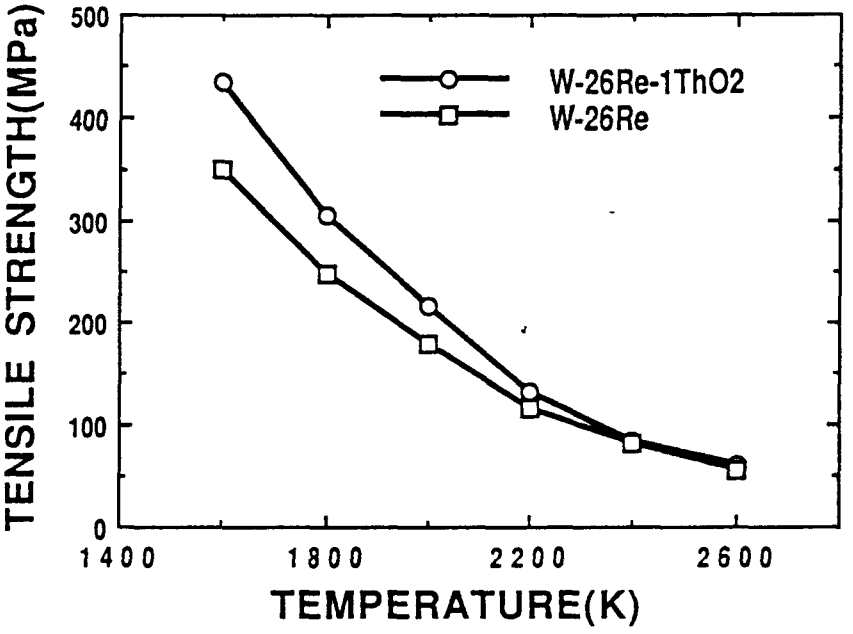

Fig. 2.18 Ultimate tensile strength of W-26Re-1ThO_2 and W-26Re.

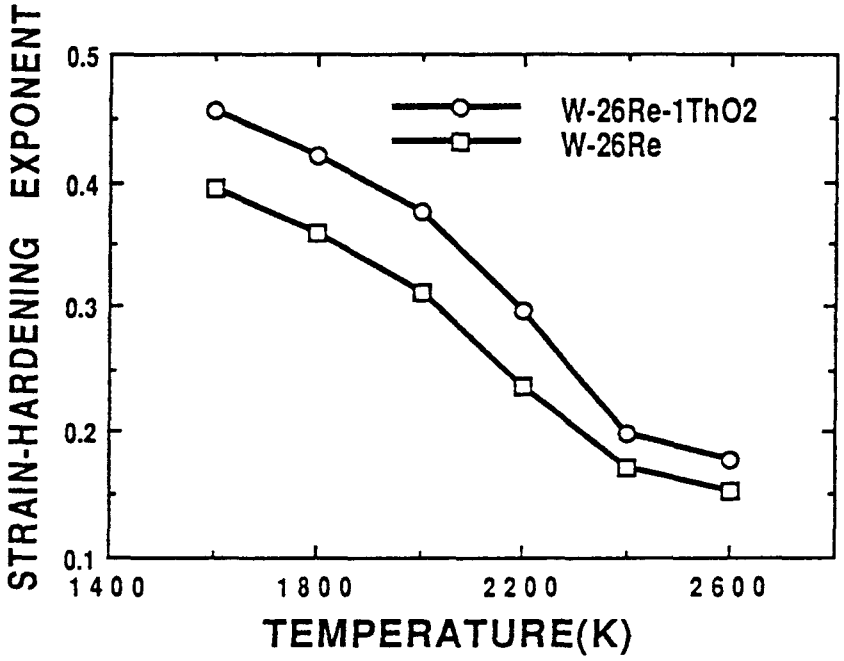

Fig. 2.19 Effect of 1.0 percent thoria on the strain-hardening exponent of W26Re.

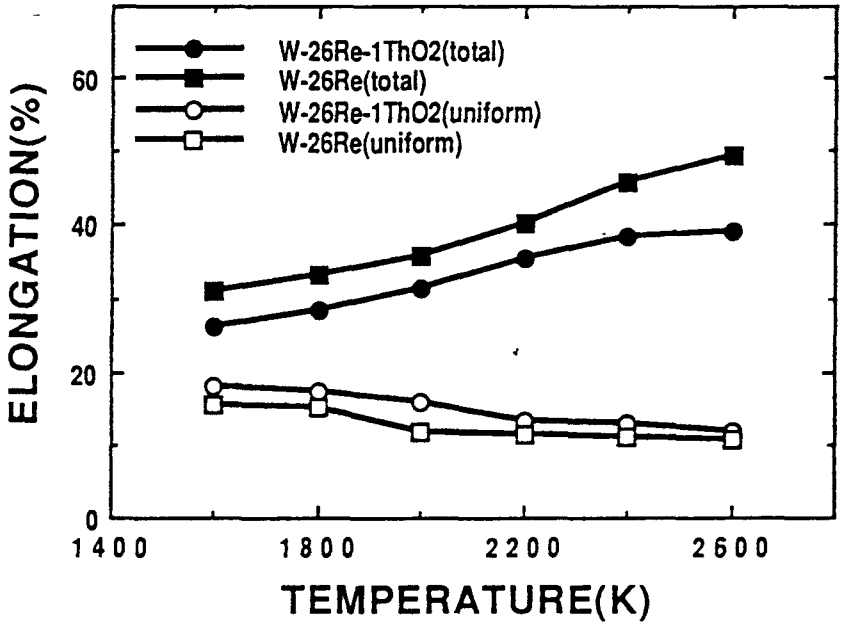

Fig. 2.20 Ductility of W-26Re-lThO_2 and W-26Re at high temperatures

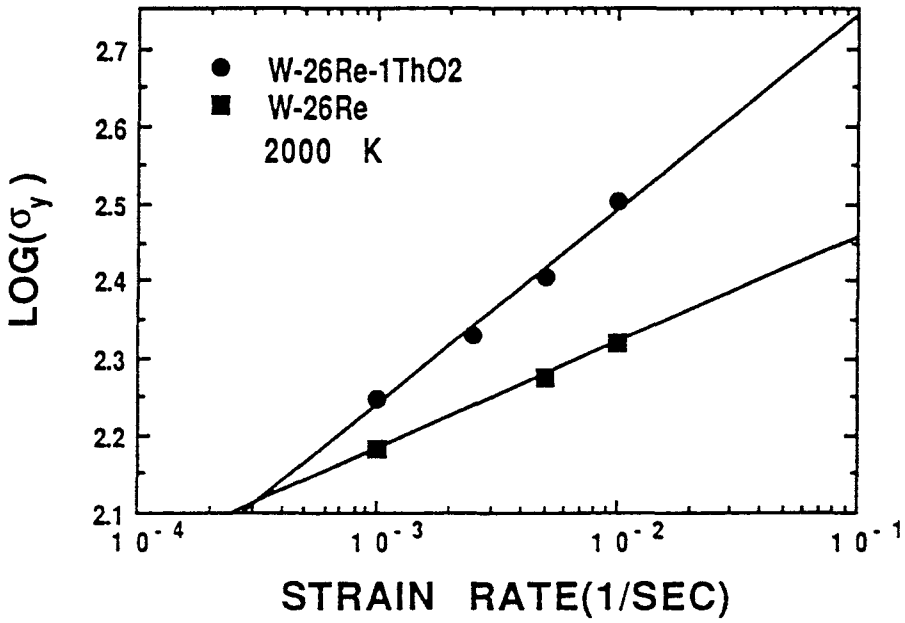

Fig. 2.21 Yield stresses of W-26Re-1ThO_2 and W-26Re as a function of strain rate 2000 K.

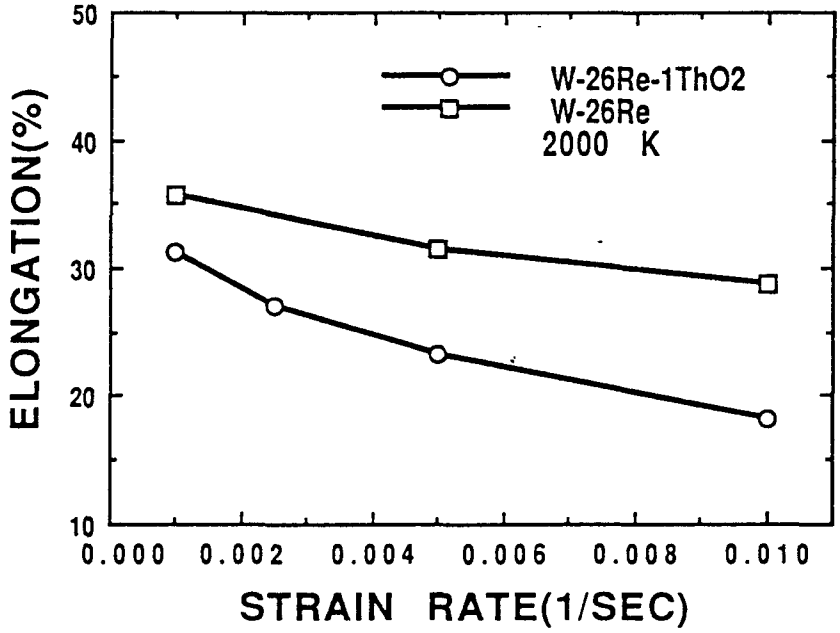

Fig. 2.22 Elongation of W-26Re-1ThO_2 and W-26Re as a function of strain rate at 2000 K.

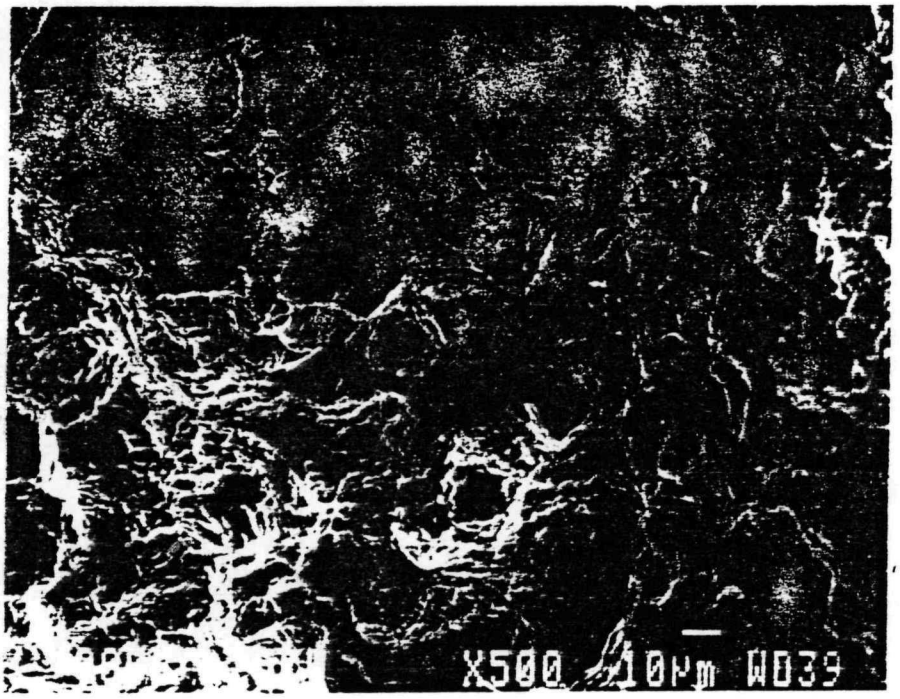

(a) W-26Re-1ThO_2

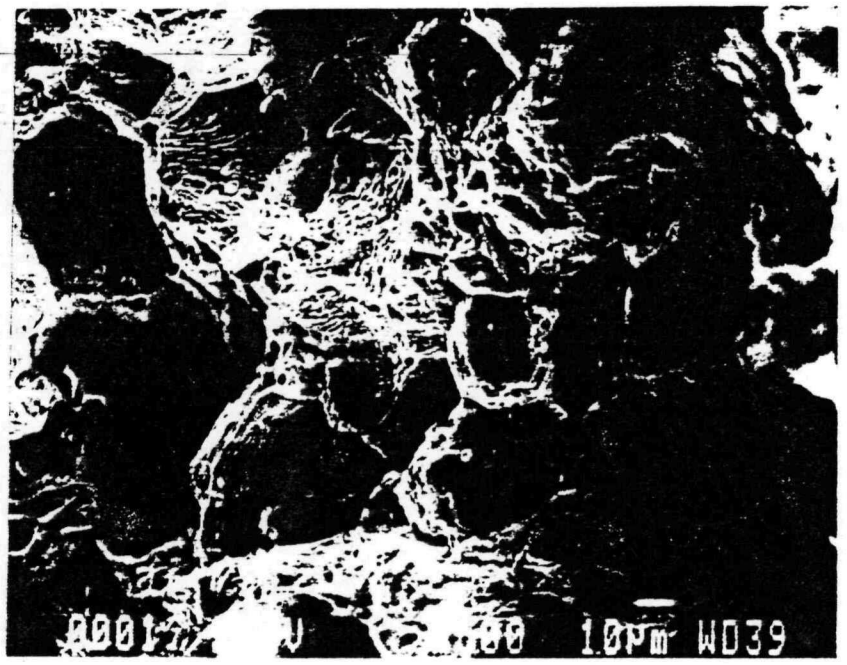

(b) W-26Re

Fig. 2.23 Fractographs of W-26Re-ThO_2 and W-26Re tested at 1800 K.

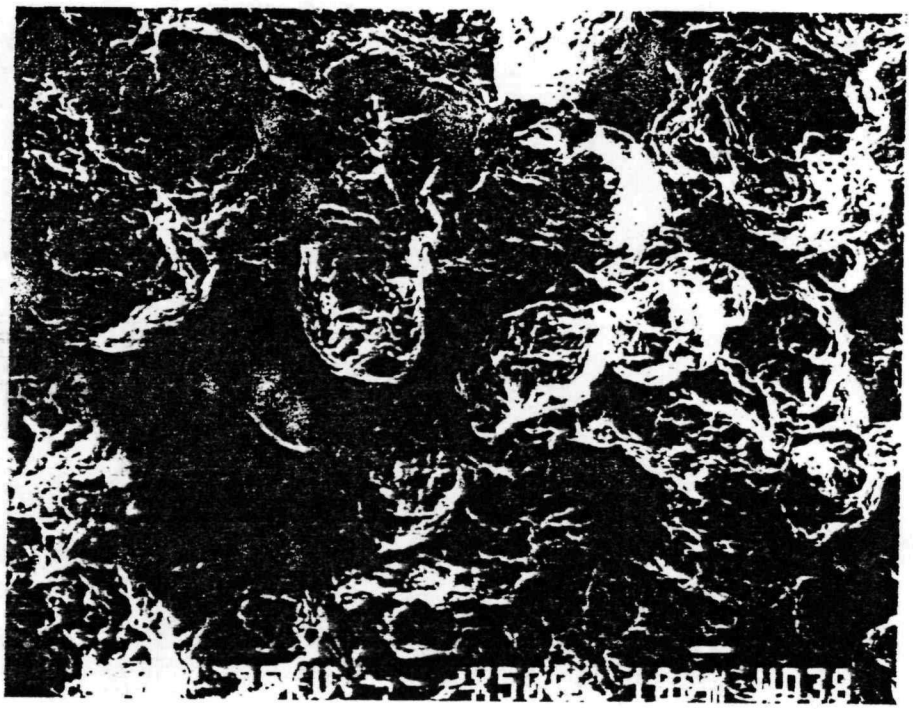

(a) W-26Re-lThO_2

(b) W-26Re

Fig. 2.24 Fractographs of W-26Re-ThO_2 and W-26Re tested 2400 K.

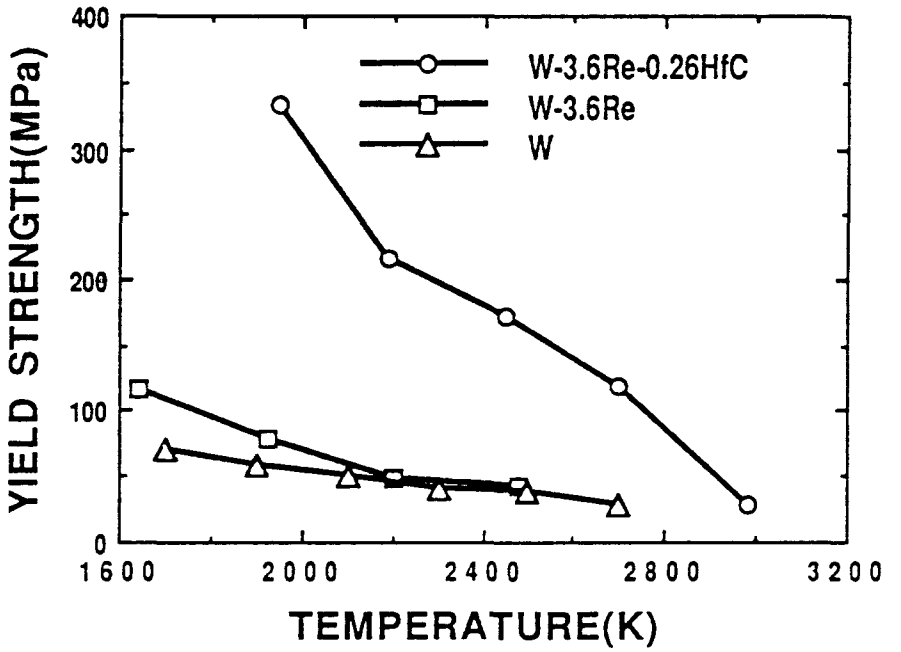

Figure 2.25 High-temperature yield strengths of arc-melted W, W-3.6Re, and W-3.6Re-0.26HfC.

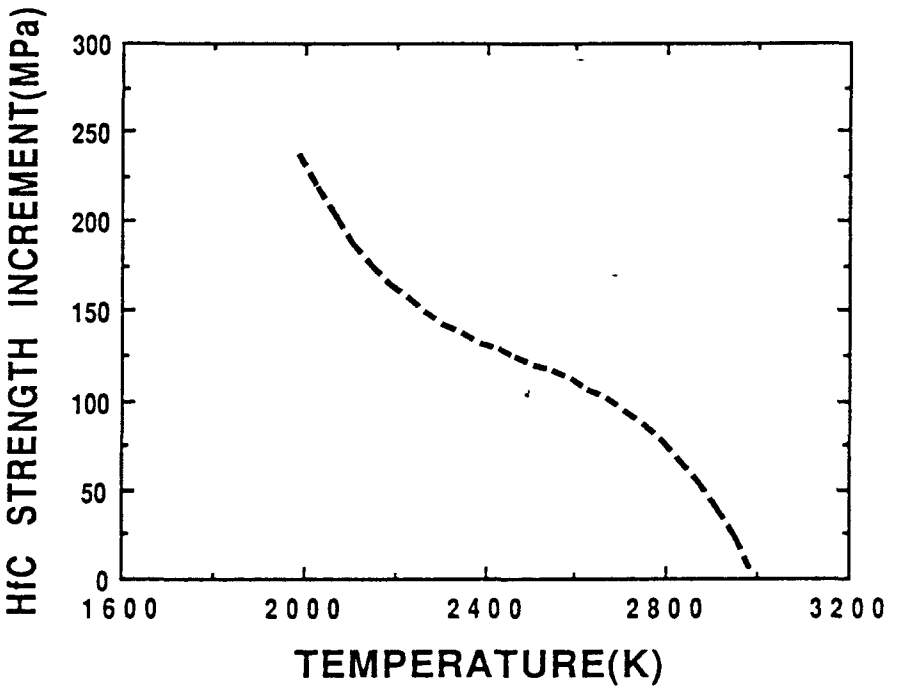

Figure 2.26 HfC strength increment in W-Re matrix from 1950 K to 2900 K.

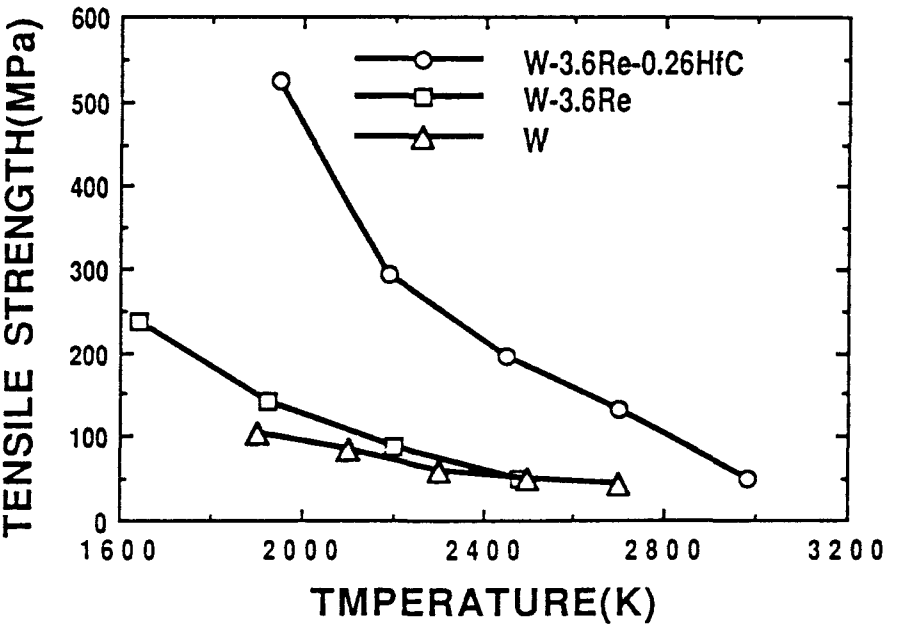

Figure 2.27 High-temperature ultimate tensile strengths of arc-melted W, W-3.6Re, and W-3.6Re-0.26HfC.

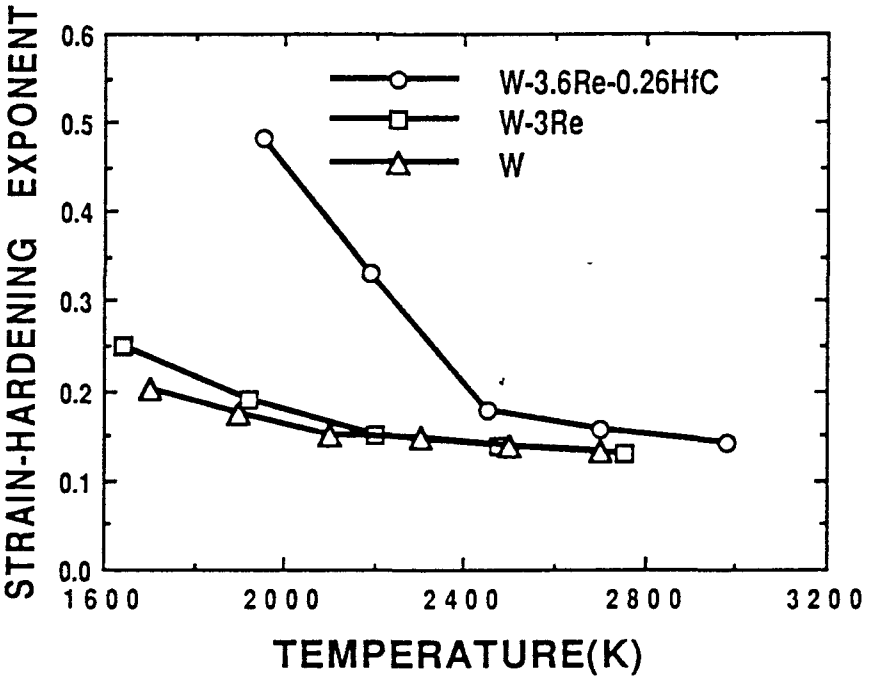

Figure 2.28 Strain-hardening exponents of arc-melted W, W-3Re, and W-3.6Re-0.26HfC.

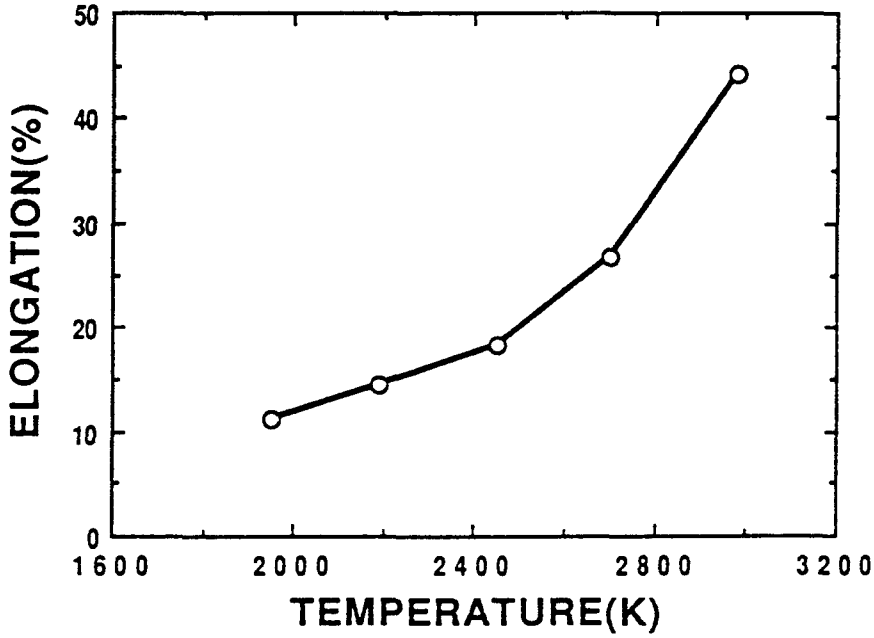

Figure 2.29 High-temperature elongation of W-3.6Re-0.26HfC.

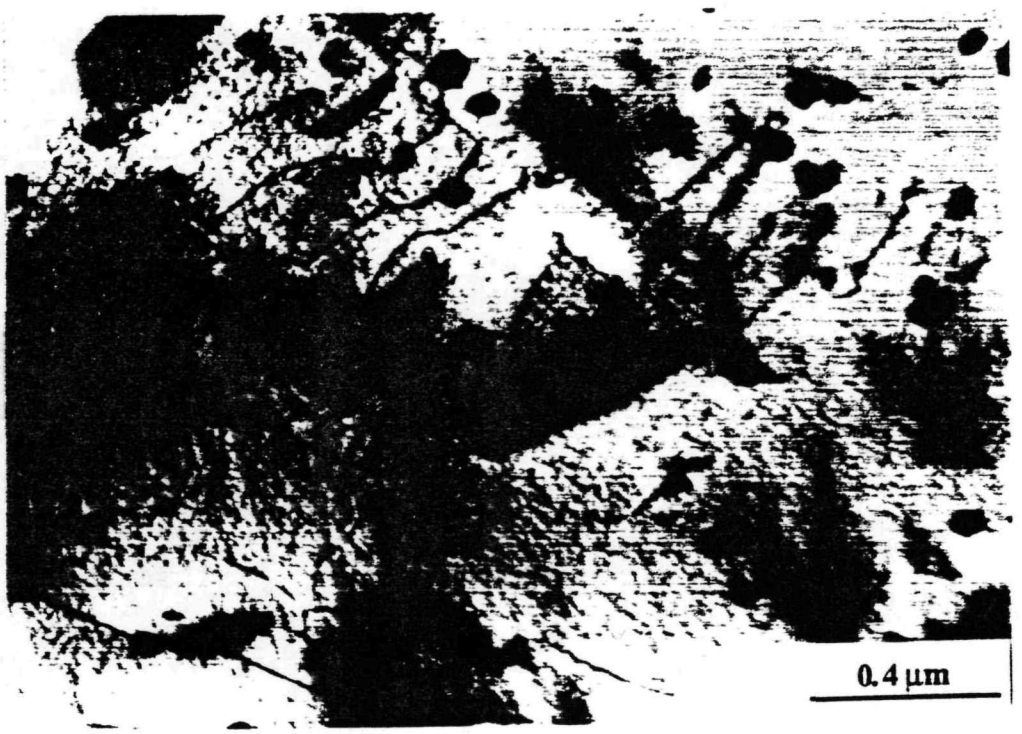

(a) 2190 K

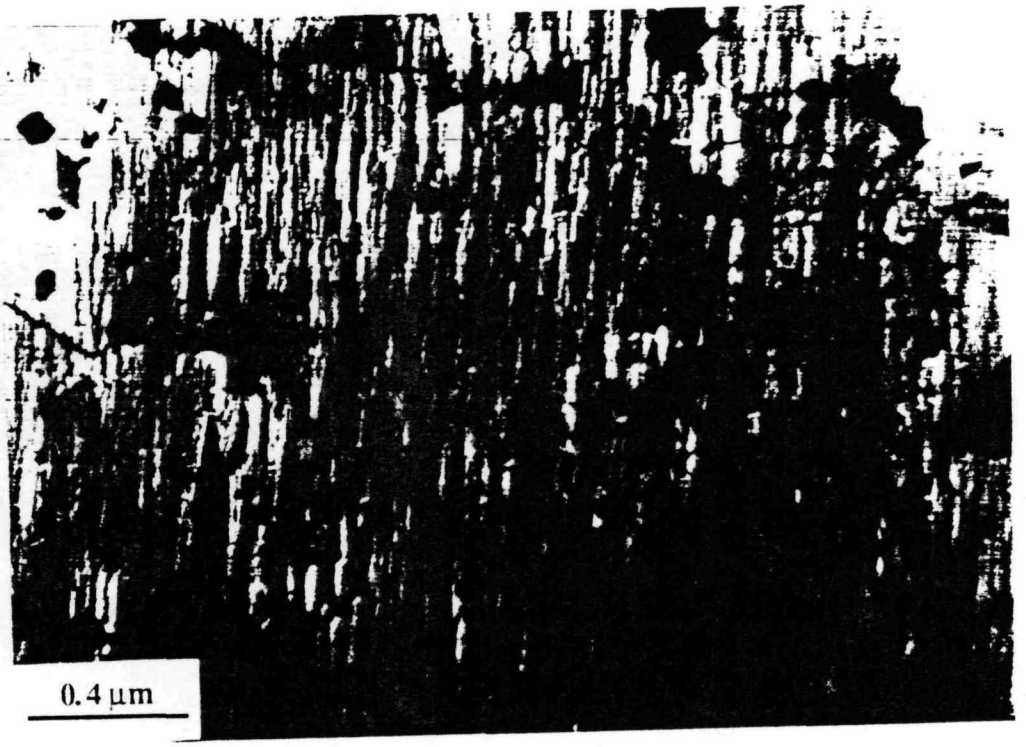

(b) 2450 K

Figure 2.30 Dislocations pinned by HfC particles in W-3.6Re-0.26HfC

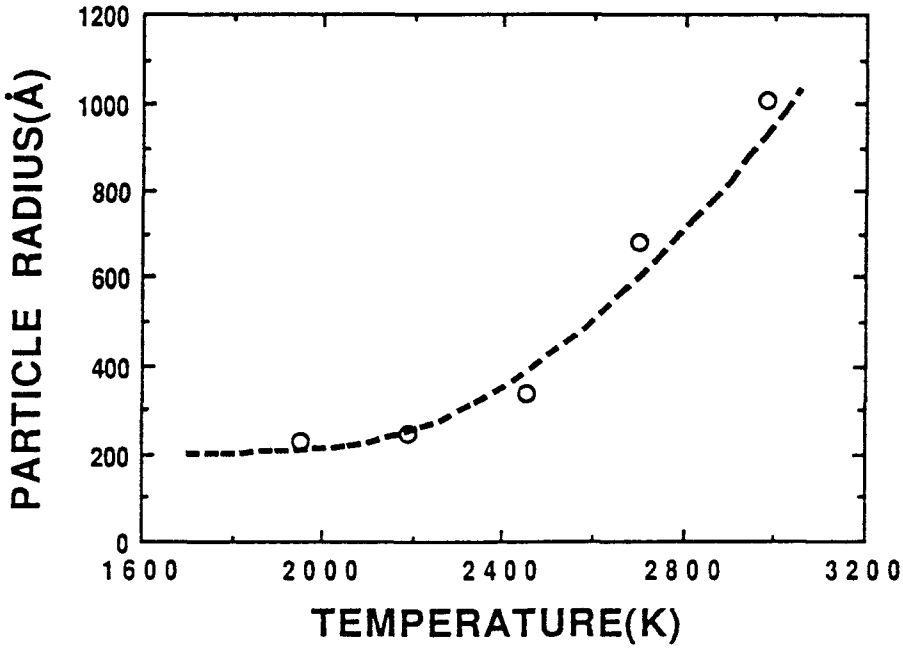

Figure 2.31 Ten-minute HfC particle size as a function of temperature.

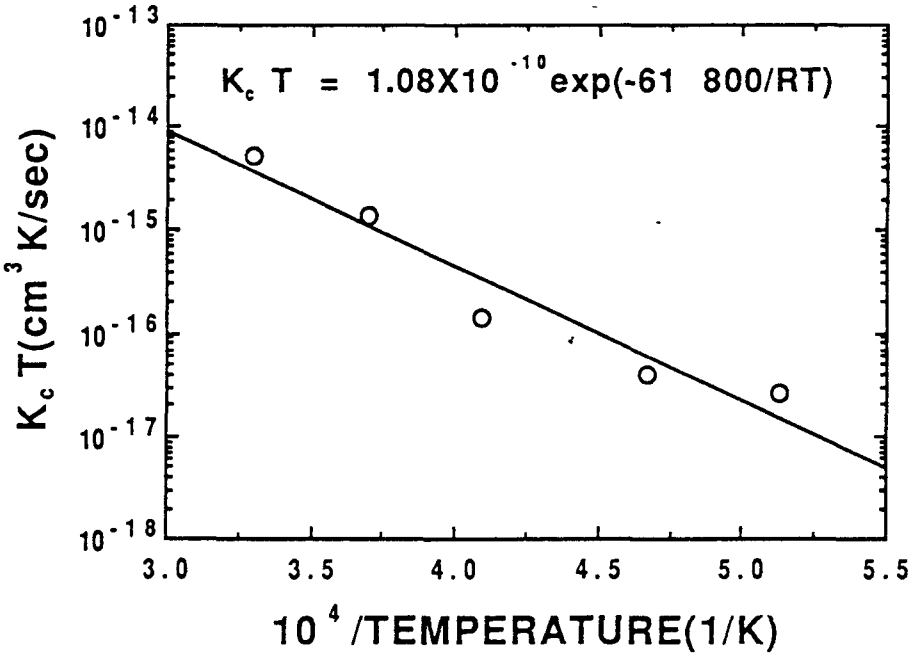

Figure 2.32 Temperature dependence of diffusivity term in HfC coarsening rate.

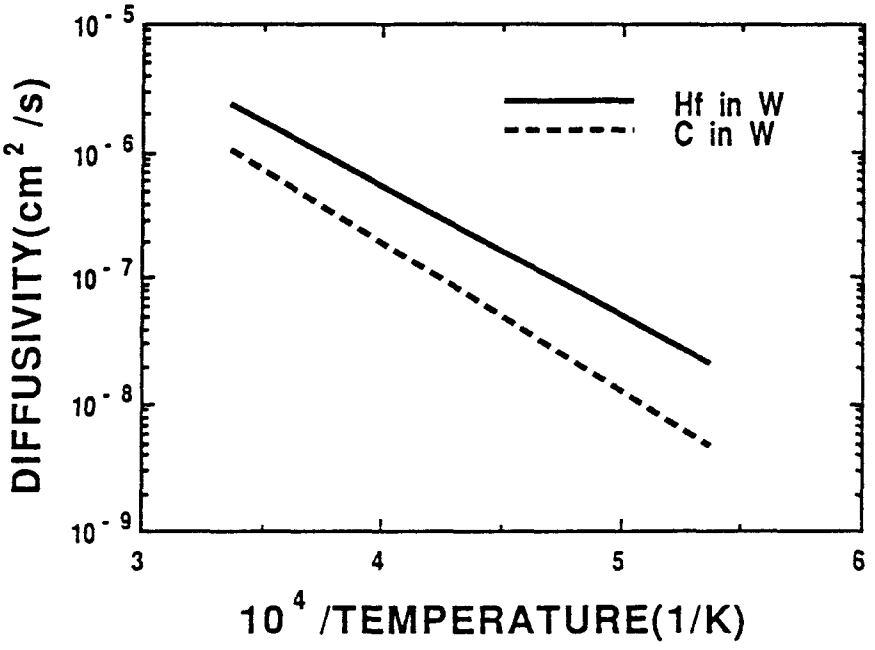

Figure 2.33 The diffusivities of carbon and hafnium in tungsten as a functionof temperature.

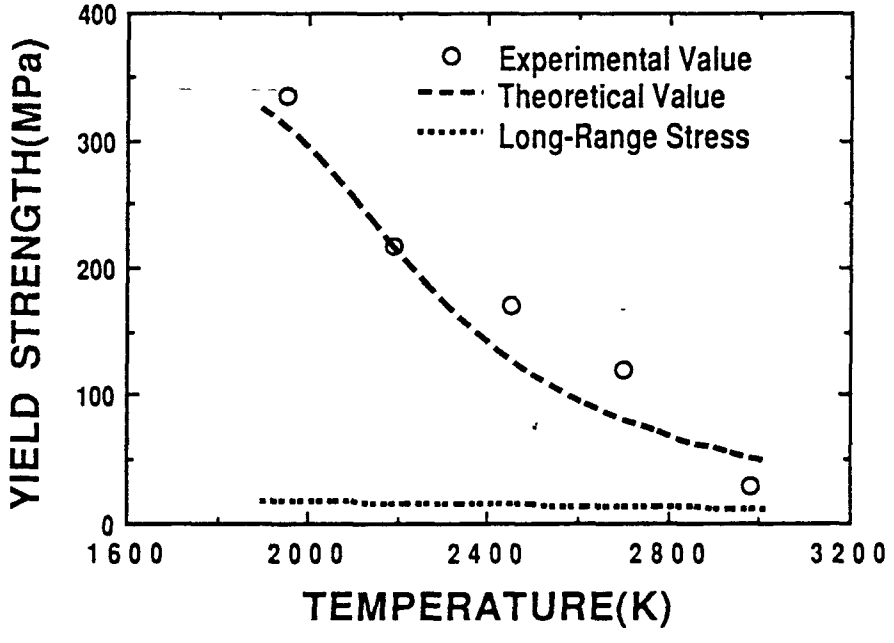

Figure 2.34 Comparison between the yield strengths predicted by the statistical approach and experimentally determined for W-3.6Re-0.26HfC.

CHAPTER 3 - CREEP PROPERTIES OF TUNGSTEN ALLOYS

3.1 INTRODUCTION

Since space nuclear power systems are required to operate at least several years at elevated temperatures in the ultrahigh vacuum of outer space, one of the most important properties of ultralloys for high-power thermionic systems is the creep resistance at elevated temperatures in vacuum. Tungsten-rhenium-base alloys are therefore being creep tested in vacuum. The creep properties of tungsten alloys reported in section 3.3 were obtained by conducting creep tests in a custom-built UHV high-temperature creep testing system, which was set up at Arizona State University and will be discussed in section 3.2.

Two tungsten alloys (W-4%Re-0.26%HfC & W-3.6%Re-1%ThO_2) have been creep tested for this project up to now. W-Re-Hf-C alloys were developed and studied in NASA Lewis Research Center during late 1960's and early 1970's[1-3]. In studying the high temperature mechanical properties of W-4Re-Hf-C alloys, Klopp and Witzke [1] found that W-4%Re-0.35%Hf-0.35%C had the optimum high-temperature strength (tensile, ductility, and creep). Therefore W-4Re-Hf-C alloys attracted most attentions as promising materials for space power applications such as space nuclear reactor(SNR) and thermionic energy convertor(TEC) [4-6]. However, the high-temperature creep behaviors of W-4Re-Hf-C alloys were not well documented. Neither creep activation energy nor rate-controlling creep deformation mechanism of this alloy system at elevated temperatures was reported. Hence one of the purpose of the present study was to evaluate the creep behavior of a W-4Re-0.26HfC (near the optimum composition) by studying the effect of stress and temperature on the steady-state creep rate. The activation energy for creep deformation was also determined and the rate-controlling creep deformation mechanism of this alloy was studied by transmission electron microscopy (TEM). The fracture behavior of this alloy at high temperatures was also studied by optical and scanning electron microscopy (SEM) examinations. The other purpose of the present study was to evaluate the creep behavior of a W-3.6Re-1ThO_2 alloy. The creep behavior of W-Re-ThO_2 alloy system have not been reported in literature. Since thoria particles have the highest melting point among oxides, W-3.6Re-1ThO_2 may have comparable creep properties with those of W-4Re-Hf-C alloys. Therefore, this alloy system could be a potential material for space-power application. In this study, the effects of stress and temperature on steady-state creep rate were evaluated and creep activation energy was also determined.

3.2 UHV HIGH-TEMPERATURE CREEP TESTING FACILITIES SET-UP

3.2.1 Introduction

This section describes the design and set-up of a creep testing system for testing W-Re-base alloys. Since the melting point of tungsten is the highest among all of the metals, the creep testing system designed must have the capability of testing tungsten alloys at temperatures above 1850 K(> $0.5T_m$, where T_m is the melting point in Kelvin). Moreover, since tungsten alloys tend to oxidize at high temperature, this creep testing system must be an ultra-high vacuum system. Most of the creep testing system described in literature have been concerned with testing at temperatures up to about 1000°C. Only a few papers described the ultra-high temperature creep testing machine. Smith et al. [7] described a testing machine for short-time creep and creep-rupture testing at 2000 to 2500°C by using a tantalum-tube resistance heater. This machine was used in determining creep and stress-rupture properties at 2000 to 2500°C (in vacuum or in helium atmosphere) over periods of a few minutes to an hour or so. A heating current of about 1000 amp at 6 volts is required to reach a specimen temperature of 2000°C, and about 1600 amp at 8 volts to reach 2500°C for this machine. Taylor [8] developed an apparatus for tensile testing at temperatures up to 5400°F in vacuum by using an induction coil. Induction power is used to heat the specimen by radiation from a susceptor. The power supply consists of a 50-KW, 440-V, 10000-cycle motor generator unit and output station. He claimed that the furnace had been maintained at a temperature of 5000 °F for over 70 minutes and at 5400°F for over 35 minutes. Inouye [9] used a direct resistance heating apparatus to measure the creep of refractory alloys in low-pressure oxygen. Buzzard [10] used a split-type tungsten-mesh heating element creep testing machine to study the effect of grain size on creep properties of a tungsten alloy from 1800 to 4000°F. Test data were obtained up to 5000 hours. Klopp [1] et al. also used similar creep testing machine to study the creep properties of a W-Re alloy.

3.2.2 The Design and Set-up of Creep Testing System

The high-temperature high-vacuum creep testing machine designed for the present project is a direct resistance-heating type. The reason for not setting up a split-type tungsten-mesh heating element creep testing machine is due to the limited budget for capital equipments in this project. According to Centorr Associates, Inc., the high- vacuum high-temperature (2500°C max.) testing chamber, including power supply, will cost more than sixty thousand dollars. The load train and data recording facilities are not even included. Therefore, to use the budget more efficiently and at the same time shorten the creep testing machine set-up time, direct resistance-heating type machine was designed and built.

Fig. 1 shows the schematic diagram of the creep testing apparatus designed. This creep testing system can be divided for the purposes of discussion into four units: (a) heating unit, (b) sample loading unit, (c) vacuum unit, and (d) data recording unit.

(a) Heating Unit: Heating unit consists of a power supply, a medium-current feedthrough, copper electrodes, optical pyrometer, and a tantalum heat shield.

The AC power supply is custom-built. Its maximum output is 6 KW (20V, 300A). The maximum current for the feedthrough is 150 A. The maximum specimen temperature capable for this design depends on the specimen cross-section area. For the specimen used in this study, temperature can be maintained at 2500°C for more than 50 hours.

(b) Sample Loading Unit: Sample loading unit consists of the following parts:

(1) Grips
(2) Pull rods
(3) Connecting block
(4) Coupling
(5) Weight
(6) Weight pan
(7) Bellows
(8) Pins
(9) Load cell

Where grips and pins were made of TZM molybdenum alloy to withstand high temperature for a long period of time. Connecting block was made of Inconel-750, while pull rods and coupling were made of stainless steel.

The grips were designed for testing plate-type specimens. To test cylinder-shaped or fiber specimens, grips have to be modified. The load train was designed in such a way that load can be applied to the specimen through a bellows. The desired load can be measured by a load cell which is right under the bellows. The maximum load can be applied in this machine is 200 pounds.

(c) Vacuum Unit: Vacuum unit consists of the following:

(1) Mechanical pump
(2) Sorption pump
(3) Ion pump
(4) Ion pump power supply
(5) Ionization gauge controller
(6) TC gauge
(7) Right-angle valves
(8) Vacuum chamber

This vacuum unit can obtain a vacuum of 8×10^{-7} torr at elevated tewperatures. The vacuum of the chamber can be further improved by using an ion pump with higher pumping capability.

(d) Data Recording Unit: Data recording unit consists of an linear variable differential transducer (LVDT), a computer, a monitor, a printer, and the interface accessaries (i.e. signal conditioning module, and data acquisition and control interface board). This unit is for the periodical reading and recording of the displacement data.

To record creep data, a special computer software program was developed. This program can control this data recording unit to displace, print out, and record the creep time, displacement and creep strain automatically.

Fig. 2 shows the picture of the creep testing system which was set up in Arizona State University. Fig. 3 shows the TZM grips (loaded with a W-4Re-0.26HfC specimen) designed for this machine.

3.2.3 Conclusions

To design and set up a high-temperature and high-vacuum creep testing system is challenging, not only because the literature or information available is rare, but also because to maintain a temperature higher than 0.5 T_m in vacuum for a long time is not easy.

A high-temperature high-vacuum creep testing system was set up in Arizona State University and successfully used in creep testing tungsten alloys at tempertures up to 2783 K for 50 hours in a vacuum of 8×10^{-7} torr. The testing temperature can be further increased by reducing the cross-section of the specimen. The vacuum of the chamber can also be improved by using an ion pump with higher pumping capability.

3.3 HIGH-TEMPERATURE CREEP PROPERTIES OF TUNGSTEN ALLOYS

3.3.1 Experimental Procedure

(A) Materials

The materials used in this study are:

(a) W-4 Re-0.26HfC, arc-melted and swaged, 1 inch in diameter bar, supplied by NASA Lewis Research Center. The chemical compositions of this material was checked with microprobe analysis, and is shown in table 3.1.

(b) W-3.6Re-1ThO_2, powder metallurgy alloy, sintered and swaged, 0.25 inch in diameter rod, supplied by Rhenium Alloys Inc., Cleveland, Ohio. The chemical compositions of this alloy is shown in table 3.2

Table 3.1 Chemical Composition of W-4%Re-0.33%HfC

W	Re	Hf	Ir	Th	Ta
Balance	3.95	0.26	0	0	0

Table 3.2 Chemical Composition of W-3.6%Re-1%ThO_2

W	Re	Th	Hf	Ir	Ta
Balance	3.60	1.01	0	0	0

Note:1. Unit of the compositions is weight %.
2. Data shown above is the average of ten readings.

Plate-type specimens were machined with an electric discharge machine (E.D.M.). The dimensions of the plate-type specimen were shown in Fig. 4. The specimens were first mechanically polished as usual and then chemically polished in a 10% NaOH solution.

(B) Testing

The creep properties of these alloys were studied by performing step-load and step-temperature creep tests in the vacuum chamber described in section 3.2. Prior to heat treatment and testing, a small load was placed to the specimen to stabilize the load train. Frequent adjustment of this load was necessary during heating because of thermal expansion. In order to have a homogeneous

microstructure for each specimen before creep test, specimens were in-situ heat treated in vacuum chamber right before creep tests. In-situ heat treatments of the specimen consisted of degassing the specimen at 1273 K for 12 hours under a vacuum of 8 x 10^{-7} torr followed by recrystallization annealing at 2100 K for 2 hours and then heated at the test temperature for 30 minutes to stabilize the temperature of the specimen. After finishing the in-situ pretest heat treatment desired load was applied to the specimen through a bellows. Strain was detected by using a linear variable differential transducer (LVDT). Test temperature was measured with an optical pyrometer through a viewport. The optical pyrometer was calibrated with a ribbon filament lamp prior to testing. Step-load creep tests were conducted at temperatures ranging from 1955 to 2500 K and at stresses from 10 to 70 MPa. All the creep tests were carried out in a vacuum of 8 x 10^{-7} torr. Afer creep testing, the specimens were examined with an optical microscope and a JXA-840 scanning electron microscope to study the fracture behavior of these alloys. The dislocation substructures of the alloy before and after creep tests was evaluated by transmission electron microscopy. Thin foils for electron microscopy were prepared from materials taken from the gauge section of each specimen by first mechanical polishing to a thickness of 70 micrometers, and then thinned by using a Tenupol-3 double jet electropolishing machine in a 2 pct NaOH solution. Thin foils were examined in a JEOL 2000FX microscope operated at 200 KV.

3.3.2 Results and Discussions

In the following, the results obtained for W-4Re-0.26HfC will first be given and discussed. The data for W-3.6Re-1ThO_2 will then be discussed and compared with those of W-4Re-0.26HfC.

(A) W-4Re-0.26HfC

Resulting creep data for this alloy are presented in Table 3.3. The typical step-load strain-time creep curves of this alloy tested at various temperatures are shown in Fig. 5. It shows the normal three-stage creep, i.e. primary, steady-state, and tertiary creeps. Upon initial loading a primary creep region with decreasing creep rate occurred followed by a steady-state creep region with a constant creep rate. After the steady-state creep rate was measured at a given stress, the stress was abruptly changed to a new level and the primary creep took place again. Eventually tertiary creep occurred with necking in the gauge section. The effect of stress and temperature on the steady-state creep behavior can be obtained by analyzing these creep curves.

3.3.2.1 The Effect of Stress on Steady-State Creep Rate

Fig. 6 shows stress-dependence of the steady-state creep rate of this alloy at various temperatures. It shows a power-law relationship between creep rate and creep stress and can be expressed as

$$\dot{\varepsilon} = A\sigma^n$$

where $\dot{\varepsilon}$ is the steady-state creep rate, σ is the applied stress, A is a constant, and n is the stress exponent of creep deformation, which is an indication of the stress sensitivity of steady-state creep rate. The values of n obtained in this study range from 5.0 to 5.5 at temperatures from 1955 to 2500 K. It appears that the stress exponent of this alloy is not sensitive to the test temperatures used in this study. The average value of the stress exponent can be calculated as 5.2. This value is in fair agreement with the value of n=5 reported by Robinson and Sherby [11] for arc-cast and electron beam melted tungsten. Vandervoort obtained a value of n=5.5 in studying the creep behavior of a W-5Re alloy [12]. However, Rubenstein found the value of n ranged from 10 to 13 for arc-melted W-Hf-C alloys [13]. He attributed the high stress exponent value of those alloy to the internal stress raised by the precipitate-stabilized fine dislocation structure.

3.3.2.2 The Effect of Temperature on Steady-State Creep Rate

The temperature-dependence of the steady-state creep rate for the W-4Re-0.26HfC alloy at various stresses is shown in Fig.7. The activation energies for creep deformation of this alloy at various stresses are also shown in this figure. They were calculated from the formula

$$Q_C = R \ln(\dot{\varepsilon}_2/\dot{\varepsilon}_1)/(1/T_1 - 1/T_2)$$

where $\dot{\varepsilon}_1$ and $\dot{\varepsilon}_2$ are the steady-state creep rate at temperatures T_1 and T_2 (in absolute temperature). At temperatures range from 1955 to 2190 K, the activation energies range from 101 to 110 Kcal/mole with an average value of 105.5 Kcal/mole. While at temperatures from 2300 to 2500 K, the average activation energy was calculated to be 161.9 Kcal/mole. It is well known that the activation energy for creep deformation usually corresponds to an activation energy for self-diffusion at temperatures above 0.5 T_m [14]. However, by combining data from the literature, Robinson and Sherby reported that the creep activation energy varied with temperature for polycrystalline tungsten [11]. For temperatures above 0.65 T_m the activation energy for creep approaches the activation energy for lattice self-diffusion Q_l (=140 Kcal/mol [15] or 153 Kcal/mol [16]). While for temperatures below about 0.6 T_m the creep activation energy of tungsten is the same as the activation energy for dislocation core diffusion Q_d (=90.5 Kcal/mol [17]) or grain boundary diffusion Q_{gb} (=92.5 Kcal/mol [17]). There is a transition region between 0.6 and 0.65 T_m, where the creep activation energy increases with increasing temperature. From the results obtained in this study, it is clear that our results is consistent with that proposed by Robinson and Sherby. Apparently, the rate-controlling mechanism for creep of this alloy at temperatures ranging from 1955 to 2190 K appears most likely to be diffusion controlled dislocation climb. While the rate-controlling creep mechanism at temperatures ranging from 2300 to 2500 K is lattice self-diffusion.

3.3.2.3 Microstructure Characterizations

The as-swaged and recrystallized optical microstructures of W-4Re-0.26HfC are shown in Fig. 8 (a) and (b), respectively. The material was completely recrystallized by in-situ annealing at 2450 K for 1.5 hours, as can be seen in Fig. 8 (b). Fig. 9 and 10 show the typical optical and SEM microstructures observed on the side surfaces of the specimen after creep tests. They show sliding offsets of surface scratches and wedge-shaped intergranular cracks resulting from grain-boundary sliding examined on the step-load creep specimen tested at 2190 K. The wedge-shaped cracks observed were tend to be normal to the stress axis. Thermal etching of the specimen can also be observed on these two figures. It was also observed that grain boundary migration took place during creep. Many migration irregularities were formed by grain boundary migration during creep and they act as potential sites of the stress concentration and crack nucleation on sliding grain boundaries, as shown in Fig. 11. Irregular-shaped cracks are developed on the boundaries where migration occurs. The irregular migration often occurs on grain boundaries inclined to the stress axis. SEM fractographs of the specimens creep tested at 2190 and 2300 K are shown in Fig. 12 and 13, respectively. They show clearly the intergranular fracture mode of the materials tested at these two temperatures. Fig. 13 also show wavy slip lines observed on some grains adjacent to the fracture surface. Creep specimens tested at other temperatures also show the same results. Therefore, it can be concluded that the rupture of the creep specimens is due to wedge-shaped intergranular cracks and irregular intergranular cracks (due to grain boundary migration). Both of these two intergranular cracks are caused by grain boundary sliding.

Fig. 14 shows a typical transmission electron micrograph of the specimen in swaged condition. It illustrates the dislocation cell structure with boundaries containing high density of dislocation tangles pinned by second phase particles. Typical transmission electron micrographs of W-4Re-0.26HfC after annealing and creep testing are shown in Fig. 15 to 27. The 1955 K creep tested

structure in Fig. 15 shows well-defined subgrains and globular hafnium carbide particles associated with subgrain boundaries as well as individual dislocations pinned by HfC particles. As shown in this figure, the subgrain boundaries were formed by dislocation networks. Fig. 16 shows individual dislocations pinned by HfC particles found in the specimen tested at 1955 K. From these transmission electron micrographs the HfC particle diameters were measured to ranged from 100 to 830 A. Numerous fine precipitates (less than 100 A in diameter) were also formed during creep test, as can be seen in Fig. 17. In this figure, it can also be seen that dislocations were pinned by HfC particles and no Orowan looping around particles can be found. In Fig. 18 numerous second phase particles were seen to locate in the grain boundary of the specimen tested at 2070 K. They act as obstacles for the movement of grain boundaries. After carefully examine the grain boundary structure in this picture, it is found that boundaries contain periodic grain boundary dislocation arrays, as pointed by arrows. Subgrains were also found in 2070 K creep tested specimens. Their boundaries were also formed by dislocation networks and some globular hafnium carbides were found in these subgrain boundaries just as in the case of 1955 K creep tested samples. Fig. 19 shows that individual dislocations in the interior of the subgrains are pinned by HfC particles. No Orowan looping was observed around the particles, which indicates that the dislocations by-pass the HfC particles by a climb mechanism. Fig. 20 and 21 show the dislocation networks found in the 2190 K creep tested specimen. The dislocations were well knitted to form the subgrain boundaries. Dislocation networks consist of two or three dislocation families were found in this specimen. Fig. 20 shows an example of the networks with two dislocation families. Fig. 21 shows an example of the hexagonal networks with three dislocation families. The size of the second phase particles in specimens tested at 2070 and 2190 K were measured to range from 200 to 900 A in diameter. Numerous fine second phase particles (less than 100 A in diameter) were also found in the matrices of the 2070 and 2190 K creep tested specimens, as shown in Fig. 18 and 20. Hafnium carbide particles are also very effective in pinning subgrain boundary dislocations at temperature as high as 2190 K. Fig. 22 shows clearly the pinning effect of HfC particles on the subgrain boundary dislocations. It can be seen that dislocations in the networks are pinned by HfC particles (at A, B, and C), and therefore dislocation lines near the particles are somewhat distorted. No evidence of Orowan looping can be seen either in the boundaries or in the interior of the subgrain. It is also very interesting to find that the dislocations are usually seen to be pinned by the particles at the departure side of the particles. This phenomenon has been reported by several researchers in studying creep behavior of ODS (Oxide-Dispersion- Strengthened) alloys [18-21]. It was explained that an attractive force existed between dislocations and incoherent oxide particles as a results of a lower energy configuration [19]. Nardone and Tien attributed the existance of the threshold stress for ODS alloys to this attractive interaction between particle and dislocation [19]. However, the creep stresses applied on the specimens in this study are well below the threshold stress. According to Nardone and Tien, the creep rate of this alloy should be negligible. Obviously, their model can not applied to this tungsten alloy. This is mainly due to the fact that hafnium carbide particles are coherent particles, while their model was proposed for incoherent oxide particle strengthened alloys. Grain boundary migration can also be observed in the creep tested specimen, as shown in Fig. 23. This figure shows that the grain boundary is migrating from left-hand side to right-hand side. A particle at A hinder the movement of the grain boundary. Therefore, the grain boundary has to by-pass the particle by a climb mechanism. As temperature increased above 2200 K, hafnium carbide particles coarsened rapidly. Fewer and fewer dislocations can be found in the crept specimens as test temperature getting higher and higher. Also the dislocation networks are rarely found in these specimens. Instead, low angle grain-boundary is frequently seen, as shown in Fig. 24. Figs. 25, 26, and 27 shows the TEM micrographs of the specimens tested at 2300, 2400, and 2500 K, respectively. The HfC particle size measured range from 500 A to 5000 A in diameter.

3.3.2.4 Deformation mechanisms for creep

In this section the possible rate-controlling creep deformation mechanisms of W-4Re-0.26HfC are discussed according to the creep data obtained as well as the dislocation substructures observed in TEM.

Although the value of the stress exponent of this alloy is very close to that predicted by climb-controlled glide model proposed by Weertman [22], this model doesn't seem to be applicable to this alloy. Because according to Weertman the creep rate is controlled by the escape rate, by means of climb, of leading dislocations piled up at obstacles. However, TEM examination of the creep-tested samples show that dislocation pile-ups were not observed in this study.

The motions of jogged screw dislocations proposed by several researchers [23-25] can also be precluded as the rate-controlling deformation mechanism for this alloy from the results obtained in the stress-change creep test and the TEM observations. The observation that an incubation stage was obtained following the stress reduction in the stress-change creep test indicates that dislocation glide processes, such as the glide of jogged screw dislocations, are not rate-controlling deformation mechanisms during creep of W-4Re-0.26HfC, since with this type of process, a small stress reduction should be followed by a new slightly lower creep rate and not by a period of zero creep rate. In addition, from the TEM observations, it was found that the dislocations in the creep structure are predominately edge character. Therefore, the glide of jogged screw dislocations can be precluded as a rate-controlling mechanisms for this alloy.

Ansell and Weertman [26] developed the first model for high-temperature creep of alloys hardened by second-phase particles. They assumed that the rate-controlling process is the climb of dislocation over the second-phase particles. They suggested that at low stresses the dislocations climb over the particles with no pile-up or bowing of dislocations at the particles, while at high stresses ($> \mu b/\lambda$, where μ is the shear modulus, b the Burgers vector, and λ the interparticle spacing) the dislocations move past particles by bowing out and pinching off loops around the particles. The steady state creep rate at high stresses is then governed by the rate at which the dislocation loop nearest to the particles climb to the top of the particle and is annihilated; the other loops then move inwards, and a new loop forms by bowing and pinching off an arrested dislocations. Based upon the above assumptions, they arrived at the following expression of the creep rate at low stresses:

$$\dot{\varepsilon} = \frac{\pi \sigma b^3 D}{2 k T d^2}$$

where σ is the applied stress, b the Burgers vector, D the diffusion coefficient, k Boltzmann's constant, T the temperature, and d the particle size. At high stresses they obtained the following equation:

$$\dot{\varepsilon} = \frac{2 \pi \sigma^4 \lambda^2 D}{d \mu^3 k T}$$

where λ is the interparticle spacing and μ is the shear modulus. From these two expressions, they concluded that at a given particle size and spacing a stress exponent of 1 was expected at low stresses, increasing to a value of 4 at high stresses. The stresses applied in the present study were smaller than $\mu b/\lambda$, and therefore the stress exponent of the alloy in the present study should expect a value of 1 according to the theory of Ansell and Weertman. However, a value of 5.2 was obtained for W-4Re-0.26HfC in the present study. Moreover, this theory also predicts that at low stress and, for a given volume fraction of particle, the steady state creep rate should decrease with increasing particle diameter (i.e., $\dot{\varepsilon} \alpha d^{-2}$). However, this is not true in the present study of W-

4.0Re-0.26HfC. As shown in Fig. 4.10, the creep stress increment due to HfC particle decreases as the HfC particle size increases, which means that the steady state creep rate increases with increasing particle diameter. Thus, for this alloy, the creep model proposed by Ansell and Weertman may not be applicable. Actually, their model can not account for the creep behavior of many dispersion- and precipitation-hardened alloys, e.g., Ni-ThO_2 (n=40) [27], Ni-Cr-ThO_2 (10<n<25) [28], and Nimonic alloys (n=4~7) [29]. The experimental results of these alloys reveal that the stress-dependence of the creep rate may vary widely between different materials and structural conditions, which could not be explained by this model.

A recovery model for high temperature creep has been proposed by McLean and Hale [30], based on the view that, during creep, dislocation exist as a 3-dimensional network. Recovery is then considered to result in growth of the network. During primary creep the dislocation density increases; this implies that the rate of recovery can not catch up with the rate of strain-hardening, and thus causes the creep rate to decrease. As the mesh-size in the dislocation network decreases with increasing dislocation density the recovery accelerates, and eventually a stage is reached where there is a balance between recovery and strain-hardening, which gives a roughly constant distribution of mesh sizes in the network. Based upon the above model, Lagneborg [31] proposed a model for high-temperature creep in materials hardened by second-phase particles. In such a model the creep process is described as consecutive events of recovery and strain-hardening, where the recovery is the rate-controlling step. According to this model, the second-phase particles impede the growth of the mesh-size in the dislocation network, and hence recovery and creep-rate are slowed down. It was proposed that the decrease in the recovery rate was due to a decrease of the driving force for the recovery process and of the mobility of the climbing dislocations involve in the process. The following expression for the creep rate was derived:

$$\dot{\varepsilon} = K\sigma^3[(\sigma/\alpha\mu b) - z]^2$$

where σ is the applied stress, μ the shear modulus, b the Burgers vector, K and α are constants, and z is a measure of the retarding force from the second phase on the climbing dislocation during recovery. This equation predicts that for stresses just above the critical (threshold) stress, which is the stress that gives zero creep-rate, the stress exponents should be much higher than 5 and decrease with increasing stress. It appears that this equation is able to account for the observed increase of the stress sensitivity of the creep-rate with decreasing stress in ODS alloys [27,28,32-35]. On the other hand, precipitation-hardened materials in which coalescence of the particles can not be entirely disregarded, there will be time for some increase of the interparticle spacing due to coalesence and thus decreases z somewhat. This will diminish the stress sensitivity at low creep rates even so much that no deflection occurs in stress/creep rate relationship, and the stress exponent approaches to a constant equal to 5. This model seems to be able to account for the creep behavior of W-4Re-0.26HfC qualitatively. It appears that the HfC particles impede the generation of sources by network growth, thus reducing the steady state creep rate.

The above creep model for second-phase particle hardened materials proposed by Lagneborg was further modified by Lagneborg and Bergman [36], and Lagneborg [37]. In their theory, they applied the principle of recovery creep as well as a general climb mechanism to describe creep in precipitation-hardened alloys and derived a relationship of the type

$$\dot{\varepsilon} = A(\sigma-\sigma_p)^n$$

where A is a constant, σ_p a back stress due to the extra dislocation line length produced during bypassing the particles, and n the stress exponent. Owing to the fact that σ_p was constant at high stresses, where the back stress σ_p corresponds to the stress to operate a particle-cutting mechanism or the Orowan mechanism, and proportional to σ ($\sigma_p = K\sigma$, where K = 0.7) at low stresses

($\sigma<\sigma_{or}$, where σ_{or} is the Orowan stress), they predicted a stress exponent of 4 at low stresses and large stress exponents (typical within the range 5 - 15) at high stresses. At sufficiently low stresses dislocations can bypass the particles by surmounting them by a climb motion. This bypassing process can occur under a smaller opposing force from the particle than that required for a cutting mechanism or the Orowan mechanism. Accordingly, their theory can explain the pronounced break found in the stress/creep rate relationship of precipitation-hardened alloys[36,37]. Dislocation loops and pairs were never observed in the TEM examination of the creep-tested W-4Re-0.26HfC specimens, but only single dislocation bulging between the particles. Hence, the bypassing of dislocations over particles in this alloy appears to be a general climb mechanism, as suggested by Lagneborg. However, their theory can only qualitatively explain the experimental results of this study. Because, by using the calculated values for the back stress σ_p ($=K\sigma$, where K=0.7) of W-4Re-0.26HfC in this study, the value of n was found to be equal to about 5.2, which is not in agreement with that predicted by this model. This descrepency may be due to the over-estimated value of the back stress at low applied stresses for the precipitation-hardened alloys in this model. According to Arzt and Ashby [38], the threshold stress, σ_{th}, for general climb at low stresses is very small and can be expressed as

$$\sigma_{th}(\text{general}) \approx 0.04(Gb/l) \approx 0.05\ \sigma_{or}$$

where G is the shear modulus at the test temperatuere, b the Burgers vector, l the length of the climbing dislocation segment, and σ_{or} the Orowan stress which is given by $\sigma_{or} = CGb/l$ (C is a constant estimated at 0.84 [39]). While for local climb, they predicted the threshold stress as follows:

$$\sigma_{th}(\text{local}) \approx 0.3(Gb/l) \approx 0.36\ \sigma_{or}$$

Consequently, σ_{th} (local)/σ_{th} (general) $\approx$ 7.2. Since the values of G, b, and l can be either calculated or measured, the threshold stress σ_{th}(general) for W-4Re-0.26HfC at various temperatures can be obtained. It is interesting to see that by using the calculated values for σ_{th}(general) in W-4Re-0.26HfC, the value of n was found to be about 4.2, which is very close to the value proposed by Lagneborg and Bergman. After comparing the calculated values of σ_p and σ_{th}(general) for W-4Re-0.26HfC in this study, it was found that σ_p was about twice to ten times as large as σ_{th}(general), but was very close to the predicted value of σ_{th} (local). Therefore, it appears that the creep model of Lagneborg and Bergman is basically an extension of the localized climb model in the low particle volume fraction approximation, as pointed out by McClean [40].

Recently, Arzt and co-workers [41-43] studied the creep behavior of dispersion strengthened alloys and proposed a kinetic model for dislocation climb over hard particles with or without attractive particle-dislocation interactions [42,43]. In the case of no attractive particle-dislocation interaction [42], they did not assume the shape of the climbing dislocation in the vicinity of the particle. The only assumption concerning dislocation geometry they made was that the climbing dislocation segment was required to have constant chemical potential for vacancies along its length, i.e., the shape of climbing dislocation was given by a minimum energy condition. The resulting dislocation velocity was derived as:

$$v = 1/t_c = (Gb^4/d^3) \cdot C_i \cdot A \cdot [(\sigma-\sigma_{th})/\sigma_{or}]^n$$

where t_c = by-pass time for dislocation over particles

G = shear modulus

b = Burgers vector

d = width of the particle

C_i = a kinetic constant which for volume diffusion control is approximately equal to

$$C_v = 2\pi D_v d/K_B T b$$

If pipe diffusion from the neighboring particle is rate-limiting, then

$$C_p = a_p D_p/K_B T \lambda b$$

where D_v is the volume diffusivity, a_p the pipe cross sectional area ($\approx b^2$), D_p the pipe diffusivity, K_B the Boltzmann's constant, λ the interparticle spacing, and T the absolute temperature.

A = $60 \cdot 10^{-1.9ß}(d/h)^{1.6}$ where ß is the ramp angle of the particle and h the height of the particle.

σ = the applied stress

σ_{th} = the threshold stress for climb

σ_{or} = the Orowan stress

n = $3.5 \cdot ß^{0.3}(h/d)^{0.2}$

This model predicts quantitatively, the extent to which climb is localized near the particle. Localization increases with increasing stress but purely local climb, as suggested by Brown and Ham [44], is never obtained. A natural power-law dependence of the dislocation velocity on the applied stress, with n = 3 to 4, was obtained. This model also predicted a pronounced break in the stress/creep rate relationship of precipitation strengthened alloys, which on decreasing stress show a transition from (stress-sensitive) particle cutting or Orowan looping to (less stress-dependent) climb. This conclusion confirms the theory of Lagneborg and Bergman, as discussed previously. However, contrary to the relatively high threshold stress that Lagneborg and Bergman proposed, they predicted a small threshold stress for equilibrium climb and thus concluded that low volume fractions of small non-interacting particles were incapable of producing significant threshold stresses at high temperatures. It can be seen that predictions of this model are hard to compare to the measured creep data of W-4.0Re-0.26HfC, because the translation of dislocation velocities into creep rates requires quantitative knowledge of the mobile dislocation density, which is not available in the present study. However, from the predicted value of the stress exponent (for dislocation velocity) and the magnitude of the threshold stress, it appears that this model can qualitatively account for the creep behavior of W-4.0Re-0.26HfC.

From the above discussions it can be concluded that HfC particles impede the motion of dislocations and the rate-controlling deformation mechanism of creep in W-4Re-0.26HfC alloy appears to be climb of dislocations over HfC particles. The climb of dislocations over HfC particles agrees with the general climb model suggested by Lagneborg [37]. However, the back stress for dislocation climb over particles suggested by Lagneborg was too high to explain the experimental results obtained in this study. On the other hand, the threshold stress for dislocation climb predicted by Arzt and Ashby [38] and Rosler and Arzt [42] can explain the results of this study. In conclusion, the experimental results of the W-4Re-0.26HfC alloy can be explained qualitatively by any of the following models: (a) model of dislocation climb over non-interacting hard particles proposed by Arzt and coworkers, (b) Lagneborg's recovery creep model, and (c) the recovery creep and dislocation climb model of Lagneborg and Bergman. However, the climb-controlled glide model of Weertman, the screw dislocation glide model, or the model of Ansell and Weertman can not account for the experimental results of this study.

(B) W-3.6Re-1ThO_2

The resulting creep data of this alloy is shown in Table 3.4. Fig. 28 shows the typical step-load strain-time creep curves of this alloy tested at various temperatures.

3.3.2.5 The Effect of Stress on Steady-State Creep Rate

Fig. 29 shows the stress-dependence of steady-state creep rate of this alloy at temperatures ranging from 2040 to 2500 K. It also shows a power-law relationship between creep stress and steady-state creep rate. The stress exponents of creep deformation at various temperatures range from 4.6 to 4.7, and are insensitive to the temperature. They are slightly lower than those obtained for W-4Re-0.26HfC alloy.

The average value of the stress exponent is 4.6.

3.3.2.6 The Effect of Temperature on Steady-State Creep Rate

Fig. 30 shows the temperature-dependence of steady-state creep rate at various applied stress (ranging from 21 to 45 MPa). The creep activation energy of this alloy can be obtained by measuring the slope of each curve. It also turn out that the creep activation energy vary with temperature for this alloy. At temperatures range from 2040 to 2200 K, the creep activation energies range from 102 to 108 Kcal/mol with an average value of 105.8 Kcal/mol. While at temperatures from 2300 to 2500 K, the average creep activation energy is 152.8 Kcal/mol. Comparing with the values obtained for W-4Re-0.26HfC, it appears that these two alloys have the same rate-controlling creep deformation mechanism either at lower temperature or higher temperature range. The rate-controlling deformation mechanism at temperatures between 2040 and 2200 K is most likely to be diffusion controlled dislocation climb, as in the case of W-4Re-0.26HfC. While at temperatures between 2300 and 2500 K the rate-controlling deformation mechanism seems to be lattice self-diffusion.

3.3.2.7 Microstructure characterizations

Figs. 31 and 32 show the as-swaged microstructures of this alloy observed in optical and scanning electron microscope, respectively. They show the band structure elongated in the direction of the swaging axis. Voids can be found in the interfaces between ThO_2 particles and matrix. Since this alloy is a P/M alloy numerous tiny pores can be observed throughout the material. Figs. 33 to 36 show the optical microstructures of the side surface of the specimens tested at temperatures from 2100 to 2400 K. The grain size of the alloy after creep test can be measured by the linear intercept method. It was found that the average grain size of the creep tested specimen increase slowly from 70 micrometers to 110 micrometers as testing temperature increase from 2100 K to 2500 K. Therefore, from this result it is clear that thoria particles are very effective in retarding grain growth in this alloy. After examining the these micrographs carefully, it was found that intergranular cracks occurred on grain boundaries, which were perpendicular to the stress axis. The formation of these r-type cracks is due to the initiation and growth of voids on the grain boundaries. Voids nucleate on the grain boundaries due to the presence of the thoria particles. These voids grow and cluster together by the aid of grain boundary sliding and thus form the r-type cracks, which cause the eventual fracture of the material. Fig. 37 shows clearly the r-type cracks found in the specimen creep tested at 2040 K. Typical SEM fractographs of this alloy were shown in Figs. 38. It shows the typical intergranular fracture mode for this alloy after creep tested at the elevated temperature, as in the case of W-4Re-0.26HfC alloy. It can also be seen that numerous voids accompanied with thoria particles are located in grain boundaries, which confirms that the formation of the void in grain boundary is due to the presence of thoria particles. The particle size of thoria range from less than 1 micrometer up to 5 micrometers.

Since the thoria particles and their clusters found in this alloy can be as large as 5 micrometers, representive thin foils for transmission electron microscope study were very difficult to prepare. This is because the thoria particles are tend to detach from the thin foil during either electropolishing or ion milling. The resulting thin foils are usually too thick to be examined in TEM. Fig. 39 is the typical transmission electron micrographs of the W-3.6Re-1ThO_2 creep specimen tested at 2100 K. It shows the dislocation networks observed in this specimen. Compared with the dislocation networks found in the W-4Re-0.26HfC specimen, it appears that less dislocation networks formed in W-3.6Re-1ThO_2 alloy. It also shows that some dislocations were pinned by thoria particles. However, the interaction between dislocations and thoria particles is not so strong as that between dislocations and hafnium carbide particles.

3.3.2.8 Creep Strength at a creep rate of 10^{-6}/sec

Fig. 40 compares the creep strength of this alloy with W-4Re-0.26HfC, pure tungsten [45], W-5Re [12], and W-23.4Re-0.27Hf-C [3] alloys at a creep rate of 10^{-6}/sec. The strengthening effect of HfC and ThO_2 particles is obvious. It appears that below about 2250 K, W-4Re-0.26HfC has the highest creep strength. However, as temperature is raised above 2250 K, W-3.6Re-1ThO_2 has higher creep strength than W-4Re-0.26HfC.

From the above TEM micrograph study, it is clear that the high creep strength of W-4Re-0.26HfC is associated with the presence of the hafnium carbide particles and the formation of subgrains containing dislocation networks. It appears that fine HfC particles retard the movements of dislocations , subgrain boundaries and grain boundaries. However, as temperature exceeds 2200 K, HfC particles coarsened rapidly, and they can no longer retard the movement of dislocations effectively. Therefore, the creep strength of this alloy decrease rapidly as temperature exceeds 2200 K. On the other hand, in the case of W-3.6Re-1ThO_2 alloy, the high creep strength is of course associated with the presence of the thoria particles. Since the thoria particles can effectively retard the grain growth at temperature as high as 2500 K, W-3.6Re-1ThO_2 has higher creep strength than W-4Re-0.26HfC at temperatures above 2250 K.

3.3.3 Conclusions

1. The stress exponent for the steady-state creep of the W-4Re-0.26HfC alloy is shown to be 5.2, and is not sensitive to the test temperature from 1955 to 2500 K.

2. At temperatures from 1955 to 2190 K, the activation energy for creep deformation is about 105.5 Kcal/mol for W-4Re-0.26HfC. However, the activation energy for creep increased to 161.9 Kcal/mol at temperatures from 2300 to 2500 K.

3. Subgrains were formed in W-4Re-0.26HfC alloy during creep testing at 1955 to 2500 K. At temperatures from 1955 to 2190 K dislocation networks form the subgrain boundaries. At temperatures above 2300 K dislocation networks were rarely seen.

4. The size of HfC particles were measured to range from 100 to 900 A after creep tests at temperatures from 1955 to 2190 K. HfC particle coarsened rapidly at temperatures higher than 2200 K. Their particle size range from 500 to 5000 A at temperatures from 2300 to 2500 K.

5. From the creep data and TEM micrographs examination, the creep deformation mechanism for W-4Re-0.26HfC appears most likely to be diffusion controlled dislocation climb over the HfC particles at temperatures from 1955 to 2190 K, while lattice self-diffusion is the rate-controlling creep mechanism at temperatures above 2300 K.

6. The stress exponent for the steady-state creep of the W-3.6Re-1ThO_2 is 4.6, and is also insensitive to the test temperature from 2040 to 2500 K.

7. The activation energy for creep deformation of W-3.6Re-1ThO_2 is about 105.8 Kcal/mol. at temperatures from 2040 to 2200 K, and is about 152.8 Kcal/mol. at temperatures from 2300 to 2500 K.

8. The rate-controlling deformation mechanism of W-3.6Re-1ThO_2 at temperatures between 2040 and 2200 K is most likely to be diffusion controlled dislocation climb. While at temperatures above 2300 K the rate-controlling deformation mechanism seems to be lattice self-diffusion, as in the case of W-4Re-0.26HfC.

9. Failure mode of these two alloys is intergranular fracture. The intergranular fracture of W-4Re-0.26HfC is caused by wedge-shaped and irregular-shaped cracks, while the intergranular fracture of W-3.6Re-1ThO_2 is caused by r-type cracks.

10. Both HfC and ThO_2 particles are very effective in strengthening W-Re alloys. Both W-4Re-0.26HfC and W-3.6Re-1ThO_2 are more creep resistant than pure tungsten, W-5Re, and W-23.4Re-0.27Hf-C at temperatures above 0.5 T_m. However, at temperatures below 2250 K W-4Re-0.26HfC is more creep resistant than W-3.6Re-1ThO_2 due to the pinning effect of HfC particles on dislocations, subgrain boundaries, and grain boundaries. While, at temperatures above 2250 K, W-3.6Re-1ThO_2 has higher creep strength than W-4Re-0.26HfC due to the rapid coarsening of HfC particles.

References

1. W.D. Klopp and W.R. Witzke, "Mechanical Properties of Arc-Melted Tungsten-Hafnium-Carbon Alloys," NASA Tech. Note D-5348, Cleveland, Ohio, 1969.

2. W.R. Witzke, "The Effect of Composition on Mechanical Properties of W-4Re-Hf-C Alloys," Metall. Trans., **5**, (1974) 499-504.

3. W.D. Klopp and W.R. Witzke, "Mechanical Properties of a Tungsten-23.4 Percent Rhenium-0.27 Percent Hafnium-Carbon Alloy," J. Less-Common Metals, **24**,(1971) 427-443.

4. J.F. Morris, "Decreased Creep for Increased Space Power," Engineering Fracture Mechanics, **24**,(1986) 77-95.

5. J.F. Morris and D.L. Jacobson, "Materials Considerations for Ultrahigh-temperature Thermionic Conversion in Space Nuclear Power," 21st Intersociety Energy Conversion Engineering Conference (IECEC), Aug., 1985.

6. J.F. Morris and D.L. Jacobson, "Ultralloys for Nuclear Thermionic Conversion," 18th IECEC paper 839032, Aug., 1983.

7. M.C. Smith, D.M. Olson, and H.L. Brown, The Review of Scientific Instruments, **28**, (1957) 543.

8. J.L. Taylor, The Review of Scientific Instruments, **34**, (1963) 500.

9. H. Inouye, IEEE Conference record of 1969 thermionic conversion specialist conference, p. 425, 1969.

10. R.J. Buzzard, NASA Tech. Note D-6285, April, 1971.

11. S.L. Robinson and O.D. Sherby, "Mechanical Behavior of Polycrystalline Tungsten at Elevated Temperature," Acta Met., **17**, (1969) 109.

12. R.R. Vandervoort, "The creep Behavior of W-5Re," Metall. Trans., **1**, (1970) 857-864.

13. L.S. Rubenstein, "Effect of Composition and Heat Treatment on High-Temperature Strength of Arc-Melted Tungsten-Hafnium-Carbon Alloys," NASA Tech. Note D-4379, Cleveland, Ohio, 1968.

14. R.L. Orr, O.D. Sherby and J.E. Dorn, Trans. ASM, **46**, (1954) 113.

15. R.E. Pawel and T.S. Lundy, "Tracer Diffusion in Tungsten," Acta Met., **17**,(1969) 979.

16. R.L. Andelin, J.D. Knight and M. Kahn, "Diffusion of Tungsten and Rhenium Tracer in Tungsten," Trans. TMS-AIME, **233**,(1965) 19-24.

17. K.G. Kreider and G. Bruggeman, "Grain Boundary Diffusion in Tungsten," Trans. TMS-AIME, **239**, (1967) 1222-1226.

18. V.C. Nardone and J.K. Tien, "Pinning of Dislocations on the Departure Side of Strengthening Dispersoids," Scripta Metall., **17**, (1983) 467-470.

19. V.C. Nardone, D.E. Matejczyk, and J.K. Tien, "The Threshold Stress and Departure Side Pinning of Dislocations by Dispersoids," Acta Metall., **32**, (1984) 1509-1517.

20. J.H. Schroder and E. Arzt, "Weak Beam Studies of Dislocation/Dispersoid Interaction in an ODS Superalloy," Scripta Metall., **19**, (1985) 1129-1134.

21. R.S. Herrick, J.R. Weertman, R. Petkovic-Luton, and M.J. Luton, "Dislocation/Particle Interactions in an Oxide Dispersion Strengthened Alloy," Scripta Metall., **22**, (1988) 1879-1884.

22. J. Weertman, "Steady-State Creep through Dislocation Climb," J. Appl. Phys., **28** (1957) 362.

23. C. R. Barrett and W. D. Nix, "A Model for Steady State Creep based on the Motion of Jogged Screw Dislocations," Acta Met., **13** (1965) 1247.

24. N. F. Mott, "A Theory of Work-hardening of Metal Crystals," Phil. Mag., **25** (1952) 1151.

25. P. B. Hirsch and D. H. Warrington, "The Flow Stress of Aluminum and Copper at High Temperatures," Phil. Mag., **6** (1961) 735.

26. G. S. Ansell and J. Weertman, "Creep of a Dispersion-Hardened Aluminum Alloy," Trans. TMS-AIME, **215** (1958) 838.

27. B.A. Wilcox and A.H. Clauer, "Creep of Thoriated Nickel above and below 0.5 T_m," Trans TMS-AIME, **236** (1966) 570-580.

28. B. A. Wilcox, A. H. Clauer, and W. S. McCain, "Creep and Creep Fracture of a Ni-20Cr-2ThO_2 Alloy," Trans. TMS-AIME, **239** (1967) 1791.

29. W. Betteridge, "The Nimonic Alloys," Edward Arnold, London, 1959.

30. D. McLean and K. F. Hale, "Structural Process in Creep," p. 19, 1961:London (Iron Steel Inst.).

31. R. Lagneborg, "Recovery Creep in Materials Hardened by a Second Phase," J. of Materials Science, **3** (1968) 596.

32. R.W. Lund and W.D. Nix, "High Temperature Creep of Ni-20Cr-2ThO_2 Single Crystals," Acta Metall. **24**(1976) 469.

33. B.A. Wilcox and A.H. Clauer, "The Role of Grain Size and Shape in Strengthening of Dispersion Hardened Nickel Alloys," Acta Metall. **20**(1972) 743.

34. B. Russell, R. K. Ham, J. M. Silcock, and G. Willoughby, "Creep Mechanisms in Niobium-Stabilized Austenitic Steels," Metal Sci.J., **2** (1968) 201.

35. J. H. Hausselt and W. D. Nix, "A Model for High Temperature Deformation Dispersion Strengthened Metals Based on Substructural Observations in Ni-20Cr-2ThO_2," Acta Met., **25** (1977) 1491.

36. R. Lagneborg and B. Bergman, "The Stress/Creep Rate Behavior of Precipitation-Hardened Alloys," J. of Metal Science, **10** (1976) 20-28.

37. R. Lagneborg, "Bypassing of Dislocations Past Particles by a Climb Mechanism," Scripta Met., **7** (1973) 605.

38. E. Arzt and M.F. Ashby, "Threshold Stresses in Materials Containing Dispersed Particles," Scripta Met., **16**(1982)1285.

39. U.F. Kocks, Phil. Mag. **13**(1966) 541.

40. M. McLean, "On the Threshold Stress for Dislocation Creep in Particle Strengthened Alloys," Acta Met., **33** (1985) 545.

41. E. Arzt, J. Rosler and J.H. Schroder, "The Mechanism of Dispersion Strengthening in High Temperature Alloys," in Creep and Fracture of Engineering Materials and Structures, B. Wilshire and R.W. Evans ed., The Institute of Metals, London, (1987) 217.

42. J. Rosler and E. Arzt, "The Kinetics of Dislocation Climb over Hard Particles - I. Climb Without Attractive Particle-Dislocation Interaction," Acta Metall. **36**(1988) 1043.

43. E. Arzt and J. Rosler,"The Kinetics of Dislocation Climb over Hard Particles - II. Effects of an Attractive Particle-Dislocation Interaction," Acta Metall. **36**(1988) 1053.

44. L.M. Brown and R.K. Ham, in Strengthening Methods in Crystals (edited by A. Kelly and R.B. Nicolson), Elsevier, Amsterdam, (1971) 9.

45. R.R. Vandervoort and W.L. Barmore, "Elevated Temperature Deformation and Electron Microscope Studies of Polycrystalline Tungsten and Tungsten-Rhenium Alloys," Proc. 6th Plansee Seminar, Metallwerk Plansee Ag., Reutte-tyrol, pp. 108-137, 1969.

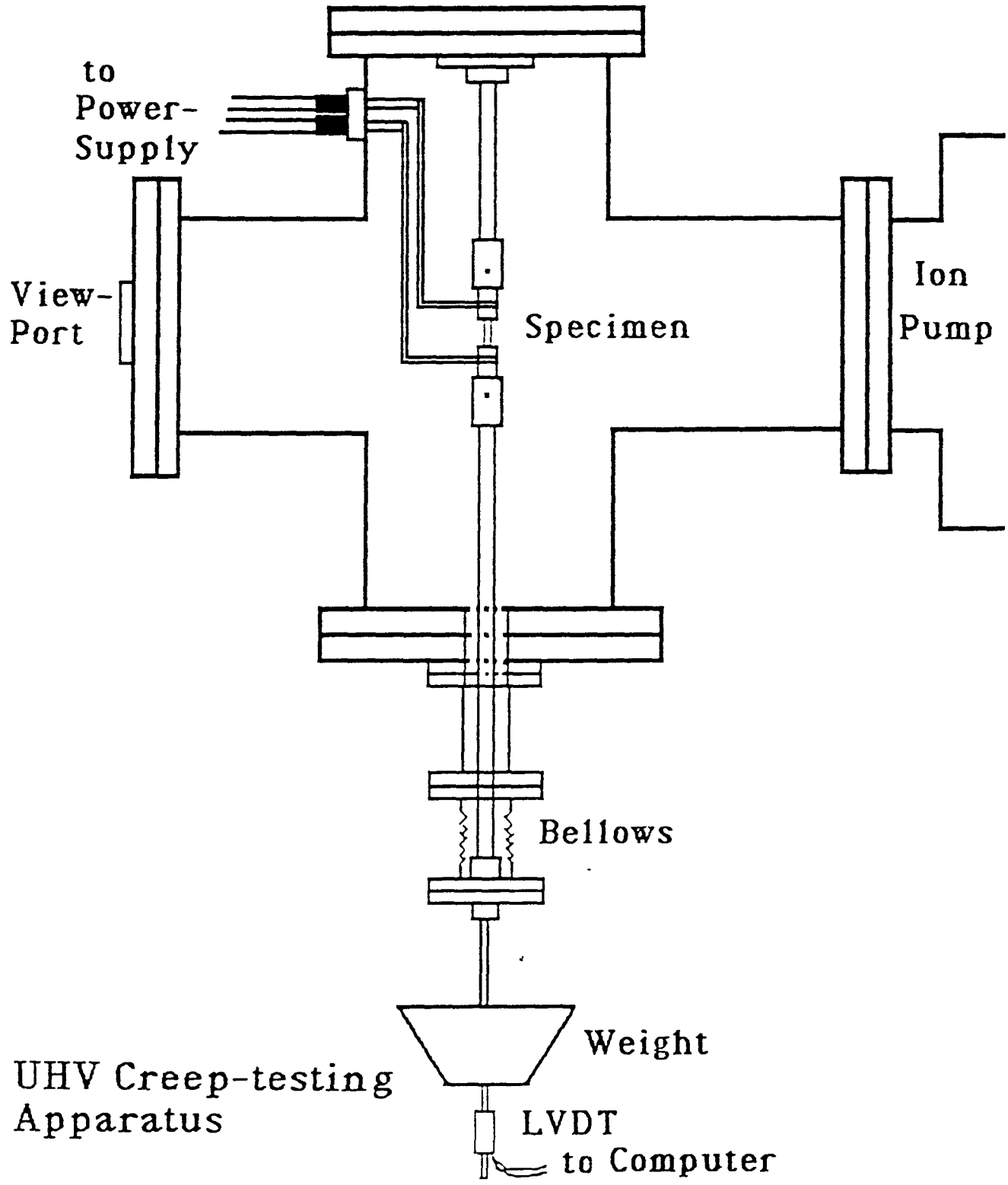

Fig. 3.1. Schematic diagram of the designed creep testing apparatus.

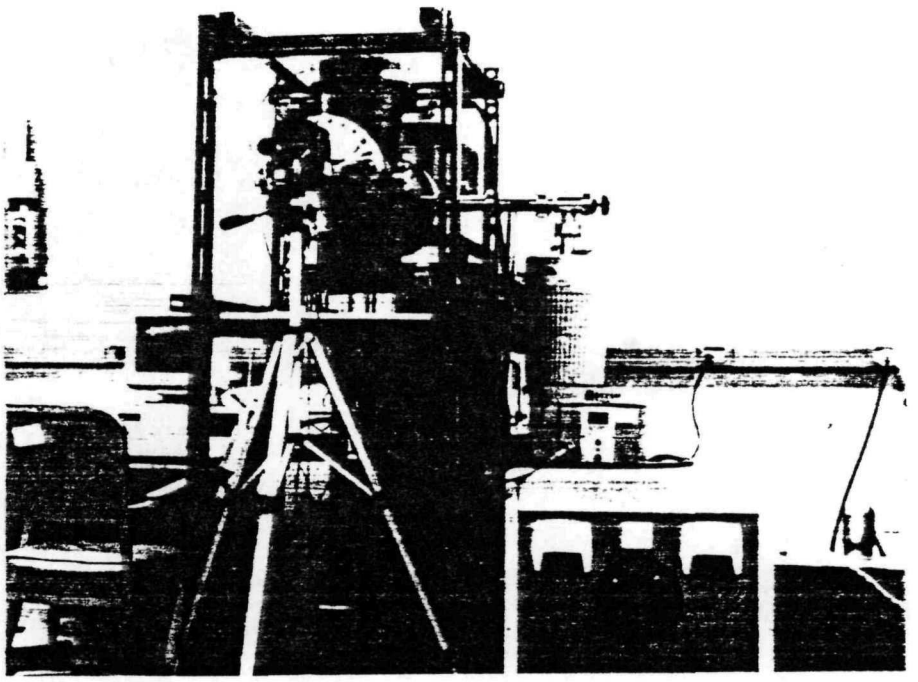

Fig. 3.2. The high temperature UHV creep testing system.

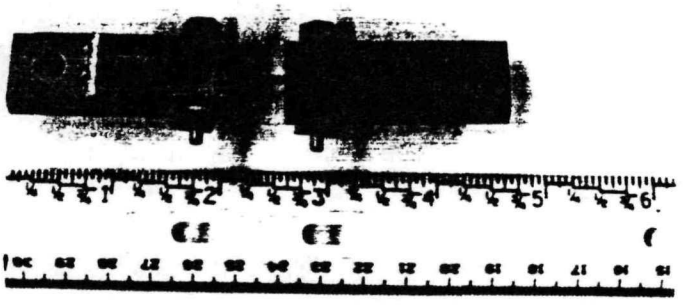

Fig. 3.3. The grips for testing plate-type creep specimens.

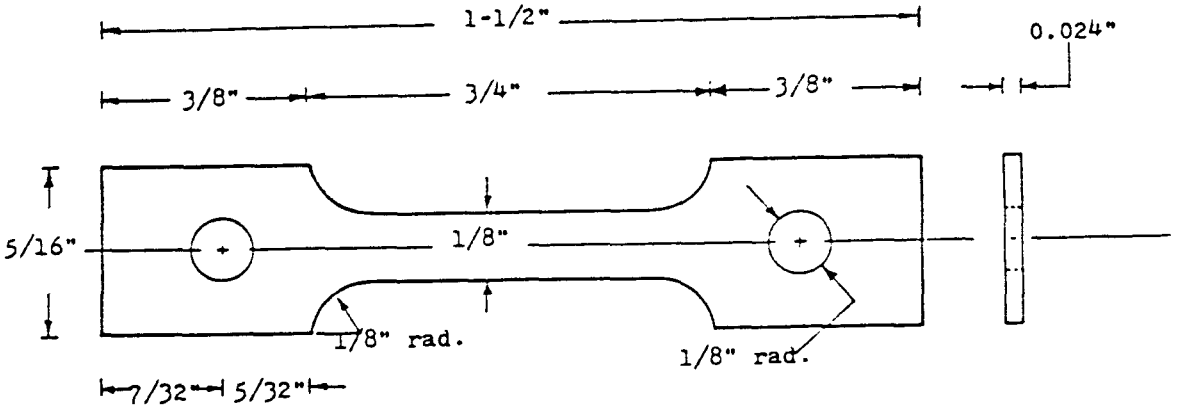

(a)

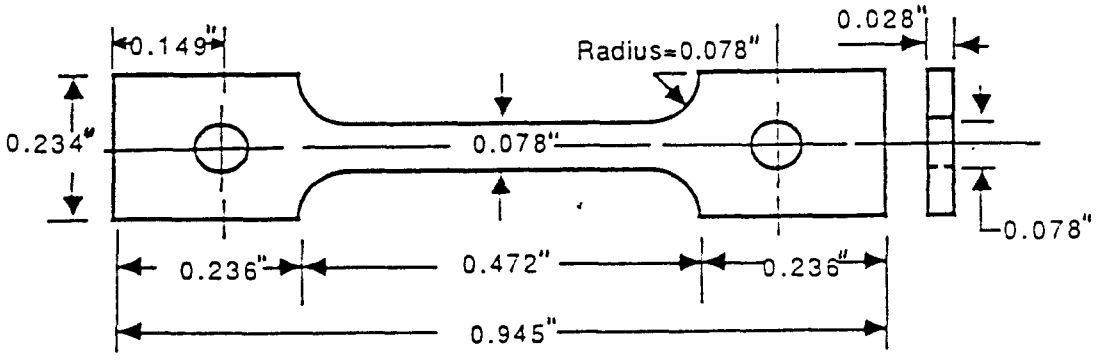

(b)

Fig. 3.4. The dimensions of the plate-type creep specimen of W alloys.

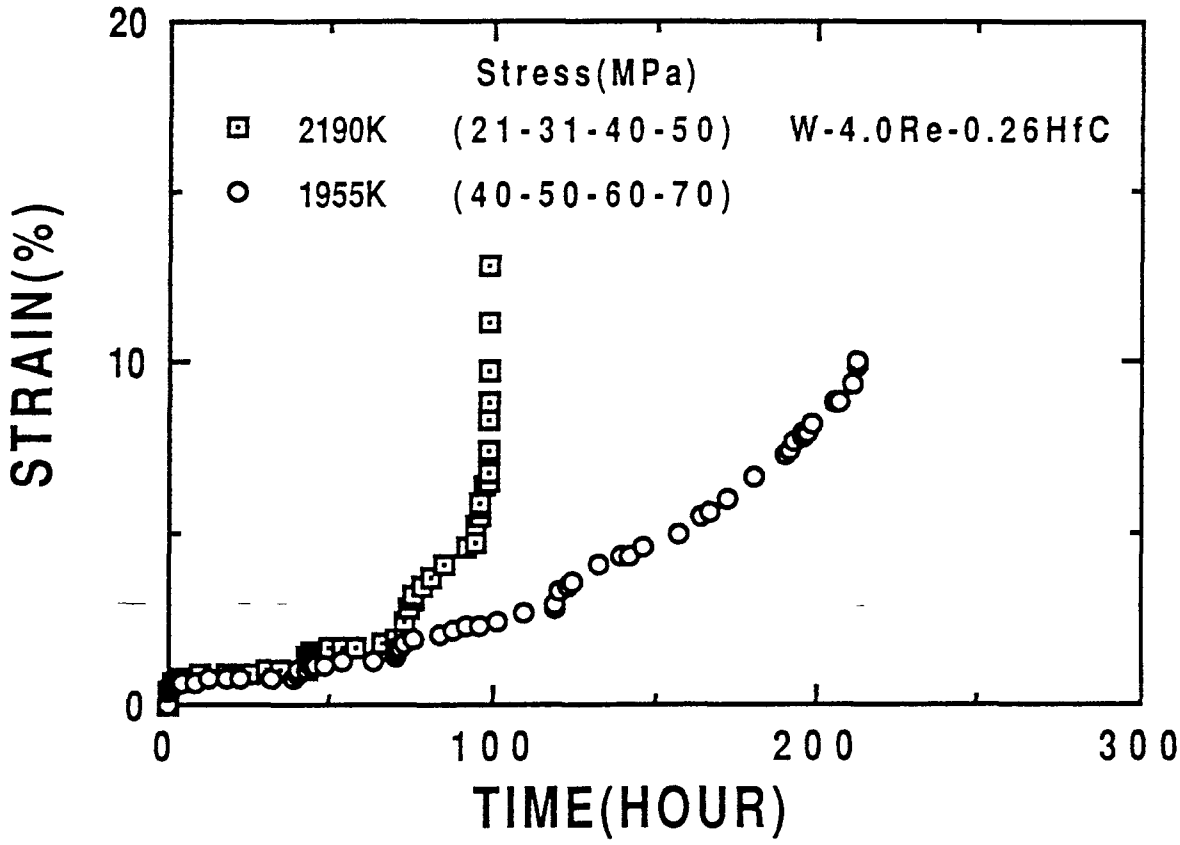

Fig. 3.5. Typical step-load strain-time creep curve of the W-4Re-0.26HfC alloy.

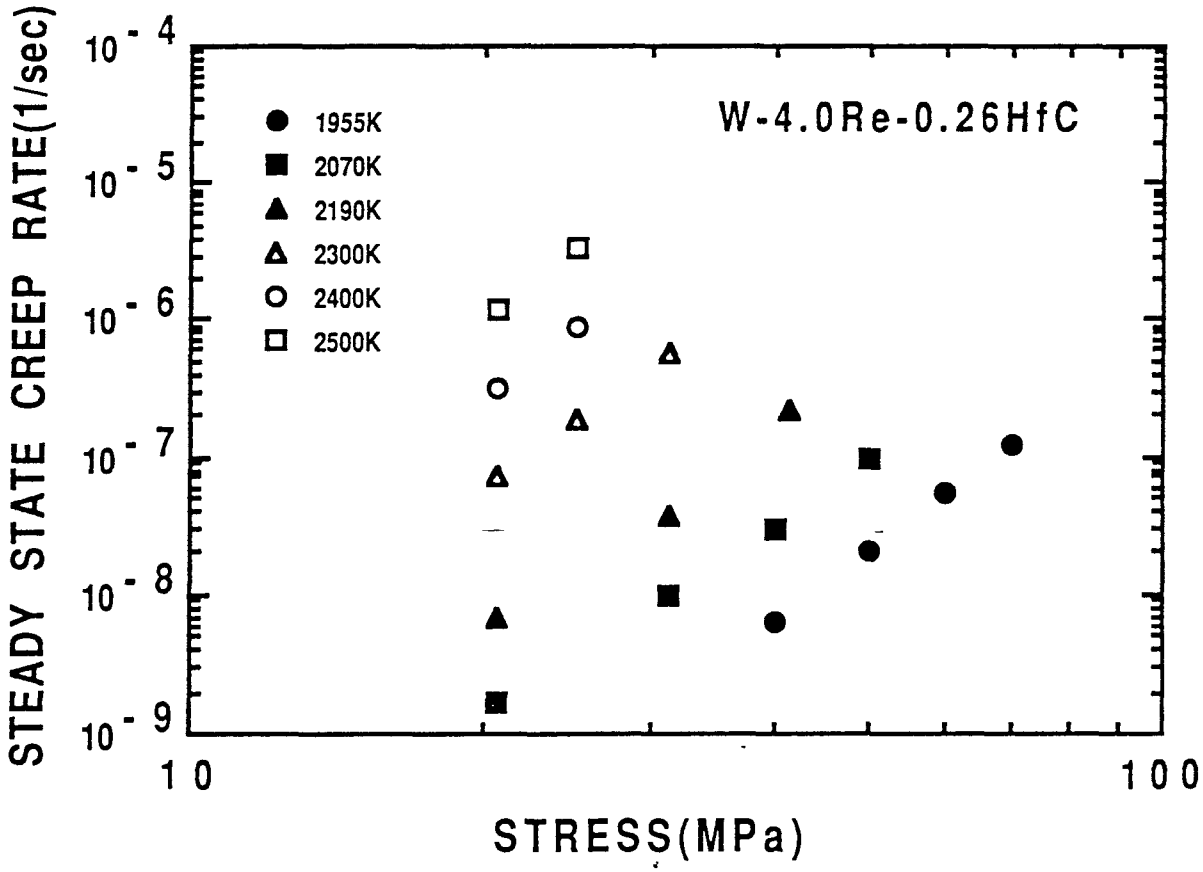

Fig. 3.6. Power-law relationship between steady-state creep rate and stress for W-4Re-0.26HfC.

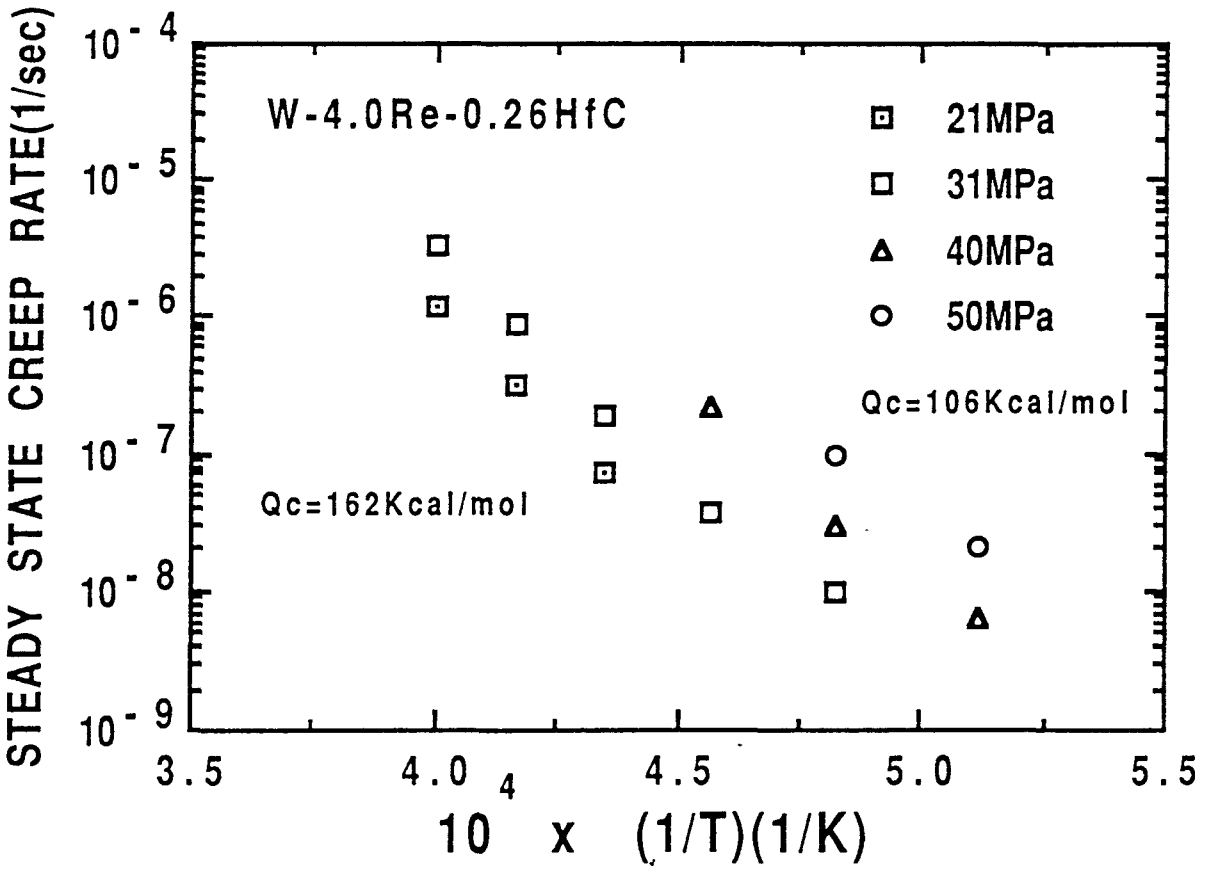

Fig. 3.7. Temperature-dependence of the steady-state crep rate for the W-4Re-0.26HfC alloy at various stresses.

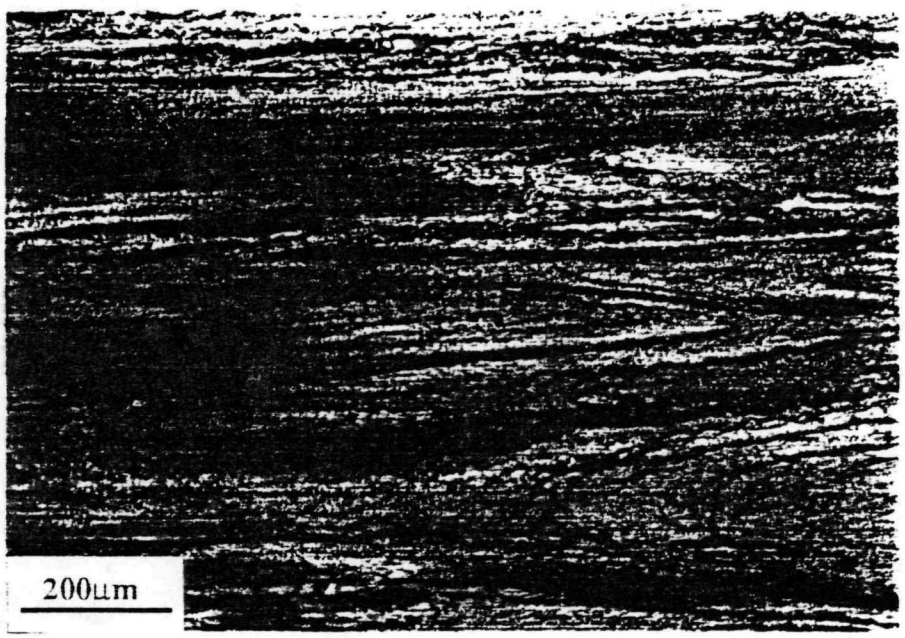

(a) as-swaged

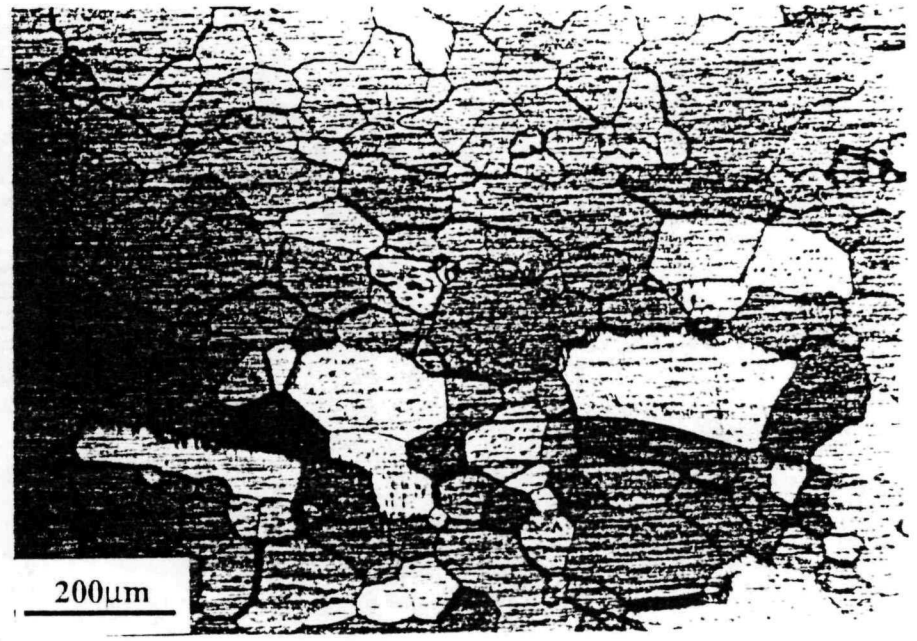

(b) recrystallized

Fig. 3.8. The (a) as-swaged and (b) recrystallized optical microstructures of W-4Re-0.26HfC.

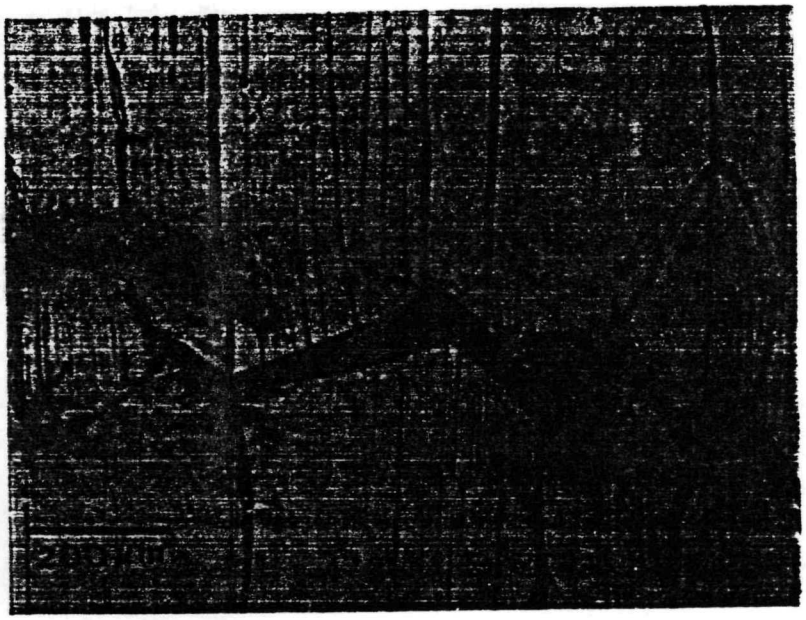

Fig. 3.9. Typical optical microstructure observed on the side surface of the W-4Re-0.26HfC crept specimen.

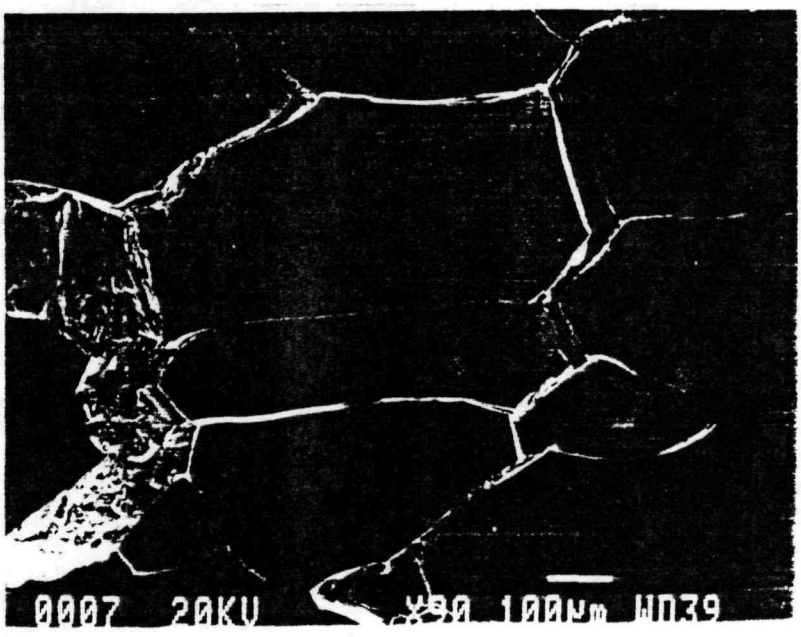

Fig. 3.10 Typical SEM micrograph observed on the side surface of the W-4Re-0.26HfC crept specimen.

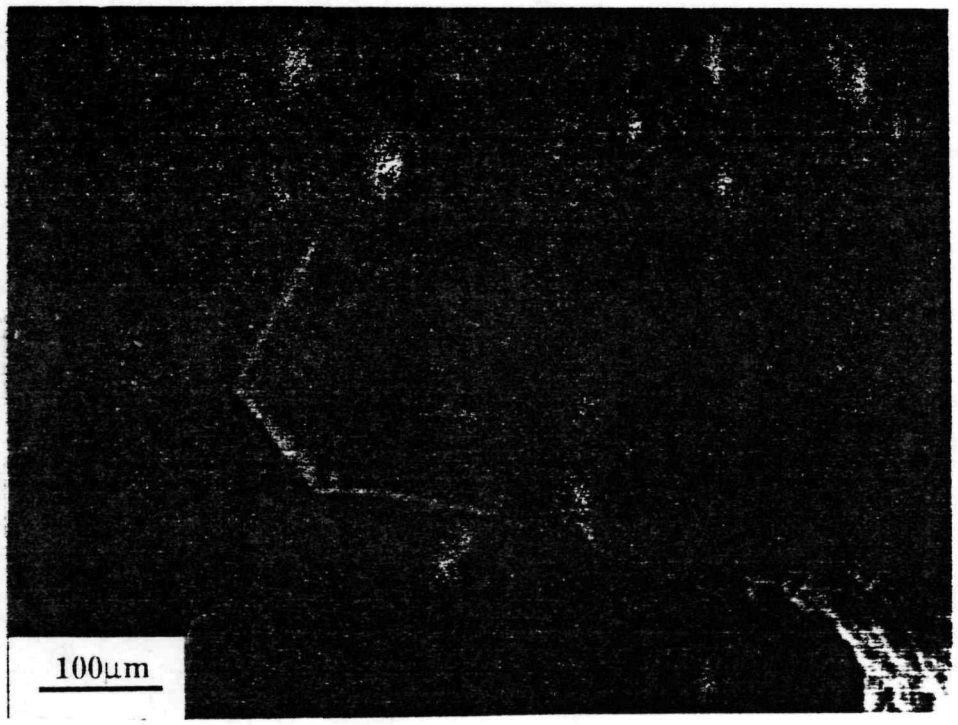

Fig. 3.11. Migration irregularities formed by grain boundary migration during creep.

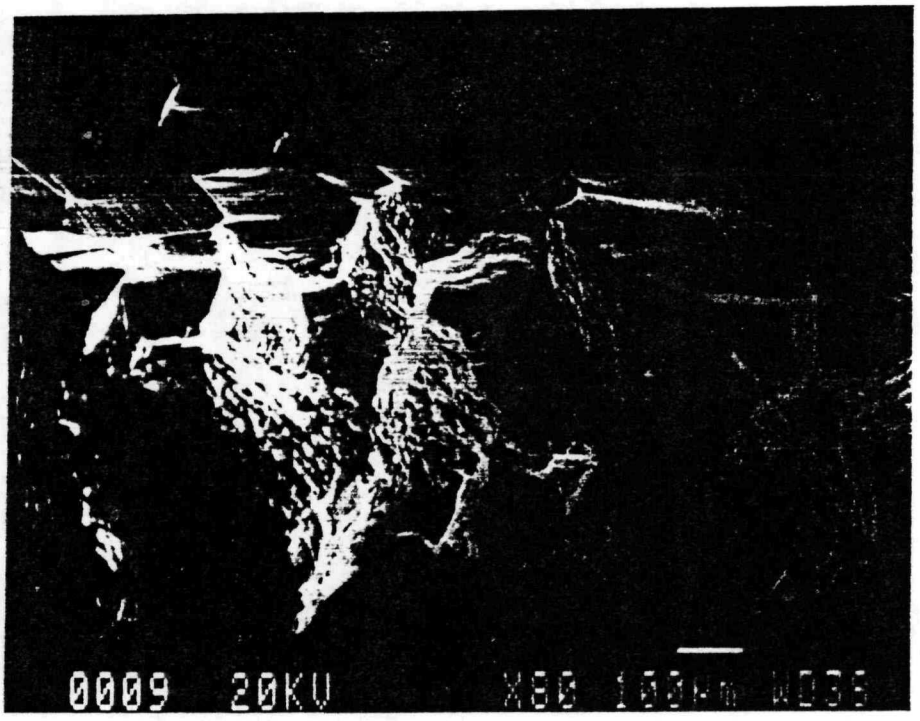

Fig. 3.12. SEM fractographs of the 2190 K creep tested sample of W-4Re-0.26HfC.

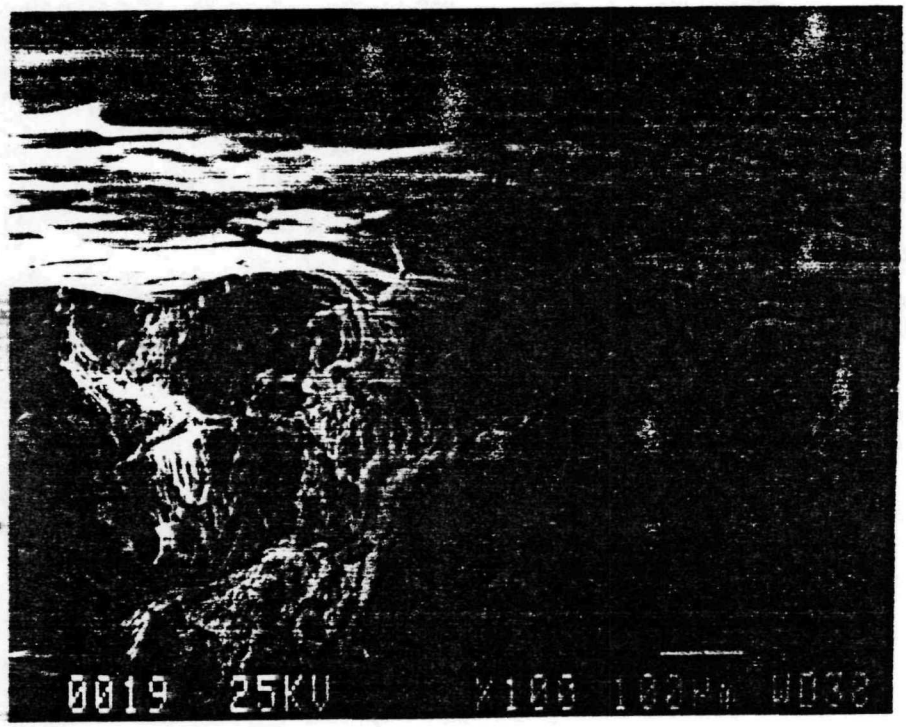

Fig. 3.13. SEM fractographs of the 2300 K creep tested sample of W-4Re-0.26HfC.

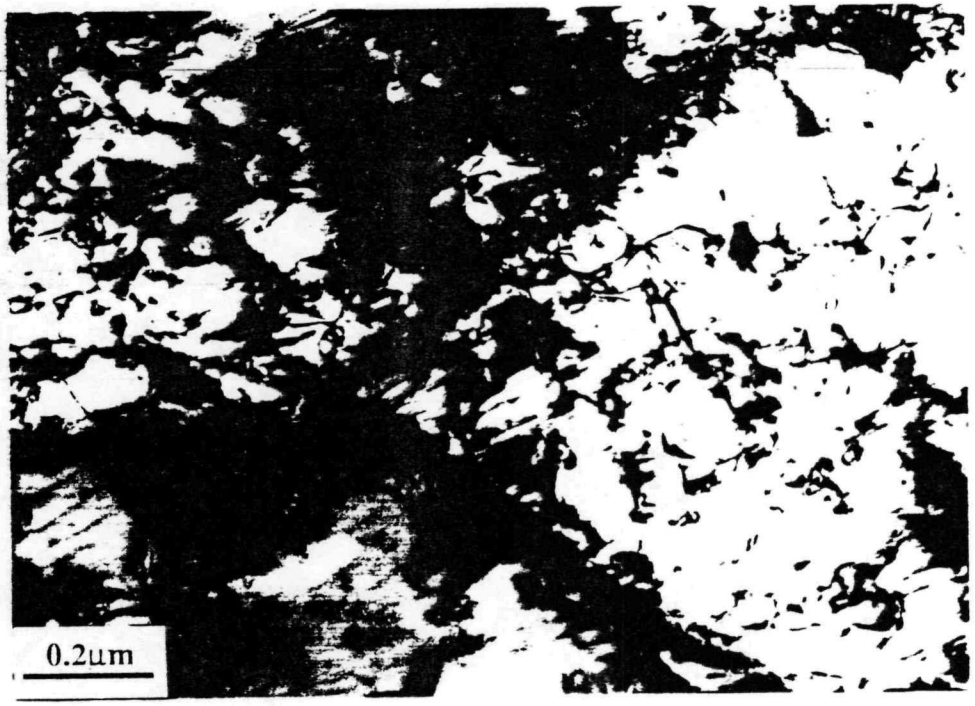

Fig. 3.14. Dislocation cell structure observed in the as-swaged W-4Re-0.26HfC alloy.

Fig. 3.15. Dislocation substructures observed in the 1955 K crept specimen.

Fig. 3.16. Individual dislocations were pinned by HfC particles in the 1955 K creep tested specimen.

Fig. 3.17. Numerous fine precipitates were formed in the 1955 K creep tested sample.

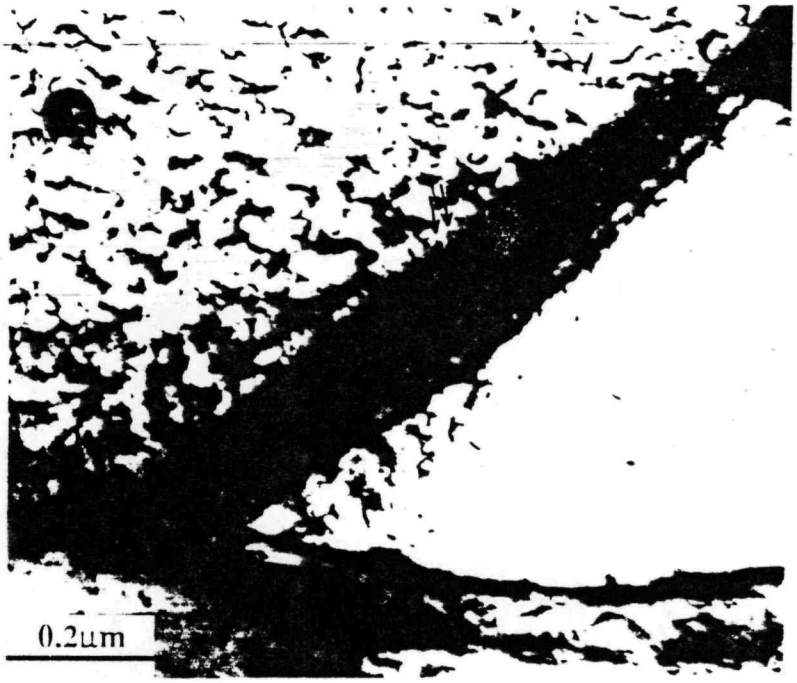

Fig. 3.18. Some HfC particles were located in the grain boundaries of the specimen tested at 2070 K. Periodic grain boundary dislocation arrays can be resolved in the grain boundary.

Fig. 3.19. The interaction between dislocations and HfC particles in the interior of the subgrain in the 2070 K creep tested sample. No Orowan looping was observed around the particles.

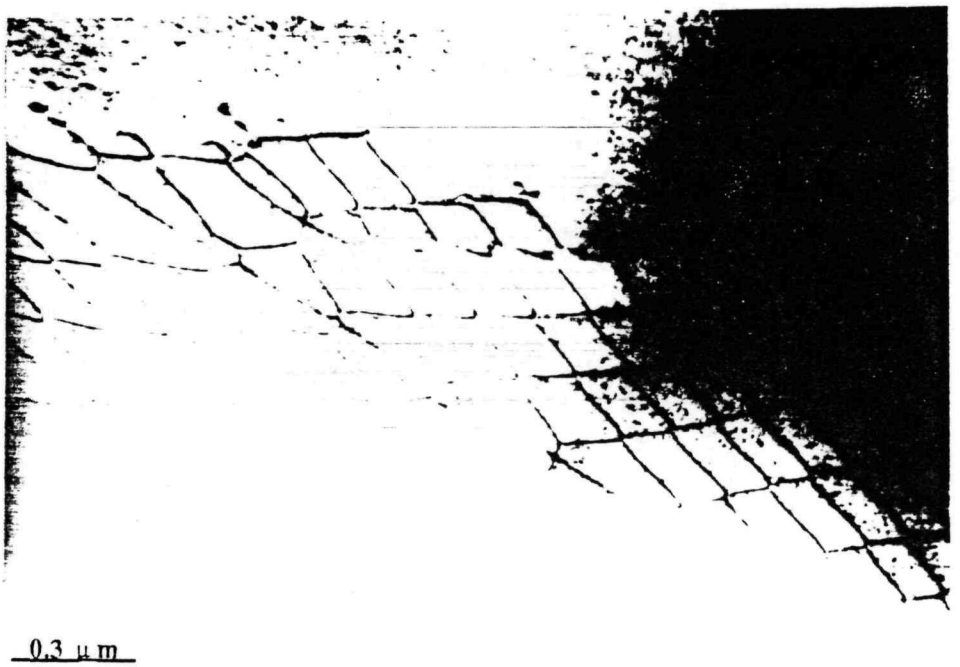

Fig. 3.20. The dislocation networks with two dislocation families formed in the 2190 K creep tested specimen.

Fig. 3.21. The hexagonal networks with three dislocation families formed in the 2190 K creep tested specimen.

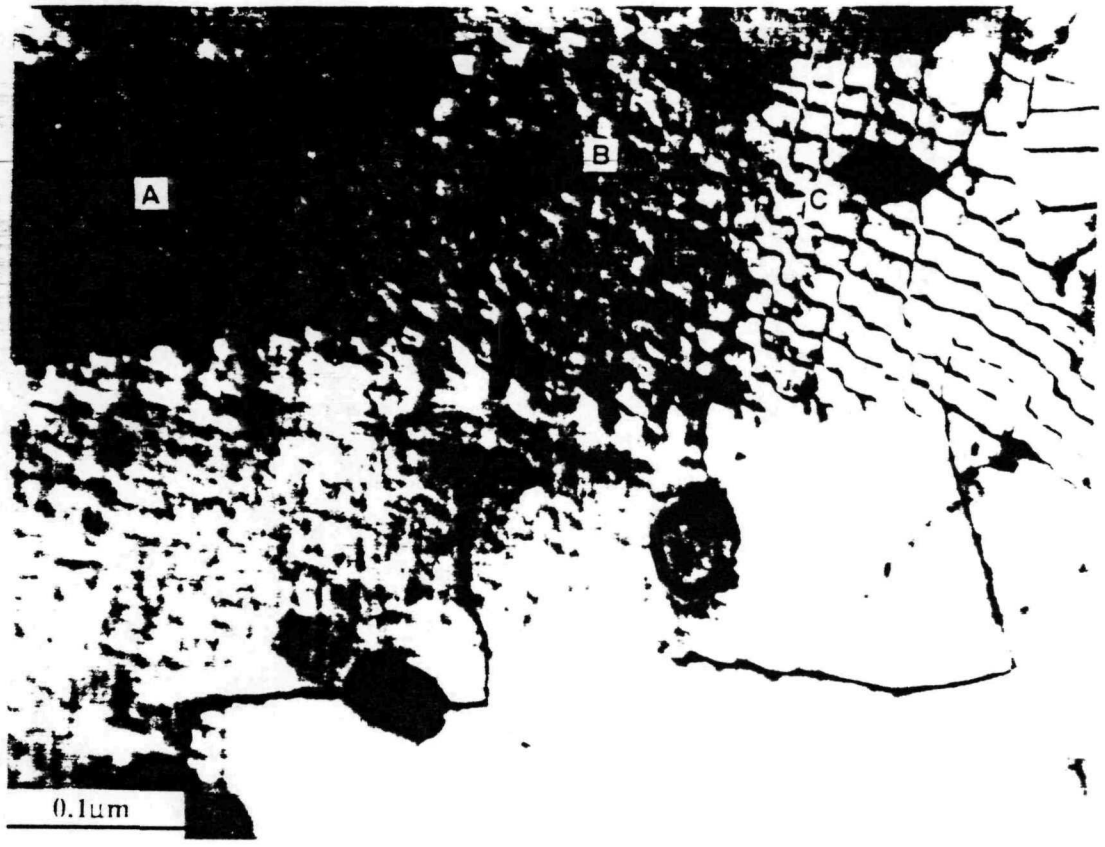

Fig. 3.22. Interaction between subgrain boundary dislocations and HfC particles. Dislocations in the networks are pinned by HfC particles (at A, B, and C).

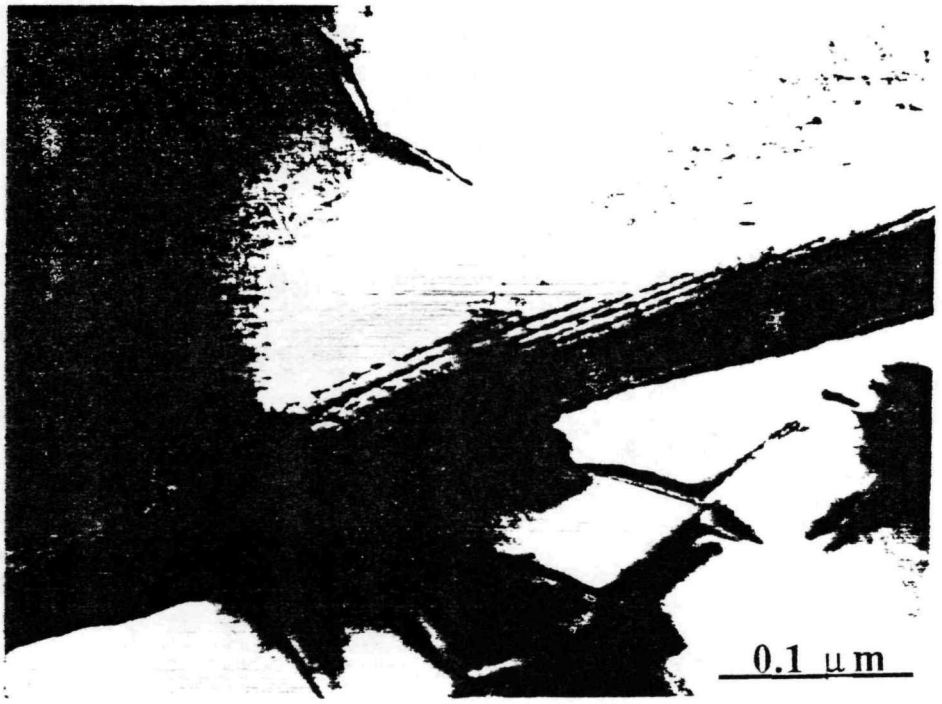

Fig. 3.23. Grain boundary migration found in the 2190 K creep tested sample.

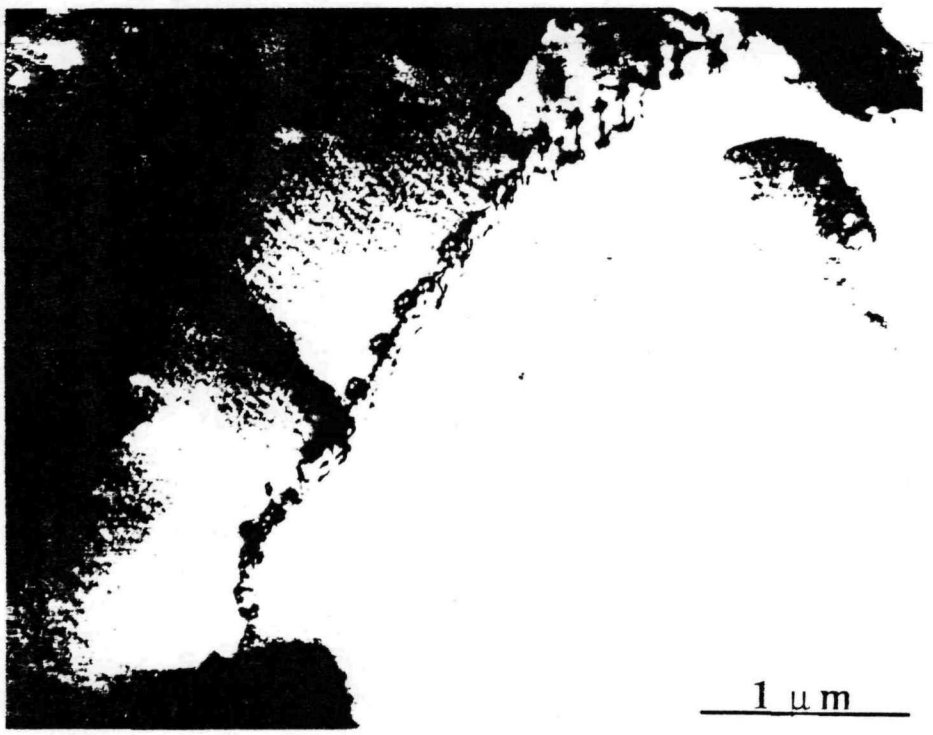

Fig. 3.24. Low-angle grain boundary found in the 2300 K creep tested samples.

Fig. 3.25. TEM micrographs of the specimen tested at 2300 K.

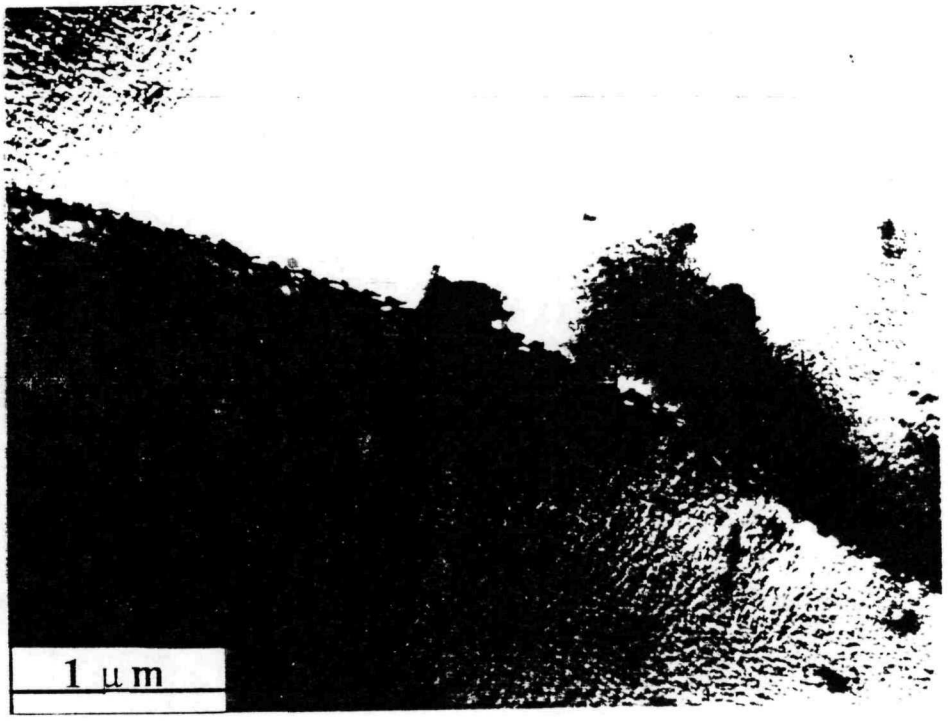

Fig. 3.26. TEM micrographs of the specimen tested at 2400 K.

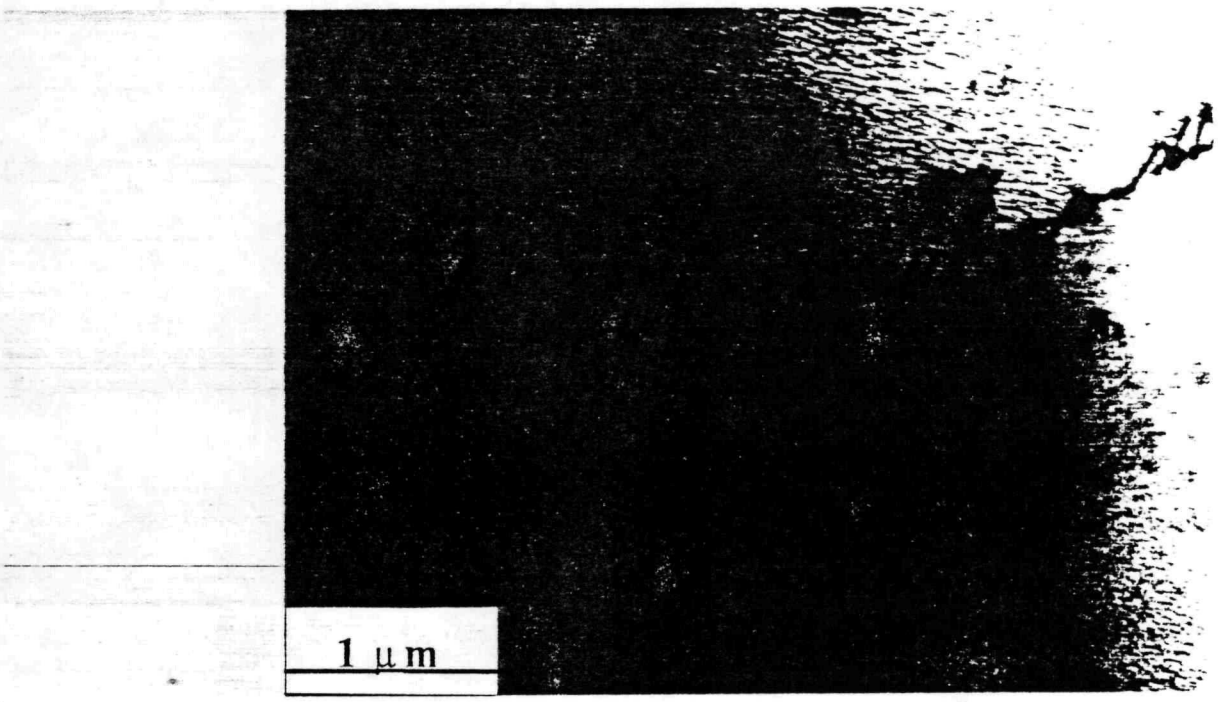

Fig. 3.27. TEM micrographs of the specimen tested at 2500 K.

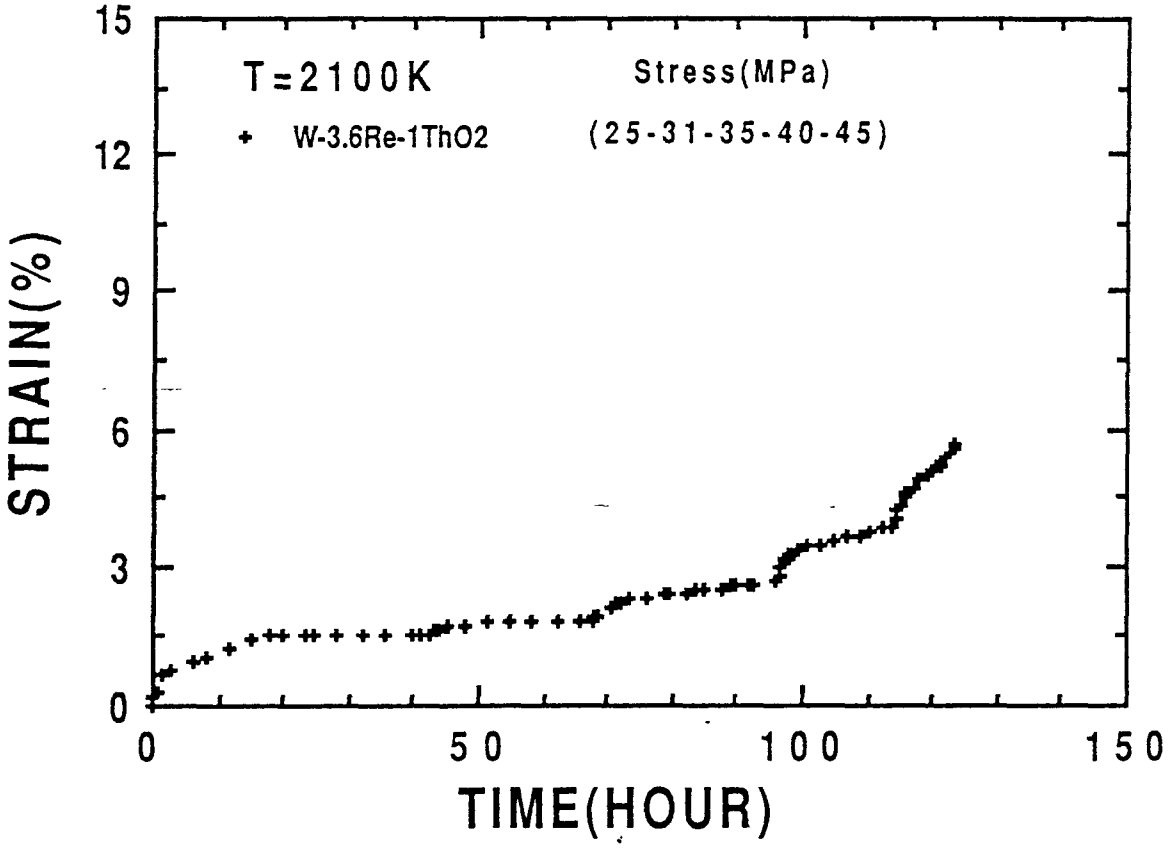

Fig. 3.28. Typical step-load strain-time creep curves of the W-3.6Re-1ThO_2 alloy.

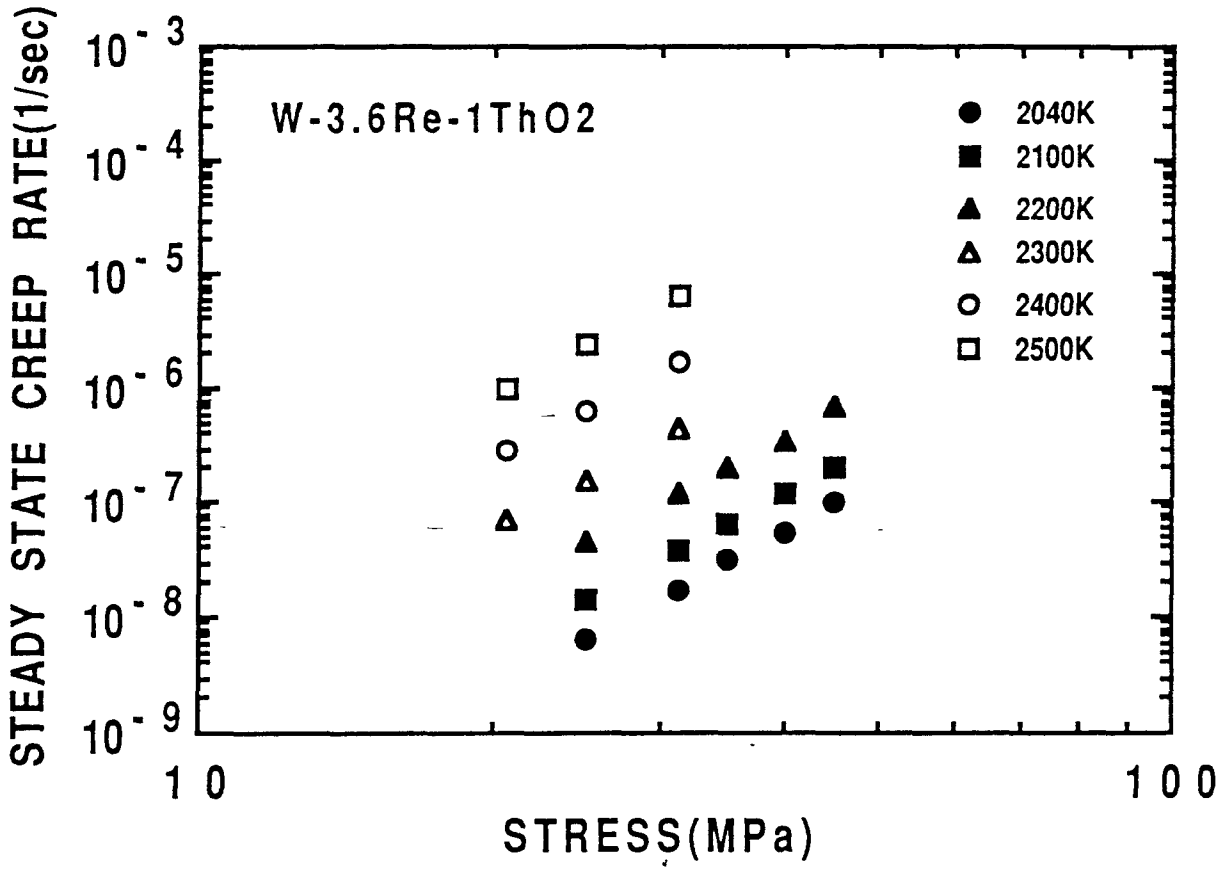

Fig. 3.29. Power-law relationship between the steady-state creep rate and creep stress in W-3.6Re-1ThO_2.

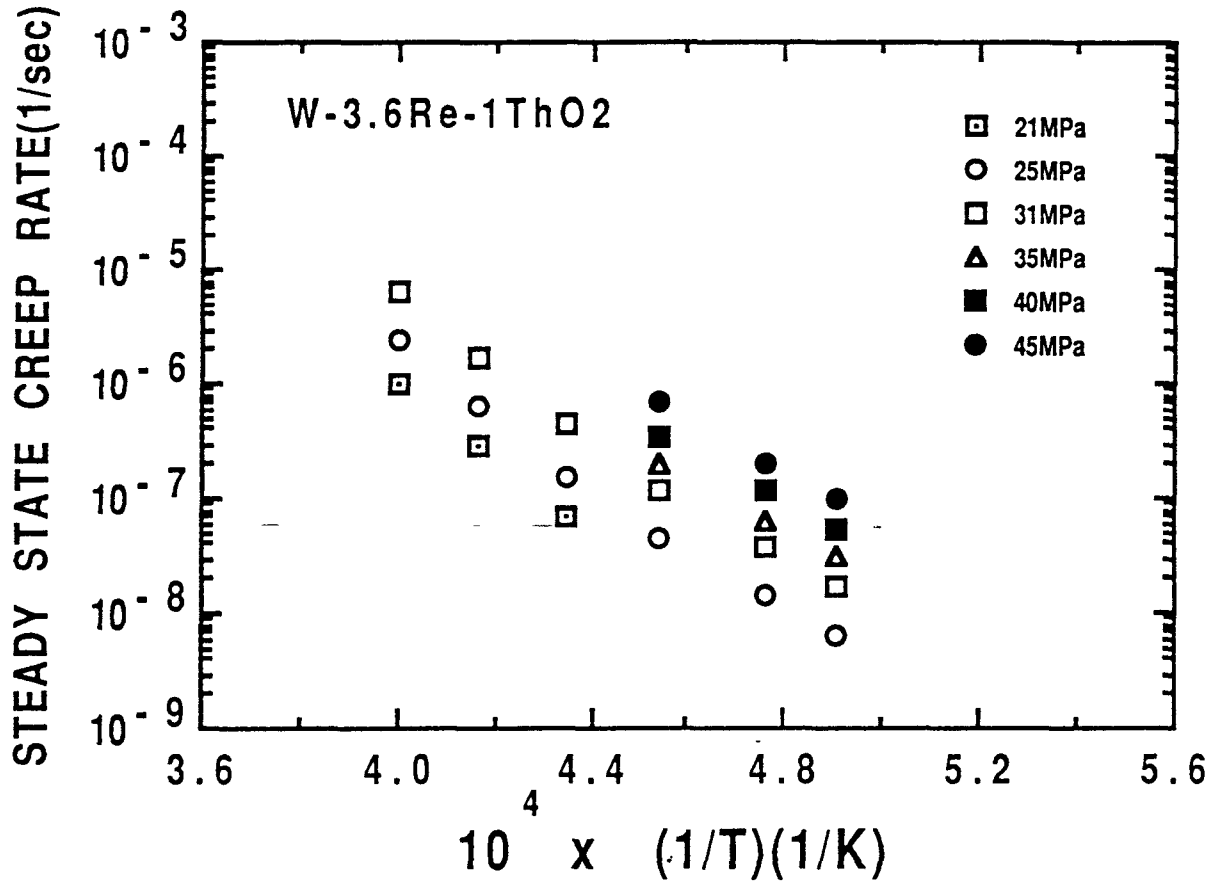

Fig. 3.30. Temperature-dependence of steady-state creep rate at various applied stress for W-3.6Re-1ThO_2.

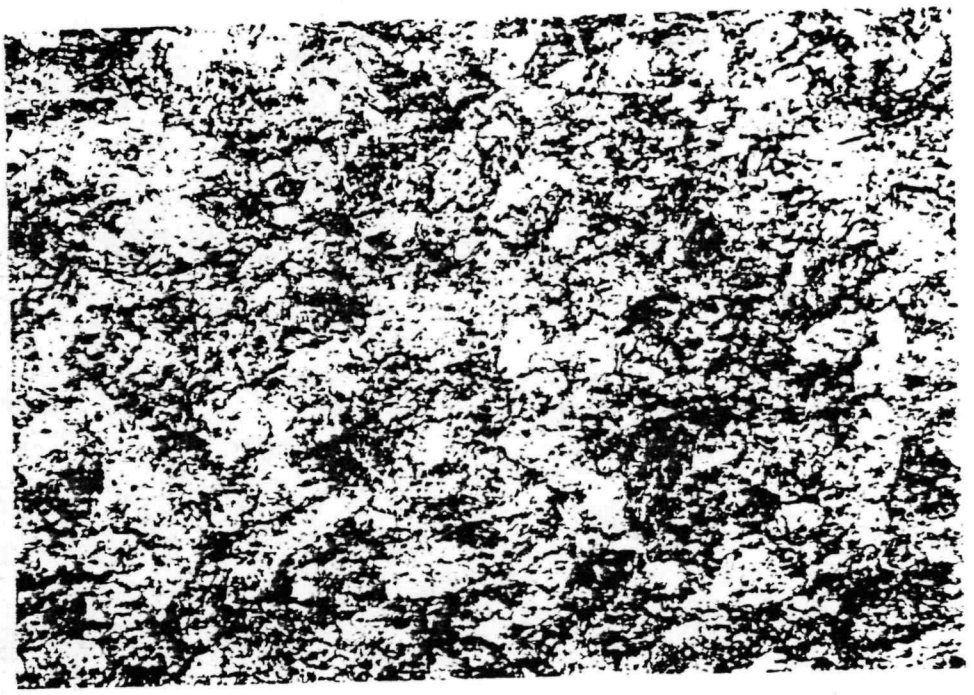

Fig. 3.31. The as-swaged optical microstructure of W-3.6Re-1ThO_2.

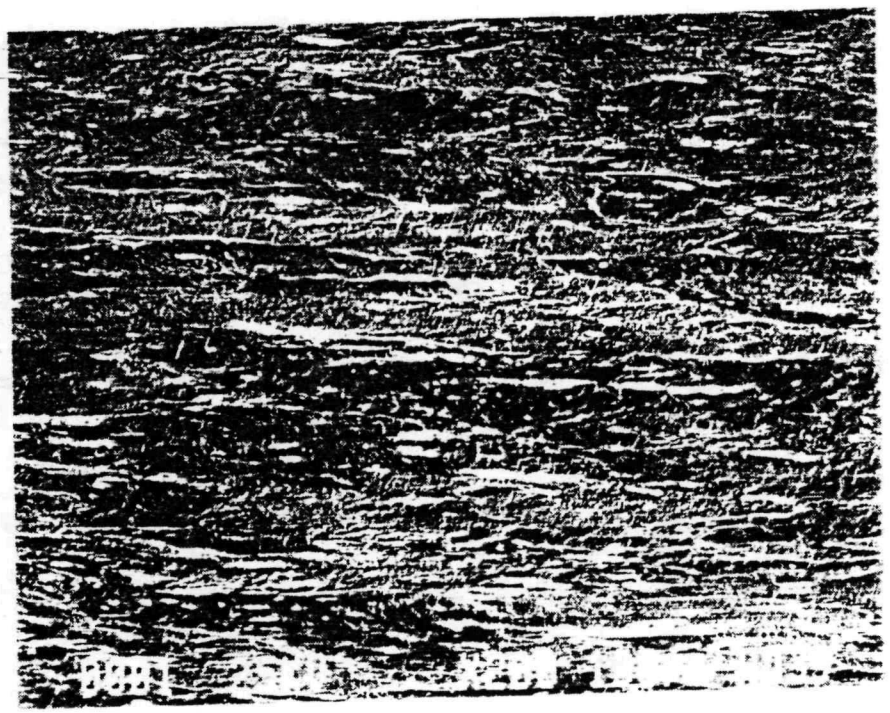

Fig. 3.32. The as-swaged SEM micrograph of W-3.6Re-1ThO_2.

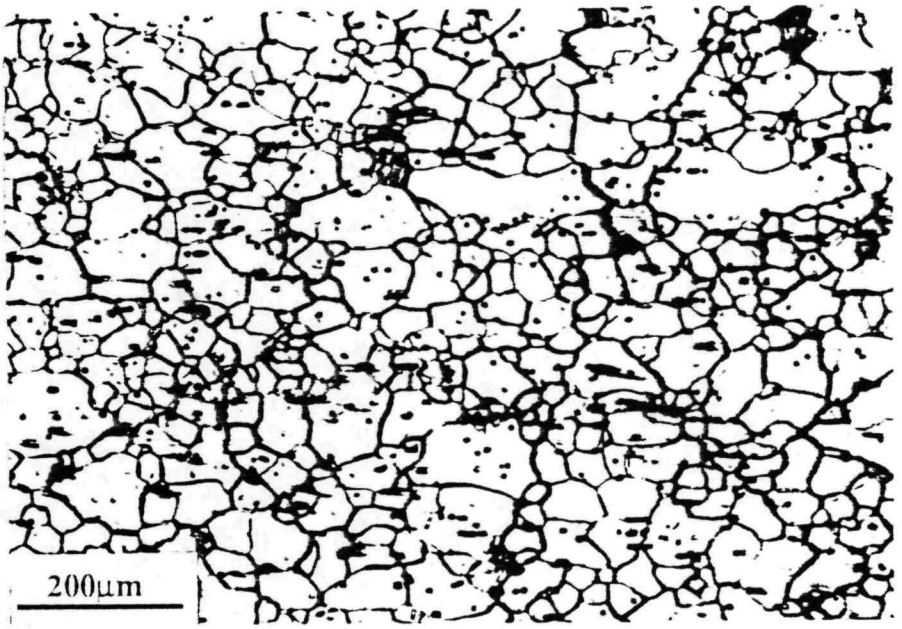

Fig. 3.33. The optical microstructure of the side surface of the specimen tested at 2100 K.

Fig. 3.34. The optical microstructure of the side surface of the specimen tested at 2200 K.

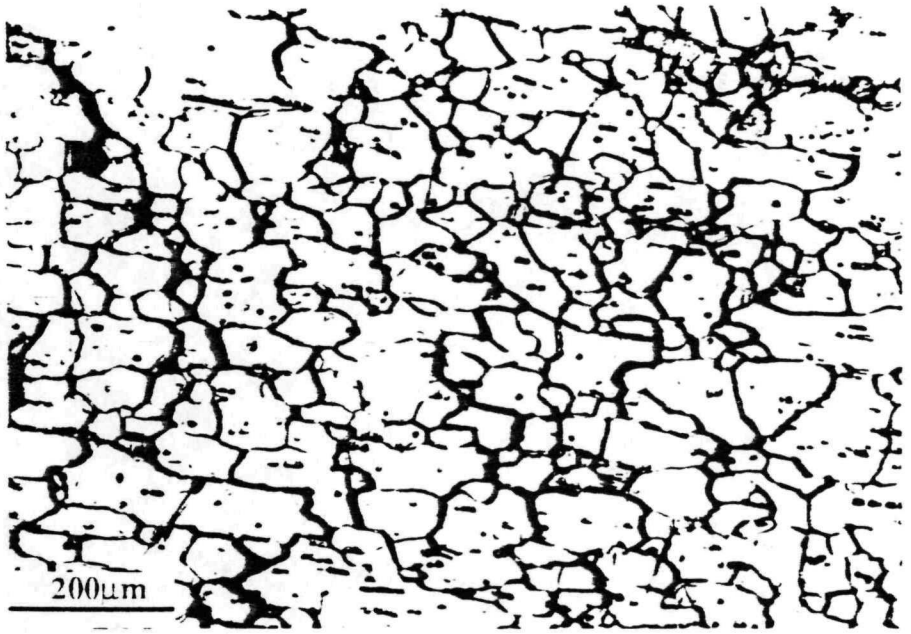

Fig. 3.35. The optical microstructure of the side surface of the specimen tested at 2300 K.

Fig. 3.36. The optical microstructure of the side surface of the specimen tested at 2400 K.

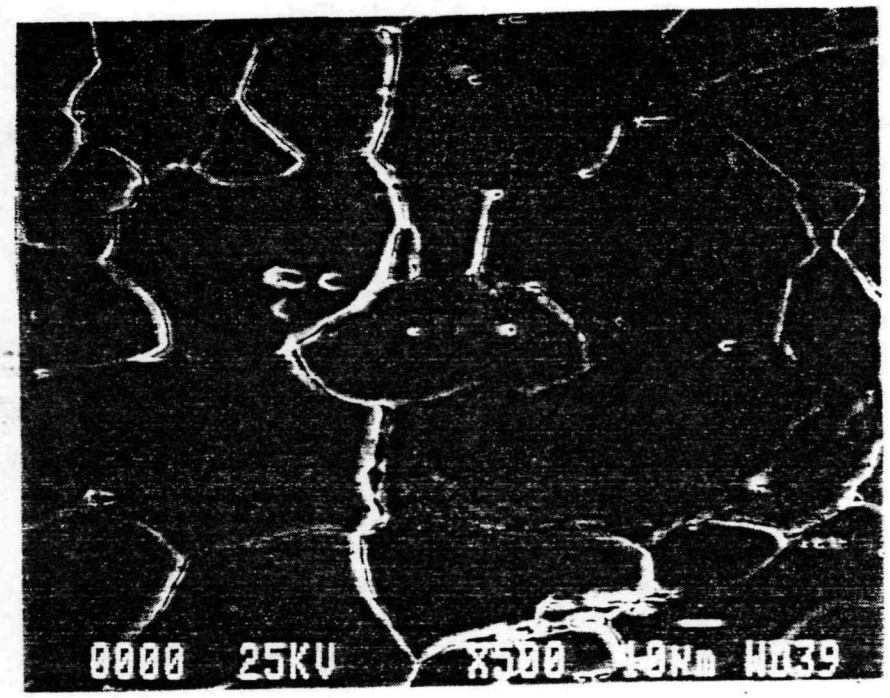

Fig. 3.37. The r-type intergranular cracks found in the W-3.6Re-1ThO_2 specimen creep tested at 2040 K.

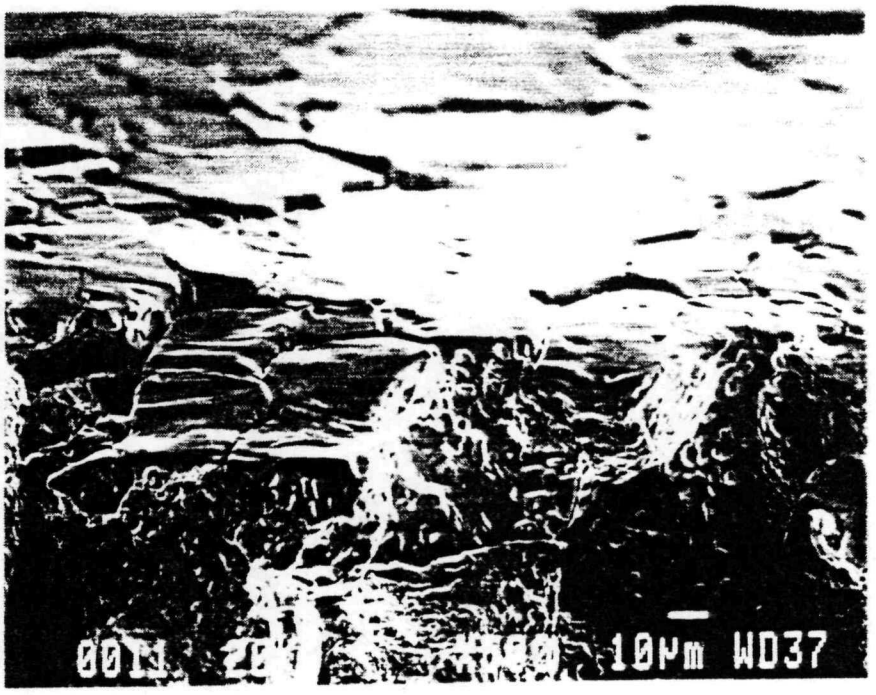

Fig. 3.38. Typical intergranular fracture observed in the 2100 K creep tested W-3.6Re-1ThO_2 specimen.

Fig. 3.39. Dislocation networks observed in the 2100 K creep tested W-3.6Re-1ThO_2 specimen.

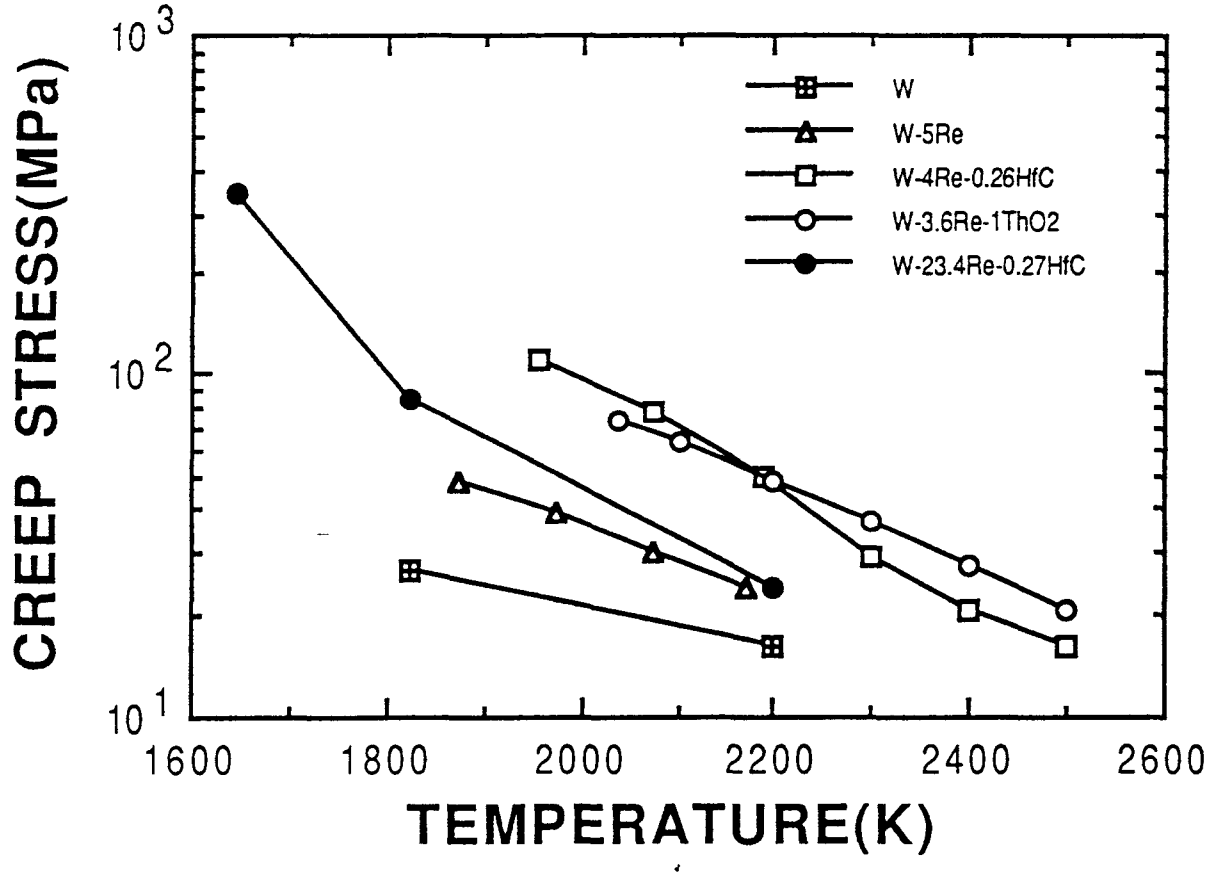

Fig. 3.40. Comparison of the creep strength of various tungsten alloys at a creep rate of 10^{-6}/sec.

Table 3.3 Creep Data for Step-Load Creep Tests of W-4Re-0.26HfC

Test Temp. (K)	Applied Stress (MPa)	Steady-State Creep Rate (1/sec)	Stress Exponent (n)
1955	40	6.170×10^{-9}	5.3
	50	2.020×10^{-8}	
	60	5.185×10^{-8}	
	70	1.182×10^{-7}	
2070	20.7	1.709×10^{-9}	5.2
	31.0	9.661×10^{-9}	
	40.0	3.003×10^{-8}	
	50.0	9.524×10^{-8}	
2190	20.7	6.803×10^{-9}	5.0
	31.0	3.700×10^{-8}	
	40.0	2.222×10^{-7}	
2300	20.7	7.025×10^{-8}	5.4
	25	1.932×10^{-7}	
	31	5.556×10^{-7}	
2400	20.7	3.100×10^{-7}	5.4
	25	8.680×10^{-7}	
2500	20.7	1.167×10^{-6}	5.2
	25	3.370×10^{-6}	

Table 3.5 Creep Data for Step-Load Creep Tests of W-3.6Re-1ThO_2

Test Temp. (K)	Applied Stress (MPa)	Steady-State Creep Rate (1/sec)	Stress Exponent (n)
2040	25	6.462×10^{-9}	4.7
	31	1.735×10^{-8}	
	35	3.139×10^{-8}	
	40	5.594×10^{-8}	
	45	9.951×10^{-8}	
2100	25	1.384×10^{-8}	4.6
	31	3.663×10^{-8}	
	35	6.634×10^{-8}	
	40	1.172×10^{-7}	
	45	2.068×10^{-7}	
2200	25	4.508×10^{-8}	4.6
	31	1.172×10^{-7}	
	35	2.068×10^{-7}	
	40	3.516×10^{-7}	
	45	6.762×10^{-7}	
2300	20.7	6.937×10^{-8}	4.6
	25	1.613×10^{-7}	
	31	4.394×10^{-7}	
2400	20.7	2.776×10^{-7}	4.6
	25	6.593×10^{-7}	
	31	1.758×10^{-6}	
2500	20.7	1.004×10^{-6}	4.6
	25	2.344×10^{-6}	
	31	6.372×10^{-6}	